Sequences of cortical activation states encode search strategies during spatial navigation

A THESIS
SUBMITTED TO THE FACULTY OF THE GRADUATE SCHOOL OF THE
UNIVERSITY OF MINNESOTA
BY

Mathew Lavere Rynes

IN PARTIAL FULFILLMENT OF THE REQUIREMENTS
FOR THE DEGREE OF DOCTOR OF SCIENCE

Prof. Suhasa B. Kodandaramaiah

May 2023

Table of Contents

Acknowledgements

I would like to acknowledge Daniel Surinach, who contributed greatly to this project in all steps. He designed, implemented, and collected data for much of the prototype work presented in Chapter 2 of this thesis. Daniel also made significant contributions to the spatial navigation experiments, and the data analysis for this project possible with his coding expertise. In short, Daniel and I worked very closely on all aspects of this project.

I am extremely grateful to Professor Suhasa Kodandaramaiah and my colleagues in his lab group. Suhasa constantly pushed me to improve myself, and my colleagues in Prof. Kodandaramaiah's lab group were always encouraging and helpful. Prof. Kodandaramaiah's experience and expertise held this project together and kept it progressing smoothly.

I would also like to acknowledge Leila Ghanbari, who completed most of the initial engineering in building the cranial windows or "See-Shells." This work would not be possible without her innovations.

I would also like to acknowledge Skylar Fausner, who diligently pressed me to follow planned schedules I made to make the experiments possible.

I am also grateful to Prof. Alptekin Aksan, who introduced me to Suhasa. Not only have I learned a lot from Prof. Aksan, but he has also helped me improve myself both as a scientist and as a hard worker.

I would like to acknowledge our research collaborator Prof. Timothy Ebner and his group for letting us use some of their lab space for our experiments and sharing experience.

I would also like to thank our collaborator Prof. David Redish for his contributions to research as we were analyzing data and interpreting it. David's expertise was of great help for us as we used our technologies to conduct neuroscience research for the first time.

I would also like to thank Prof. Majid Mohajerani, who collaborated with us while we were developing the mini-mScope. His guidance and use of the technology helped us develop our imaging technology for neuroscientists and demonstrate its capabilities.

Finally, I would like to thank all of my friends, and most of all my family. Without support from them, I would not be able to do this. I would especially like to highlight my brother and fellow scientist Anthony Douglas Rynes, who has been with me for my entire academic career. It was discussions with him that encouraged me to go into this field, and he supported me in any way he could from giving me a lift to discussing data analysis and interpretation. Thank you, brother.

List of Figures

Chapter 1 Introduction

Spatial navigation is an innate ability to orient and make decisions about where to go within an environment is mediated by a network of brain regions. Analysis of spatial navigation in animals has become a critical component in the neurobiology of learning, memory, and cognition. This has commonly been studied using a variety of common experiments such as the Morris water maze (Morris 1981, Morris et al. 1982), and its lower-anxiety variant, the Barnes maze (Barnes 1979). This experimental paradigm has also been studied in diseased states related to stress and depression.

Before such experiments, spatial navigation was investigated by behaviorists with an emphasis on sensory modalities. It was shown with evidence that sensory-guided navigation could be seen as reinforced at decision points in mazes such as the Hampton court maze (Watson 1907). It was initially thought that sensory stimuli controlled responses, called a Stimulus-Response approach to learning (Hull 1934a, 1934b, Kendler and Gasser 1948). However, this understanding was superseded by Morris' experiments, which demonstrated that for spatial learning, the importance of distal sensory cues prevails over nearby stimuli.

Theories were advanced to explain the complexities of spatial learning that based themselves upon internal models. Place learning, the innate ability to learn the spatial layout of an environment, is thought to be critical in the formation of cognitive maps of what is in the environment and where the features of the environment such as sensory cues are with respect to one another. This is fundamental to Tolman's cognitive mapping theory which suggests these maps form and can be utilized to guide navigation (Tolman et al. 1946, Tolman 1948).

The most studied and understood behavioral correlate of spatial navigation is the spatial selectivity of place cells. Place cells were initially described by experiments from O'keefe and

Dostrovsky as hippocampal cells which exhibited spatially-selective firing rates. (O'Keefe and Dostrovsky 1971). Such experiments and the subsequent investigations enabled neuroscience to understand how animals learn environments and how such cognitive maps of spatial locations can be formed however it is not well understood what animals learn and how they achieve navigation using what they've learned, nor is it understood how place cells in the hippocampus contribute to animals' performance in spatial navigation tasks. In order to understand this. The role of distributed functional regions of the cortex have been examined in the context of spatial navigation. Many regions investigated have shown cells with place cell-like properties.

Early incursions in novel environments involve attending to nearby and distant spatial features to create internal representations of the environment, while subsequent forays in the same environment may require matching incoming sensory information to existing internal representations of space to guide navigation. These internal cognitive maps may take multiple explorations of space to be adequately defined before optimal route to desired destination can be planned and executed. Therefore, spatial navigation is a complex cognitive process that involves neural computations in multiple, disparate sensory, motor and memory circuits.

The role of several of several individual brain regions important for spatial navigation has been studied extensively. Surveying findings of such studies shows that activity in each region investigated contributes unique characteristics to spatial navigation capabilities. Neuronal activity in visual cortex has been shown to display task-relevant responses (Niell and Stryker 2010), including those related to spatial locations during navigation (Pakan et al. 2018, Saleem et al. 2018, Flossmann and Rochefort 2021). Activity in visual cortex also increases during locomotion (Erisken et al. 2014, Musall et al. 2019a), which is inherently critical to spatial navigation. Such locomotion signals have also been shown to integrate across multiple regions

to modulate visual activity during navigation (Keller et al. 2012, Saleem et al. 2013, Mika Diamanti et al. 2021).

The role of association areas of the cortex in spatial navigation has also been extensively studied. In rodents, the posterior parietal cortex (PPC) has been shown to have neurons with place-cell-like properties (Krumin et al. 2018a), activity that encodes spatial movement sequences as well as position (Harvey et al. 2012, Krumin et al. 2018a), memory-based decision making (Krumin et al. 2018a), attention to position (Whitlock 2014), visual attention and spatial navigation (Harvey et al. 2012, Whitlock 2014, Krumin et al. 2018a), which has been compared to spatial sequences of movements of the arms in primates (Nitz 2006a). The retrosplenial cortex (RSC) plays crucial roles for spatial navigation. RSC has been discovered to encode both allocentric and egocentric information with regards to navigation (Alexander and Nitz 2015, Miller et al. 2019) and has been found to be involved in landmark encoding (Fischer et al. 2020), route planning (Markus et al. 1995) and associating allocentric cues to motor decisions (Franco and Goard 2021). RSC also integrates spatial information from several different cortical and sub-cortical regions (Alexander and Nitz 2015), including the hippocampus (Wyass and Van Groen 1992). Frontal regions such as the Anterior Cingulate Cortex (ACC) have been demonstrated to be activated after the recall of spatial memory and during foraging and exploration behaviors (Teixeira et al. 2006).

This research aims to investigate the mesoscale cortical neural activity dynamics during spatial navigation in mice. To accomplish this, neurotechnologies capable of overcoming challenges faced by neuroscience were built and tested. This technology is described in **Chapter 2: Technology for mesoscale imaging in freely behaving animals**.

The next chapter, **Chapter 3: Mesoscale imaging during spatial navigation**, describes the use this technology to investigate mesoscale cortical activity in freely moving mice in a behavioral paradigm not possible without such technology. This research utilized a spatial

navigation and memory behavioral assessment to uncover changes in cortex wide activity during spatial navigation. A basic question was posed: *how does cortical activity differ between mice which have learned to navigate a space versus those who haven't? Are navigational strategies reflected by changes in cortex-wide calcium activity?*

Chapter 2 Technology for mesoscale imaging in freely behaving animals

2.1 Significance

Genetically encoded calcium indicators (Chen et al. 2013), along with transgenic approaches for broadly expressing these indicators in the brain in a cell-type specific fashion (Daigle et al. 2018) has enabled mesoscale imaging of multiple cortical regions simultaneously (Vanni and Murphy 2014). These studies have revealed how neural activity across several regions of the cortex are coordinated in a variety of brain states and behaviors (Wekselblatt et al. 2016, Allen et al. 2017, Makino et al. 2017, Musall et al. 2019b, Gilad and Helmchen 2020). These studies have thus far been mostly done exclusively in head-fixed mice (Ferezou et al. 2007, Mohajerani et al. 2013). Even relatively simple behaviors in head-fixed animals require substantial time for acclimatization and training (Niu et al. 2014). To overcome some limitations of head-fixation, immersive virtual reality environments (Pinto et al. 2019a) or voluntary head-fixation of mice in their home cages (Murphy et al. 2016) have been used in mesoscale imaging studies. However, the lack of vestibular inputs and disruptions in eye-head movement coupling (Meyer et al. 2020), and behavioral effects from increased stress (Juczewski et al. 2020) can alter neural activity during head-fixation (Aghajan et al. 2015).

Several head-mounted, miniaturized imaging devices have been developed for cellular-resolution imaging of neural activity from small fields of view (FOV, < 1 mm^2) in freely moving animals (Ghosh et al. 2011, Zong et al. 2017, Skocek et al. 2018). A head-mounted imaging device with a relatively large FOV has recently been engineered for mesoscale imaging in rats (Scott et al. 2018). In comparison to rats, mice have a much larger slate of genetic tools (Namiki et al. 2007, Marvin et al. 2013, Dana et al. 2014). A miniaturized, head-mounted device with a

large FOV for imaging the whole cortex in mice has the potential to expand investigations of mesoscale cortical dynamics during free behavior.

Here, we introduce the “mini-mScope,” a miniature imaging device capable of simultaneously imaging an 8 x 10 mm FOV with resolution ranging from 39.37 to 55.68 µm. The mini-mScope weighs 3.8 g and can be head-borne by a freely moving mouse. We have used the mini-mScope to record mesoscale cortical activity in freely behaving solitary mice and during social interactions with a companion mouse.

2.2 Methods

2.2.1 Mini-mScope design fabrication and assembly

Design: The mini-mScope was designed using a computer-aided design (CAD) program (SolidWorks 2018, Dassault Systèmes). The top and bottom housing were CNC milled from Delrin. The illumination module housings were 3D printed using a desktop stereolithography (SLA) printer (Form 2, Formlabs Inc.) with black polymethylmethacrylate (PMMA) resin (RS-F2-GPBK-04, Formlabs Inc.). 1.5 mm x 2 mm x 1 mm copper plates were soldered to the large pad on the backs of the LEDs to act as heatsinks (**Fig. 2.1a**). A blue LED (LUXEON Rebel Color Blue 470 nm, Digikey Inc.) and custom diced bandpass excitation filter (450-490 nm, 3 mm x 3 mm x 1 mm, ET 470/40x, Chroma) were installed into an illumination module using UV-curable optical glue (AA352 Light Cure Adhesive, LOCTITE) (**Fig. 2.1b-c**). Three such modules were assembled and mounted in the bottom housing of the mini-mScope, and the three blue LEDs were serially wired using 29-gauge wires (Low-Voltage High-Temperature Black, Red Wire with FEP Insulation 29 Wire Gauge, McMaster-Carr) (**Fig. 2.1d**). UV-curable black resin was applied to the back of each blue LED to encapsulate the wires for stabilization. A biconvex lens (3 mm diameter, 4.5 mm focal length, 0.33 NA, Achromatic Doublet Lens, 47-721, Edmund Optics) with a numerical

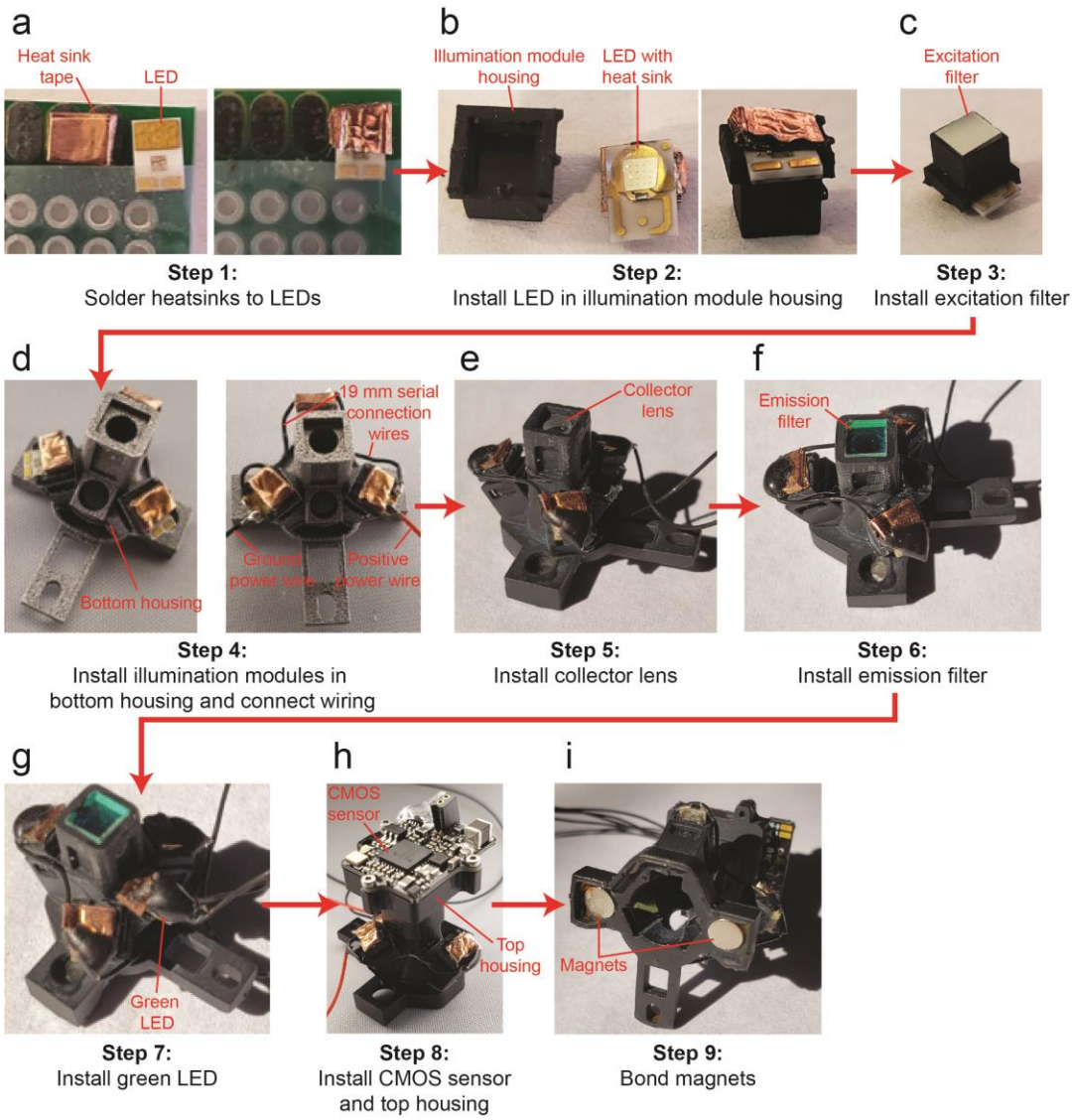

Figure 2.1: Step by step illustration of mini-mScope assembly.

aperture of 0.33 and effective focal length of 4.50 was gently inserted and press fit into the circular slot at the top of the bottom housing, followed by mounting a custom diced bandpass emission filter (500-550 nm, 4 mm x 4 mm x 1 mm, ET 525/50m, Chroma) (**Fig. 2.1e-f**). A green LED (LUXEON Rebel Color Green 530nm, Digikey Inc.) was bonded to the green LED slot of the bottom housing using cyanoacrylate glue (Professional Super Glue, LOCTITE) (**Fig. 2.1g**). A CMOS sensor (Miniscope CMOS PCB, Labmaker) was fastened to the top housing using M1 Thread-Forming Screws (96817A704, McMaster Carr). The top housing was slid onto the

rectangular shaft of the bottom housing, and the focusing was adjusted and then fixed using 316 Stainless Steel 0-80 screws (91735A262, McMaster Carr) (**Fig. 2.1h**). Two circular neodymium magnets (B07C8ZZ2K9, Amazon) were bonded to the bottom surface of the bottom housing with cyanoacrylate glue (**Fig. 2.1i**).

Wiring: A single coax cable (50 Ω co-axial silicone rubber jacketed cable, Cooner Wire) was used to connect the CMOS sensor to the main DAQ board (Miniscope DAQ PCB, Labmaker). For synchronized illumination of alternate frames with blue and green light, the external trigger output from the CMOS sensor DAQ was sent to a microcontroller (Teensy 3.5, PJRC). At each odd frame, a microcontroller sent a 3.3V transistor-transistor logic (TTL) pulse to a power metal oxide field effect transistor (MOSFET IRL520, Digikey) relay to turn on the three blue LEDs for 20 ms. At each even frame, a second TTL pulse lasting 4 ms was sent to a dedicated MosFET powering the green LED. The wires powering the LEDs were routed through a circular hole in the top housing and then a commutator (Carousel Commutator 1x DHST 2x LED, Plexon) for strain relief. High wattage resistors were used in the switching circuit and the power supplies for each illumination source were used to modulate the current delivered to the LEDs and tune light illumination output during *in vivo* experiments.

2.2.2 Animals

All animal experiments were conducted in accordance with protocols approved by the University of Minnesota's Institutional Animal Care and Use Committee (IACUC) and the University of Lethbridge's Animal Care Committee. C57BL/6J, Thy1-GCaMP6f, and Emx-CaMKII-Ai85 mice were used in the experiments. Both male and female mice were used, aged 8-30 weeks. Mice were housed in a 14-hour light / 10 hour dark cycle at 20-23 C and 30-70% relative humidity with ad libitum access to food and water.

See-Shell Preparation and Implantation

See-Shell and protective cap preparation: The See-Shell implant was assembled using the technique adapted from our previous work (Ghanbari et al. 2019a). Briefly, the frame of the See-Shell and protective cap were 3D printed using a desktop SLA printer with UV-curable black PMMA resin. A 50 µm thick PET film (Melinex 462, Dupont Inc.) was bonded to the PMMA frame using quick setting epoxy (ScotchWeld dp100 Plus Clear, 3M Inc.). Two circular neodymium magnets were inserted into the slots on the implant and bottom surface of the protective cap and fixed using cyanoacrylate glue. An 0-80 nut was inserted into the hole in the posterior tab of the implant (Brass Hex Nut, 0-80 Thread Size, McMaster-Carr).

Surgical Implantation

See-Shell implantation: Mice were administered 2 mg/kg of slow release Buprenorphine (Buprenorphine SR-LAB, Zoopharm Inc.) and 2 mg/kg of Meloxicam for analgesia and inflammation prevention, respectively. Mice were anesthetized in an induction chamber containing 1-5% isoflurane in pure oxygen. The scalp was shaved and sterilized, followed by application of sterile eye ointment (Puralube, Dechra Veterinary Products) to the eyes. Mice were then transferred and affixed to either a standard rodent stereotax (Model 900LS, Kopf Inc.) or an automated robotic surgery platform, the Craniobot(Ghanbari et al. 2019b, Rynes et al. 2020). The scalp above the dorsal cortex was excised using surgical scissors and fascia was removed using a 0.5 mm micro-curette (10080-05, Fine Science Tools). A large craniotomy over the dorsal cortex was performed either manually using a high-speed dental drill or automatically using the Craniobot. Once the skull was removed, the exposed brain was immediately covered in a gauze pad soaked in sterile saline to keep the brain hydrated.

The See-Shell implant was sterilized by soaking in 70% ethanol for 2 minutes, followed by thorough rinsing with sterile saline. The gauze pad on the brain was removed and excess blood from the craniotomy was cleared using cotton tip applicators (823-WC, Puritan). The See-Shell implant was gently placed on the skull, and the area of the skull surrounding the See-Shell was

dried using cotton tipped applicators. Surgical glue (Vetbond, 3M Inc.) was applied around the edge of the See-Shell followed by opaque dental cement (Metabond, Parkell Inc.) to adhere it to the skull. The cement fully cured before the protective cap was magnetically attached. Mice recovered on a heated recovery pad (72-0492, Harvard Apparatus Inc.) until fully ambulatory before returning to a clean home cage. Post-operative analgesia and anti-inflammatory drugs were administered for up to 72 hours post-surgery. Mice were subsequently allowed to recover for 7 days prior to imaging experiments.

The mini-mScope has been characterized for imaging through a See-Shell implant. However, it could be beneficial to perform imaging in intact skulls, which entails a much simpler surgical preparation. Intact skull surgical preparation followed the protocol described previously (Silasi et al. 2016). We modified the See-Shell implant, by removing the PET film and fixing the frame directly onto the skull to create a chamber. The chamber was filled with clear dental cement to cover the skull and create a refractive index-matched surface and was covered by a PET film cut to the profile of the outer perimeter of the frame.

The animal was aseptically prepared, followed by removal of the scalp and fascia from the skull. A skull anchor screw was implanted over the occipital bone. A sterilized See-Shell frame without PET film bonded onto it was fixed to the skull with surgical glue. Clear dental cement (Metabond, Parkell Inc.) was placed over the dorsal skull in the well created by the See-Shell implant taking care to fill the skull sutures properly. Immediately after filling the implant with a thin layer of clear dental cement, a sheet of PET cut out to the dimensions of the imaging area in the See-Shell was placed on top of the cement.

Mice recovered from surgery for at least 3 days before experimentation. Mice were imaged while presenting a sensory stimulus in both an anesthetized animal, and a freely behaving animal. We analyzed the imaging data using the same preprocessing and filter set we used for the experiments using the mini-mScope modified See-Shell.

Electrophysiology: In experiments where we performed simultaneous electrophysiology and mesoscale imaging, a hippocampal electrode was implanted through a hole outside the area of the See-Shell craniotomy. Briefly, a bipolar (tip separation of 500 µm) electrode made from Teflon-coated stainless-steel wire (bare diameter 50.8 µm) was placed in the pyramidal layer of the right dorsal hippocampus. It was inserted posterior to the occipital suture at a 33-degree angle (with respect to the vertical axis) according to the following coordinates relative to bregma: ML: 2.3 mm; dorsoventral (DV): 2.2 to 2.5 mm. The position of the electrode tips was confirmed using an audio monitor (AM8C #72x32B, Grass Instrument Co.). After electrode implantation, the craniotomy was performed and the See-Shell was implanted on the skull as described above.

2.2.3 Testing

Benchtop characterization optical imaging performance of the mini-mScope

Resolution testing: A transparent 1951 USAF test target was cut to isolate each group and the center of the target was placed onto a 3D printed inverse mold of the See-Shell contour with markings for 8 different test locations in the FOV. A See-Shell implant was pressed onto the inverse mold with the target and images were taken in each location.

Illumination profile: To measure the uniformity of illumination, a custom 3D printed acrylic container was filled with fluorescein dye (10% v/v, F2456, Sigma Aldrich Inc.) infused 3% agar gel. The See-Shell implant was placed on the container such that the entire bottom surface of the See-Shell was uniformly coated with fluorescent gel. The mini-mScope was attached to the See-Shell and single images were acquired. The current delivered to the LEDs was modulated using power supplies in the switching circuit to eliminate FOV saturation. The captured images were analyzed in MATLAB 2019a (MathWorks, Inc.) using custom code.

LED switching dynamics and LED power stability testing: To test LED stability, the blue LEDs were pulsed at 100 Hz and output light was measured using a photoresistor (NSL-19M51,

Advanced Photonix). The output voltage of the photoresistor was analyzed in MATLAB to calculate the mean intensity across the FOV.

Focusing and calibration of mini-mScope

Before every experiment, mice were lightly anesthetized (0.5-1% isoflurane in pure oxygen) and head-fixed in a stereotax to clean the See-Shell surface of any debris. The mini-mScope was then securely mounted on the implant. The green LED was switched on and the position of the top housing relative to the bottom housing was manually adjusted until the area around the midline was in focus. The adjustment screw was tightened to secure it in place. Once focused, the three blue LEDs and green LED were alternately pulsed, and their intensities were adjusted by modulating the power delivered to the LEDs using each power supply.

***In vivo* calcium imaging in anesthetized mice**

In vivo calcium imaging experiments were performed to compare mini-mScope imaging capabilities to a conventional macroscope. Mice were lightly anesthetized and affixed to a custom stereotaxic setup under a macroscope (Leica MZ10F, Leica AG). Images from the macroscope were captured using a sCMOS camera (Orca Flash 4.0, Hamamatsu Inc.). Bright field images were first captured to assess the quality of the cranial window followed by epifluorescence imaging. Blue illumination was captured at 8 bits and 15 Hz in the mini-mScope. The sCMOS camera was configured to acquire images at 8 bits and 30 fps. In the final imaging analysis, every other frame was discarded to ensure an effective acquisition rate of 15 Hz. The mini-mScope was attached immediately after image acquisition from the macroscope and 4 minutes of spontaneous calcium activity were captured. To evaluate a neural response to sensory stimuli, a 1 s vibrational stimulus was provided to the hindlimb using a 3V DC mini vibration motor (A00000464, BestTong) at 100 Hz. For visual stimulus, a white LED was positioned ~ 2 cm from the left eye of the mouse

to cover the fovea in the visual field. 100 ms flashes of light were presented after ensuring stimulus delivery was confined to the left eye.

Open field and social behavior experiments

Mice underwent acclimatization for 3-5 days in which an experimenter handled each mouse for 5-15 minutes. The mice were fitted with a mini-mScope replica with the same weight as a fully assembled mini-mScope during the handling period. For experimentation, the mini-mScope was fitted onto the mouse, which was quickly transferred to an open field arena. Experimental trials lasted 6 minutes, including a two-minute period to allow the LEDs to warm up to their maximum intensity. During social behavior experiments, a C57BL/6 mouse of the same sex was gently introduced into the arena by an experimenter 4 minutes after initiation of the trial.

Sleep recording experiment

Mice were habituated for 7 days in the recording setup with the mini-mScope mounted on their head. Each mouse was recorded for two sessions, each lasting two hours. Hippocampal LFP was amplified (×1000) and filtered (0.1-300 Hz) using a Grass P5 Series AC amplifier (Grass Instrument Co.) and was sampled at 1 kHz using a data acquisition system (Axon Instruments). A camera (Camera Module V2 #E305654, Raspberry Pi) was used to record behavior during the recording.

2.2.4 Data Analysis

Behavior video analysis: Videos of mouse behavior were captured in .avi format using an overhead camera (ELP_USB8MP02G-L75, ELP). Mice were tracked using either Zebtrack(Pinheiro-da-Silva et al. 2016) software in MATLAB or using Deeplabcut(Mathis et al. 2018). Each trial was manually verified to ensure tracking accuracy. A 17 cm square area was defined at the center of the arena as the ‘open field’. To segment the behavior based on different

behavior epochs, four researchers manually scored behavior with 1 s precision based upon whether the mouse with the mini-mScope was moving, still, grooming or rearing, and whether the mice engaged in social behavior indicated by touching in “contact” and “no contact” epochs. Scoring data was processed if there was consensus with at least 3 researchers.

Imaging data pre-processing: Data from the CMOS sensor was captured in .avi format (RGB, 480x752 image size) and contained alternate blue and green channel data. A custom MATLAB script was used to convert the videos from RGB to grayscale and truncated to exclude the 2-minute LED warmup period at the start of each trial. The resulting video was segmented into individual blue and green channel videos. Blue and green frames were binned using a bilinear spatial binning algorithm in MATLAB. Pixels in each channel were corrected for global illumination fluctuations using a correction algorithm (Vanni and Murphy 2014) and were spatially filtered using a custom weighted spatial filtering algorithm.

$\Delta F/F$ *calculations:* Intensity values from the selected ROIs from the blue and green illumination videos were computed using FIJI 2.1.0/ImageJ 1.53c.(Schindelin et al. 2012) Change in fluorescence for both GCaMP and reflectance signals were calculated over a baseline average across the whole time series.

Hemodynamic correction: The green channel $\Delta F/F$ traces were filtered using a zero-phase Chebyshev lowpass filter (cutoff frequency of 0.15 Hz). The blue $\Delta F/F$ and filtered green $\Delta F/F$ traces were used to perform hemodynamic correction as described previously (Musall et al. 2019b). The hemodynamic corrected traces were filtered using a zero-order phase Chebyshev bandpass filter (cutoff frequencies of 0.1 Hz and 5 Hz).

Open field experiments: The videos acquired from freely moving animals were corrected for lateral motion artifacts using MoCo rigid motion correction (Dubbs et al. 2016). The first frame of the video was used as the template for motion correction. Parameters used for the MoCo plugin

were w = 40 and a down sample value = 0.5. Log files of pixel displacements and a corrected output video were generated.

The time stamp data from the Miniscope v3 software contains a list of frames captured by the behavior camera and CMOS sensor. To mitigate frame pacing issues with the CMOS sensor, only frames within ±10% of the specified frame rate were kept. To address the frame dropping issues with the behavior camera (usually dropped ~400/10800 frames), common frames that exist in the CMOS video and behavior camera video were stored. The resulting data was compared to the manually scored behavior data to find the intersection between these frame data sets. Finally, this list was searched to find points with consecutively paired blue and green frames to be used for hemodynamic corrections.

Seed-pixel correlation maps: Cortical regions of interest were selected within each video trial by removing the background and areas with high vasculature and seed pixels within 6 regions (motor cortex (M1), frontal lobe (FL), barrel cortex (BC), retrosplenial cortex (RSC), visual cortex (VC), hind limb (HL) were selected for further analysis. Cortical regions were selected by imposing a post-surgery image onto a map extracted from Brain Explorer 2 (Lau et al. 2008) and registering regions based upon static landmarks on the implant with respect to Bregma and Lamda. Seed pixel correlation maps were generated using Pearson's correlation coefficient (PCC) to compare the correlation between a desired seed pixel and other pixels in the FOV. Data from the manual scoring (**Fig. 4c** and **d**) was used to generate a list of frame numbers where the mouse was either moving or still. To calculate PCC during these discontinuous epochs of time, a moving window of 1 s with a 0.5 s sliding window was incorporated between small clusters of continuous behavior. The PCC between the seed pixel trace and every other pixel in the desired regions of the cortex was calculated for each window length portion. The mean of all the PCCs was computed and stored as the PCC value for each pixel in the FOV. This process was repeated for each trial and mouse to generate representative seed pixel maps for one trial as shown in **Figure 4f.** The PCC

value between the chosen seed pixels were averaged across all trials in spontaneous free behavior to generate the inter-seed correlational plots shown in **Figure 4h**. To measure the change in activity across the left hemisphere where the seed pixels were chosen, the percentage of pixels in this ROI with PCC $r > 0.5$ was averaged across trials (**Fig. 4g**). Similar analysis was performed for social interaction experiments.

Glutamate data preprocessing: Raw data of spontaneous glutamate activity was preprocessed based on the following steps: First, the time series of each pixel was filtered using a zero-phase bandpass Chebyshev filter between 0.1 and 5 Hz. Then a baseline signal was calculated by averaging all the frames, and the fluorescence changes were quantified as ΔF/F × 100, where F is the filtered signal. To reduce spatial noise, images were filtered by a Gaussian kernel (5 × 5 pixels, sigma = 1).

State scoring: Behavioral states were scored visually using hippocampal LFP and movement signal in 10 s epochs. Movement signals were calculated using a previously described algorithm(Singh et al. 2019). Active wakefulness (aW) was characterized by theta hippocampal activity and high movements. Quiet wakefulness (qW) was characterized by theta hippocampal activity and minimum movement. NREM sleep (N) was characterized by large irregular activity in hippocampus and no movement. REM sleep (R) was characterized by theta hippocampal activity and no movement.

Correlation analysis: A uniform meshgrid with ~1.2 mm distance between its points was laid on the field of view and signal at each ROI (0.2 mm^2) was calculated. Quiet wake, NREM sleep and REM sleep were scored for each recording based on above criteria and Pearson correlation coefficients were calculated between each ROIs during qW, NREM and REM.

2.3 Results

2.3.1 Mini-mScope Design

The mini-mScope design was constrained by three criteria. First, the overall weight of the device needed to be less than ~15% of the mouse bodyweight (<4.0 g) to permit free behavior and mobility. Second, the device required the capability to image most of the dorsal cortex of the mouse. Third, the imaging resolution needed to be sufficient to image mesoscale activity dynamics across the whole FOV. We recently developed See-Shells–transparent polymer skulls that can be chronically implanted on mice and provide access to 45 mm^2 of the dorsal cortex(Ghanbari et al. 2019a) in head-fixed animals. In this study, we adapted the See-Shell to fit the mini-mScope by incorporating a planar top surface in the 3D printed frame, eliminating the headpost, and incorporating three tabs. Disk magnets were embedded in the two lateral tabs to align with disk magnets on the bottom of the mini-mScope or a protective cap (**Fig. 2.2a**). A short sleeve surrounding the mini-mScope base and the posterior tab in the bottom housing constrains the mini-mScope laterally once mounted on the See-Shell. The tab at the back of the See-Shell

frame was used to gently restrain the mouse during removal of the protective cap and attachment of the mini-mScope. Attaching the mini-mScope typically takes less than 5 seconds and can be done without anesthetizing the mouse.

The mini-mScope consists of two interlocking computer numerical control (CNC) machined Delrin housings (**Fig. 2.2a**). Three blue LEDs paired with an excitation filter are installed into three illumination arms in the bottom housing (**Fig. 2.2b**). A green LED provides illumination for reflectance measurements. A biconvex lens and emission filter are embedded in a central shaft of the bottom housing. A complementary metal oxide semiconductor (CMOS) sensor is mounted on the top housing, which is designed to slide along the central square shaft of the bottom housing for focus adjustments. The three blue LEDs are wired in series, and wires to

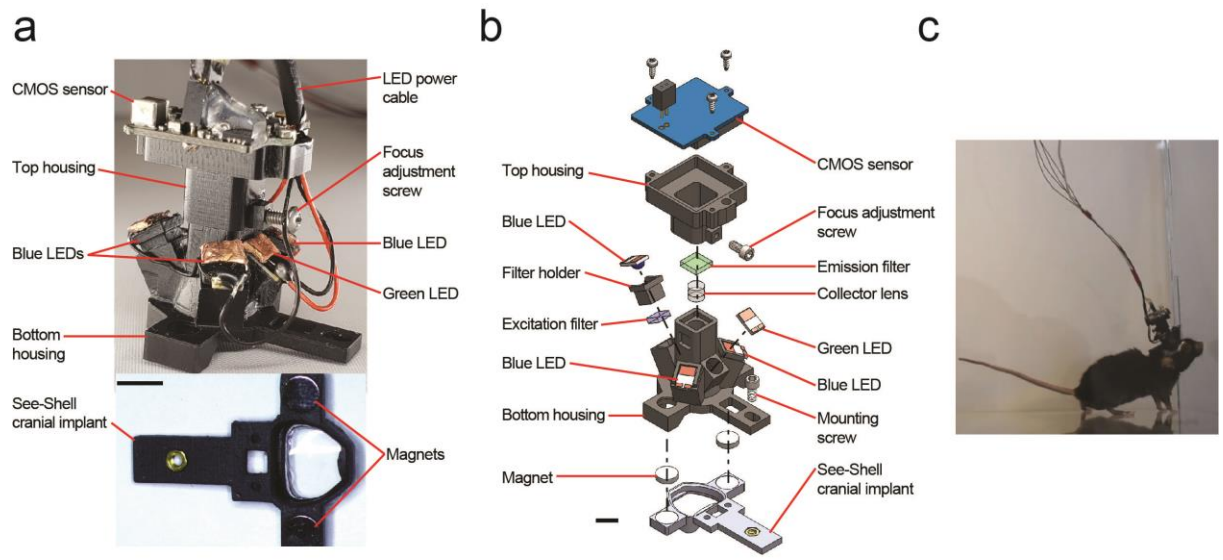

Figure 2.2: mini-mScope: A miniaturized head-mounted device for whole-cortex mesoscale activity mapping in freely behaving mice. (a) Photograph of the fully assembled mini-mScope and the corresponding See-Shell implant. Scale bar, 5 mm **(b)** Computer-aided design (CAD) rendering of the mini-mScope showing the internal components. The device is attached to the See-Shell implant via magnets. Three blue LEDs are attached to a filter holder that has a 480 nm excitation filter to excite GCaMP6f in the cortex. The green LED is used to obtain reflectance measurements for hemodynamic correction. Resulting emission signals (~520 nm) are focused through a collector lens and passed through an emission filter onto a CMOS sensor that can be manually focused. Scale bar indicates 5 mm. **(c)**: A still image of a mouse bearing the mini-mScope and engaging in natural behaviors.

power the green and blue LEDs are routed through a commutator to alleviate torsional strain on the device. Mice exhibited a repertoire of behaviors, including grooming and rearing, indicating their comfort with the mini-mScope.

The weight of the device is 3.8 g, which is heavier than some miniaturized microscopes(Ghosh et al. 2011), but comparable to devices developed for volumetric imaging (Skocek et al. 2018). Based on computer-aided design (CAD) simulations, we estimate that the center of gravity is ~24.7 mm above the mouse head. Detailed instructions for assembling the mini-mScope are provided in **Chapter 2.2.1.**

Mini-mScope Optical Performance

In contrast to typical imaging through a reinforced intact skull, the mini-mScope images the cortex through a transparent polymer skull. Qualitatively, imaging the cortex of a Thy1-GCaMP6f mouse (Dana et al. 2014), which expresses fluorescent reporters of calcium activity in excitatory neurons, with the mini-mScope allowed us to achieve a high optical resolution across the FOV (**Fig. 2.3a**) compared to imaging the cortex through the intact skull using an epifluorescence macroscope through a coverslip (**Fig. 2.3b**). To measure the mini-mScope's resolution, we imaged a 1951 USAF resolution test target positioned at 8 different locations across the FOV (**Fig 2.4**). At a location corresponding to ~ -5.5 mm anteroposterior (AP), ~0 mm mediolateral (ML) with respect to Bregma, lines in group 3, element 6 are clearly visible, indicating

a resolution of 39.36 µm at this location. Since a single biconvex lens was used to image a convex surface, not all areas of the cortex are in focus and the optical resolution varied.

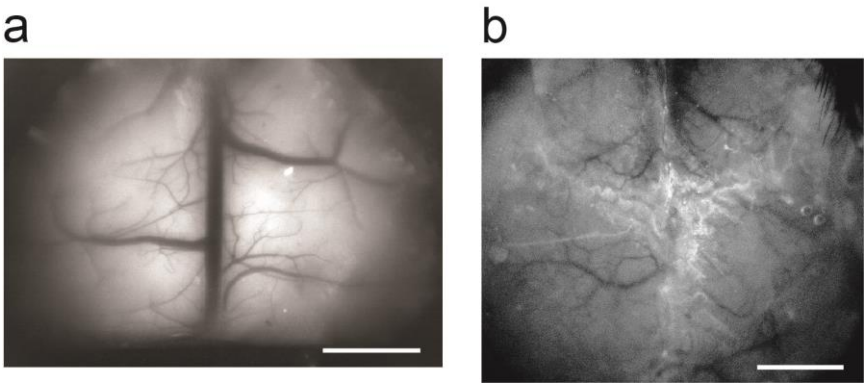

Figure 2.3: Example imaging through intact skull with macroscope vs craniotomy with mini-mScope. (a) Fluorescence image of the whole dorsal cortex of a Thy1-GCaMP6f mouse captured by the mini-mScope. Scale bar indicates 2 mm. Image representative of n = 29 mice. **(b)** Comparative image of a head-fixed Thy1-GCcaMP6f mouse imaged using a standard epifluorescence macroscope through an intact-skull preparation. Scale bar indicates 2 mm. Image representative of n = 2 mice.

The top housing was adjusted to obtain the best focus at ~1 mm lateral to the midline, resulting in resolution ranging from 39 µm along the midline to 55.6 µm more laterally, sufficient for observing mesoscale calcium activity.

The mini-mScope's array of three blue LEDs paired with excitation filters delivered a cumulative ~31 mW of power to the brain. Two of the blue LEDs are oriented at 30 degrees with respect to the optical axis. The third, located at the anterior of the bottom housing, is oriented at 25 degrees with respect to the optical axis. The LEDs are revolved around the optical axis at angles of 90, 225, and 315 degrees (**Fig. 2.5**). A green LED located at the posterior of the bottom housing at an orientation of 55 degrees with respect to the optical axis delivered ~0.22 mW of power and was used for reflectance measurements (Ma et al. 2016). We imaged fluorescein dye-infused agar gel using the mini-mScope to investigate illumination uniformity (**Fig. 2.4**). The normalized light intensity decreased by 56.1%, 53.3%, and 46.2%, compared to the maximum

intensity, at the ML lines at 1.4 mm AP, -2.8 mm AP, and -4.2 mm AP, respectively (**Fig. 2.4b**). The greatest reduction of illumination from the maximum did not exceed 60%. These metrics are

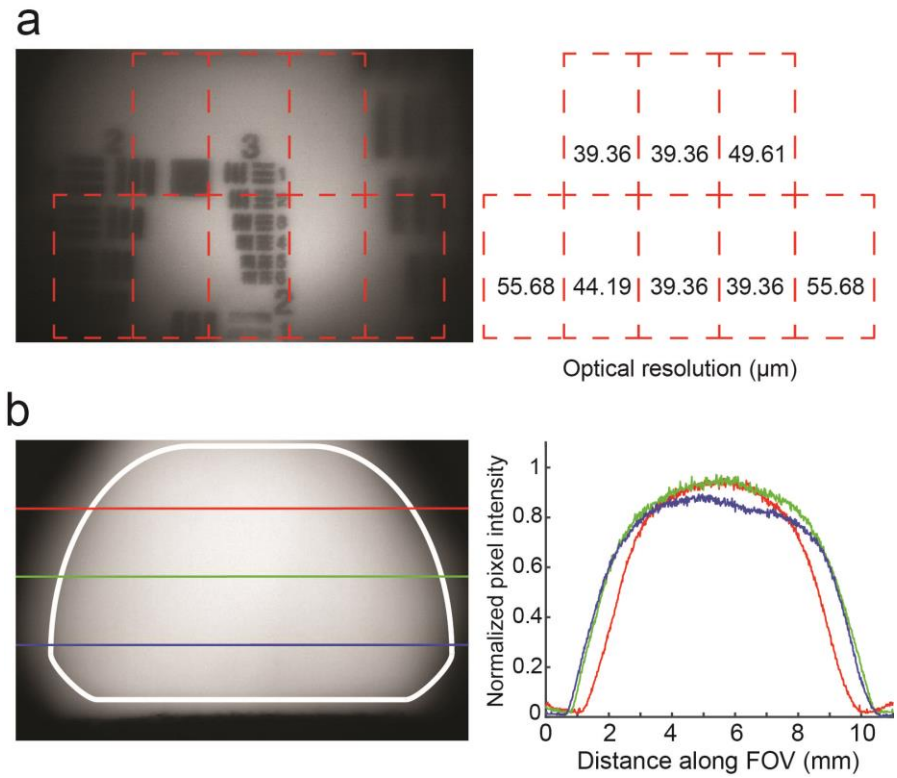

Figure 2.4: Testing the resolution and illumination of the mini-mScope. (a) *Left:* Resolution test target overlaid onto the mini-mScope FOV. *Right:* Resolutions obtained within each specified grid. **(b)** *Left:* Image of fluorescein dye infused agar phantom captured by the mini-mScope. Colored lines indicate medio-lateral sections along which illumination profiles were obtained FOV. *Right:* Plot of normalized illumination profiles from sections denoted in the *Left* panel.

comparable to the performance of previously developed large FOV scopes (Scott et al. 2018), and allowed signals obtained from all pixels to be well within the dynamic range of the CMOS sensor.

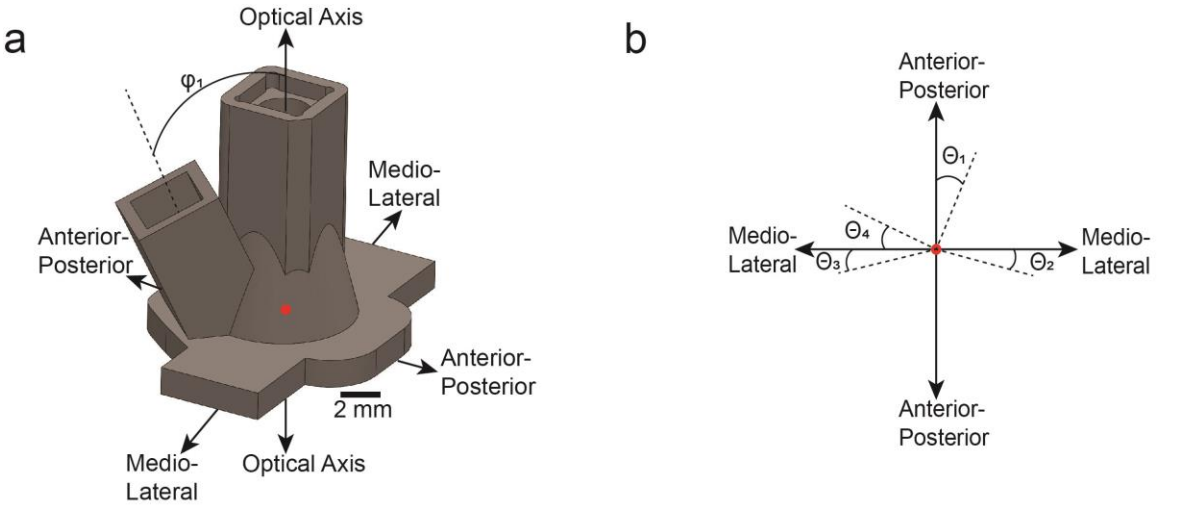

Figure 2.5: mini-mScope illumination design. (a) An illustration of the illumination design for the main body of the mini-mScope. The optical access is perpendicular to the imaging plane – oriented towards the CMOS sensor and the surface of the cortex. The number of LEDs and their angles φ were iteratively altered to optimize device weight and uniform illumination of the cortex. **(b)** A graph depicting how the illumination design was optimized for the mini-mScope. The graph shows the axes when viewing the mini-mScope along the optical axis towards the imaging surface. The angles Θ were modified similarly to the design constraints described in **(a)**.

The CMOS sensor captures images of the cortex alternatively illuminated by the green LED for reflectance imaging and the blue LEDs for epifluorescence imaging. A trigger circuit uses time stamps of CMOS frame acquisitions to precisely switch between the blue LEDs and green LED (**Figure 2.6**).

Because fluctuations in the collected fluorescence signals could be attributed to changes in neural activity or caused by fluctuations in the illumination power of the LEDs, we tested the stability of light power output delivered by the LEDs. Each LED is driven at a 30% duty cycle (20ms every odd frame lasting ~33.3ms) when images are acquired at 30Hz. Each blue LED delivered mean light power of 7.67mW at 30% duty cycle. Continuous illumination at these powers for the durations tested (3-4 minutes) resulted in negligible changes in average blue light output ~0.76% variation around the mean. The green LED delivered mean light power of 0.11mW at 6% duty cycle. Continuous illumination at these powers for the durations tested (3-4 minutes) resulted in negligible changes in average green light output ~0.33% variation around the mean.

Additional tests conducted on the collected videos using the CMOS sensor were checked to quantify the cross-bleeding of the illumination light sources into each other's frames. The emission signal for GCaMP is proportional to the blue excitation light power provided (independent of green light provided). As such, during the decay cycle of the blue LEDs, the amount of GCaMP that is excited also decreases very rapidly, and thus the cross-over of the blue excitation light into the green frames that can elicit an emission response is negligible. On the contrary however, the green reflectance illumination provided is calcium-independent in the sense that the cortex will have a reflectance response to any proportion of green illumination provided. The green illumination light can reflect back through the emission filter and onto the CMOS sensor as the green LEDs power down during alternate LED pulsing and potentially bleed into the blue frame signal. To quantify this response during realistic *in vivo* testing conducted on anesthetized mice, blue LEDs were pulsed for 6 minutes and the green LED was turned on at the 4-minute mark. The change in the mean blue intensity during this turn-on period was no more than 0.34%

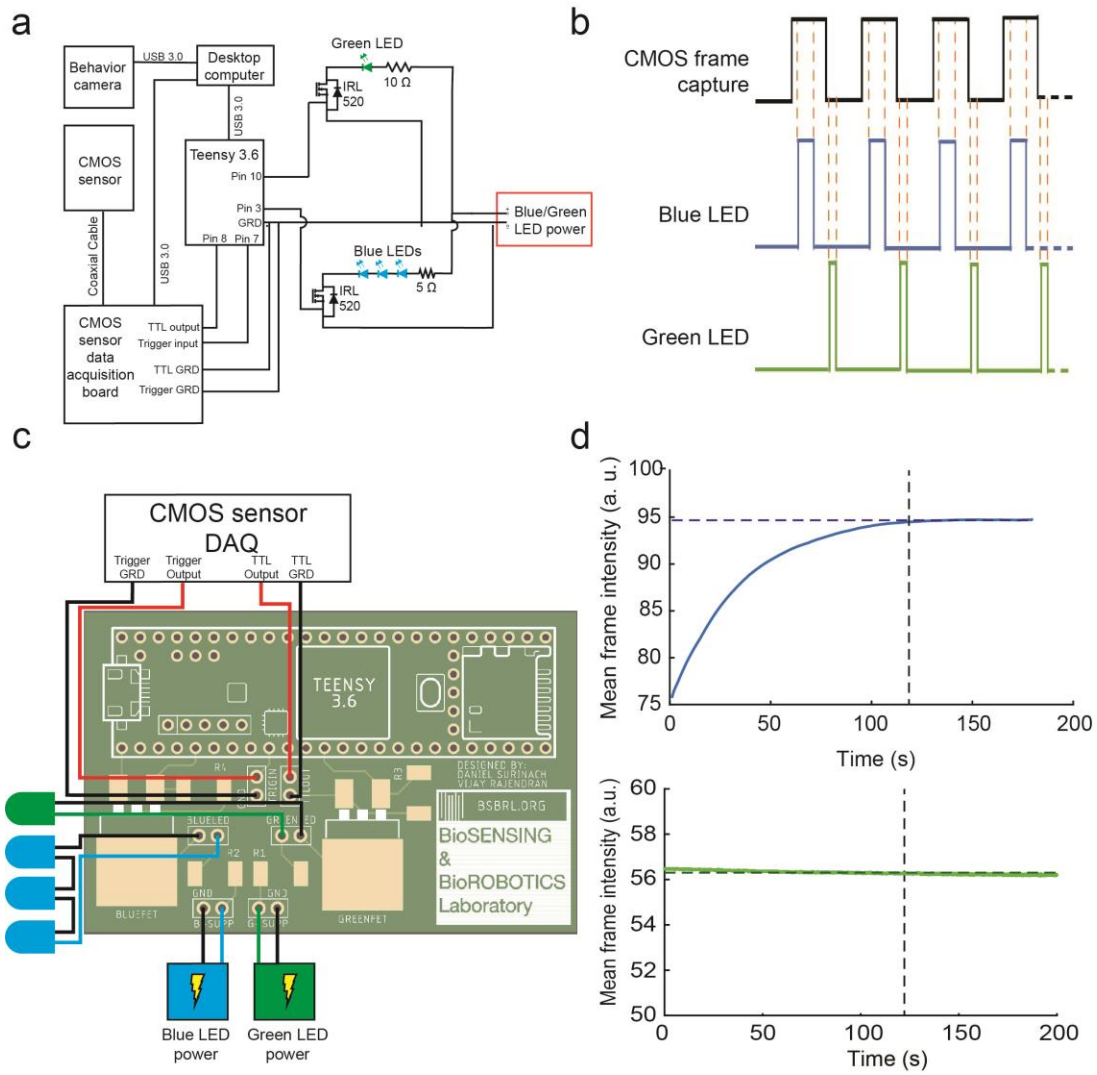

Figure 2.6: Mini-mScope electronics and LED power. (**a**) Schematic of circuitry used for alternate illumination of cortex with blue light for fluorescence and green light for reflectance. For every frame captured by the CMOS sensor, the camera data acquisition (DAQ) board sends transistor-transistor-logic (TTL) pulse to a microcontroller (Teensy 3.6). The microcontroller in turn sends alternate TTL pulses to switching circuits that power three blue LEDs and one green LED. The DAQ also controls the behavior camera synchronization with the CMOS sensor to collect cortical and behavioral data simultaneously. (**b**) Frame capture synchronization between the CMOS sensor and LED pulses. At every odd frame, the microcontroller pulses the blue LEDs for 20 ms. At every even frame, the microcontroller pulses the green LED for 4 ms. (**c**) PCB schematic to house the switching circuit. (**d**) Long term LED stability was tested by illuminating a fluorescein dye agar phantom with excitation and emission bands similar to GCaMP6f. The resulting emission signals are collected onto the mini-mScope CMOS sensor. *Top*: The mean frame intensity captured with blue light illumination is shown with the solid blue line. The black dashed line indicates an approximate 120 second warm-up period until a stable illumination point is reached (blue dashed line). *Bottom*: The mean frame intensity data captured with green light illumination is shown with the solid green line. The black dashed line indicates an approximate 120 second warm-up period until a stable illumination point is reached (green dashed line)

between the two illumination sources.

Pulsing the LEDs at high powers above their operating voltages can lead to additional light intensity noise and long-term damage of the LED themselves. To mitigate this issue, 1/8-inch copper tape was soldered to the back of the LED heat sink pads and allowed for long-term illumination experiments to be conducted (up to 10-minute experiments) with negligible LED damage and noise.

The circuit and LEDs have first-order dynamics with the blue LEDs and green LED having time constants (to reach 66.66% peak power) of 1.79 ± 0.31 ms and 1.97 ± 0.10 ms, respectively. The Blue LEDs and green LED were switched on for 20 ms and 4 ms, respectively, starting after the CMOS sensor initiated each frame capture. The LEDs' power intensity had a slow drift in average intensity value lasting ~2 minutes after which they equilibrated (**Fig. 2.6**). Therefore, we allocated a two-minute warm-up period for the blue LEDs during each experiment for the power intensity to stabilize before data collection.

Comparison with conventional epi-fluorescence macroscope

We next compared the mini-mScope's imaging capabilities to a standard epifluorescence macroscope by imaging spontaneous cortical activity under anesthesia. Despite substantial differences in the capability of the optics and the image sensors, we captured qualitatively comparable widefield images and calcium activity with both instruments (**Fig. 2.7a-b**). We observed heart beat-related oscillations in the calcium signals at 6-7 Hz in the imaging performed with both instruments (**Fig 2.7c**). The histograms of $\Delta F/Fs$ and z-score of intensity values acquired

from three regions of interest (ROIs) show minimal differences between the data captured from the two instruments (**Fig. 2.7d-e**). The probability of ΔF/F values being over 1 standard deviation from the mean was 31.7% for the mini-mScope and 30.2% for the conventional macroscope.

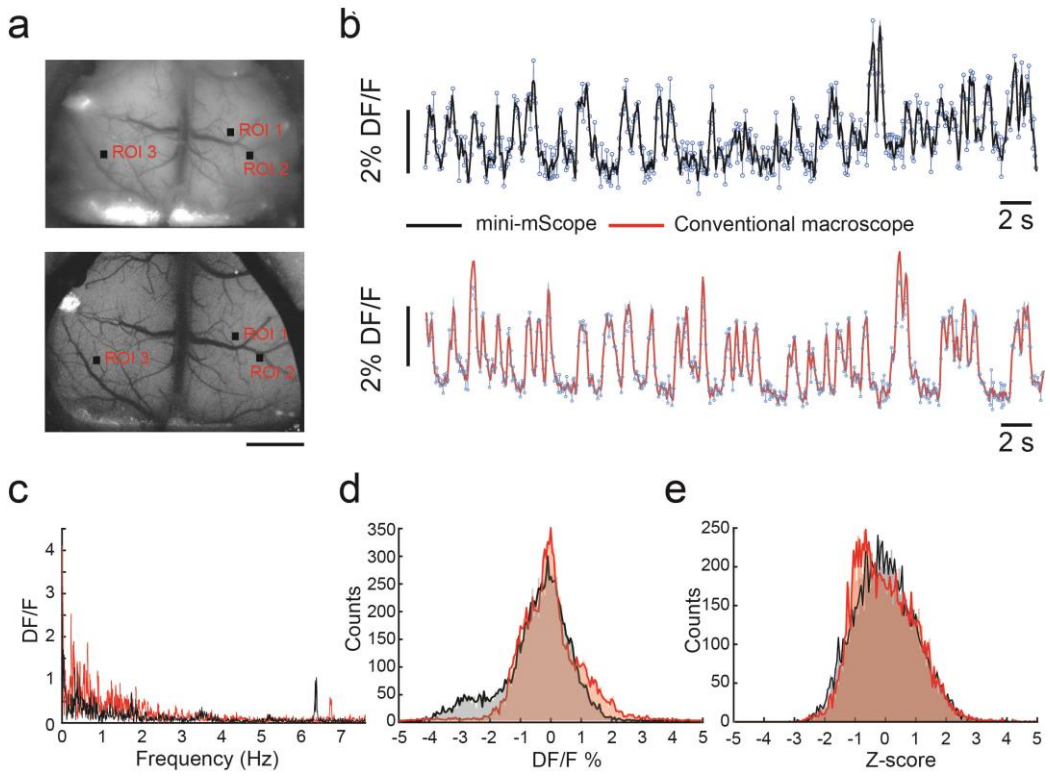

Figure 2.7: Comparison of calcium dynamics imaged with the mini-mScope to conventional widefield epifluorescence macroscope. (a) *Top:* Image of the dorsal cortex taken with mini-mScope of a Thy1-GCaMP6f mouse. Image representative of n = 29 mice. *Bottom:* image taken with a conventional widefield epifluorescence macroscope during the same experimental session. Image representative of n = 8 mice. Black squares indicate ROIs selected for ΔF/F traces analyzed in **b-e**. Scale bar indicates 2 mm. **(b)** ΔF/F traces of ROI 1 shown in **a** recorded for 120 seconds. In **(b-e)**, black and red traces indicate filtered traces (Savitzky-Golay filter, 3rd order polynomial, 5 point moving average) of ΔF/F recorded from the mini-mScope and the macroscope respectively. Blue traces with markers indicate raw ΔF/F values under 1% isoflurane anesthesia. **(c)** Plot of the ΔF/F versus Frequency obtained by computing the discrete Fourier series of 120s of spontaneous calcium activity recorded under isoflurane anesthesia (from traces shown in **b**.) **(d)** Histogram of ΔF/F values over 2-minute videos captured at the same 1% isoflurane anesthesia conditions with the mini-mScope and the conventional macroscope in the three ROIs indicated in **a**. **(e)** Histogram of z-scores of fluorescent intensity values over 2-minute videos captured at the same 1% isoflurane anesthesia conditions with the mini-mScope and the conventional macroscope in the three ROIs indicated in **a**.

Green reflectance channel imaging allowed correction of the calcium fluorescent signals for hemodynamic effects (**Fig. 2.8).**

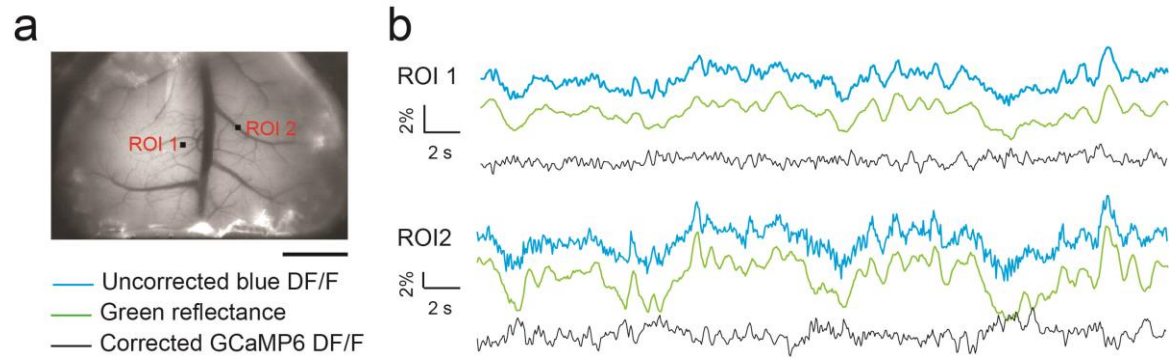

Figure 2.8: Hemodynamic correction of spontaneous signals. (a) Image of the dorsal cortex taken with mini-mScope of a Thy1-GCaMP6f mouse. Black squares indicate ROIs selected for hemodynamic corrections illustrated in **b**. Scale bar indicates 2 mm. **(b)** Uncorrected ΔF/F, reflectance ΔF/F and the hemodynamic corrected ΔF/F traces for the two ROIs shown in **a**.

We also benchmarked the signal-to-noise ratio (SNR) of the two instruments by imaging stimulus evoked activity. To compare the SNR of the mini-mScope to a conventional macroscope, we performed experiments in which a Thy1-GCaMP6f mouse lightly anesthetized with isoflurane was imaged using the mini-mScope and a conventional epifluorescence macroscope in the same experimental session when presented with vibrational stimulus or visual stimulus (**Fig. 2.9**). To evaluate the response to vibrational stimuli, a 1 s vibrational stimulus was provided to the hindlimb using a 3V DC mini vibration motor at 100 Hz. For a visual stimulus, a yellow LED was positioned ~ 2 cm from the left eye of the mouse to cover the fovea in the visual field. 100 ms flashes of light were presented after ensuring light from the LED was shielded to confine stimulus delivery to the left eye.

To analyze the data, a time stamp file generated during the experiment was used to segment this video into its respective trials. We detrended and spatially filtered each individual

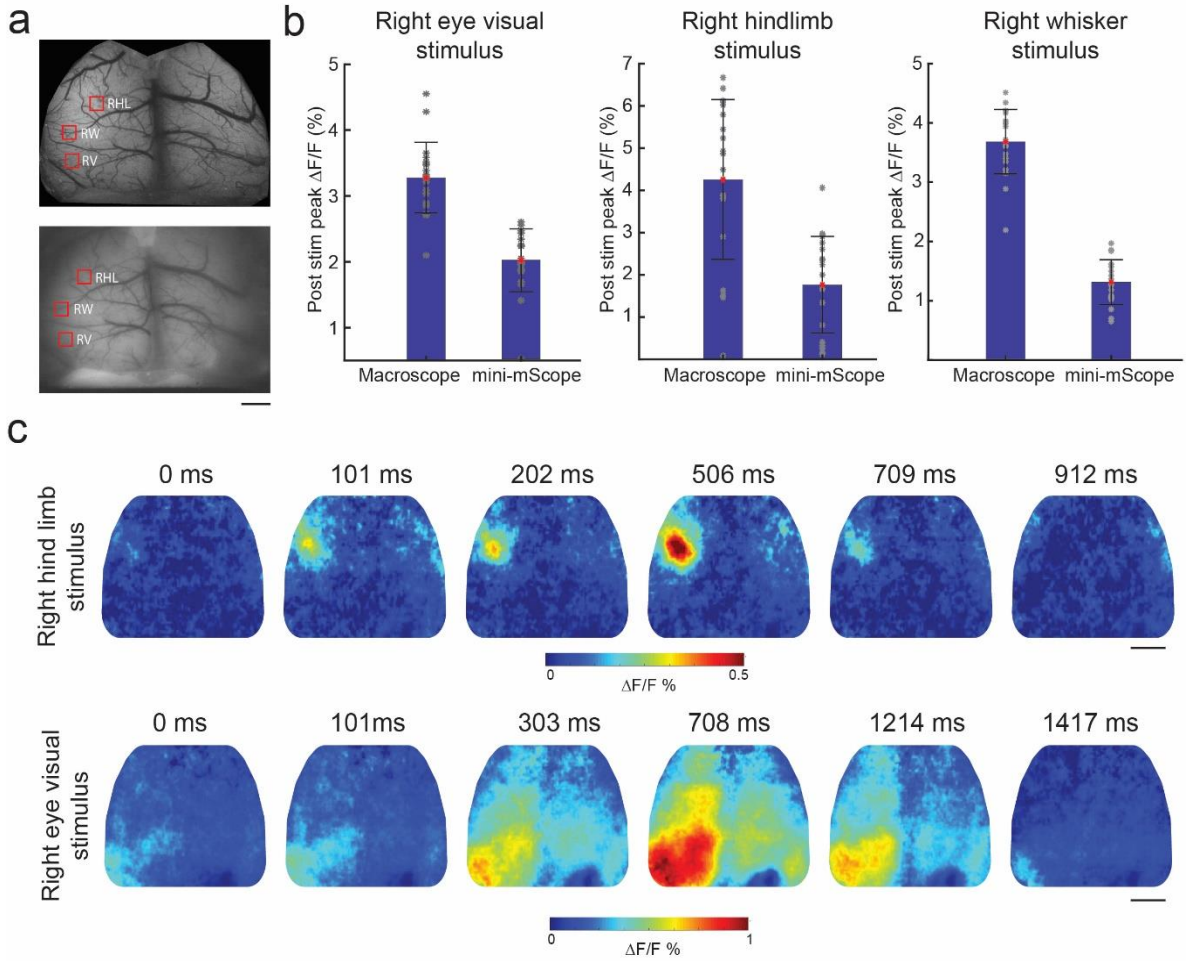

Figure 2.9: Sensory evoked stimulus across the cortex in anesthetized mice using the mini-mScope and a macroscope. **(a)** Photographs of the cortex of a Thy1-GCaMP6f mouse under anesthesia using a conventional macroscope (*top*) and the mini-mScope (*bottom*)**.** Red squares indicate ROIs selected for ΔF/F signals analyzed in **b**. Scale bar, 2 mm. **(b)** Mean post-stimulus peak ΔF/F signals of sensory evoked stimuli for the visual stimulus (*left*), hindlimb sensory stimulus (*middle*), and a whisker stimulus (*right*). Mean values are shown with red dots; error bars denote mean ± SD (n = 20 trials in one mouse, data is representative from 4 mice). **(c)** Average time series pseudocolor mean ΔF/F images showing glutamate signals from sensory evoked stimuli from Emx-CaMKII-Ai85 mice for right hind limb stimuli and right visual stimuli (n = 20 trials in one mouse, data is representative from 4 mice). Scale bar 3 mm.

trial using a custom weighted spatial filter to remove additional illumination artifacts from the

LEDs. The resulting ΔF/F data for each trial was saved to a .csv file and then averaged into a single .csv ΔF/F file.

The SNR was defined as the peak signal from the sensory evoked response divided by the baseline noise as calculated in previous literature (Grewe et al. 2010). This was calculated as the maximum intensity of the post-stimulus peak minus the mean intensity in the trial divided by the standard deviation of the intensity in the trial. To perform these experiments, we conducted additional trials in which we measured three different sensory stimuli evoked activity in the same experimental session using both instruments. In response to a visual stimulus presented to the right eye, the average peak ΔF/F response in the contralateral visual cortex was 2.1% ± 0.48% as measured by the mini-mScope. In comparison, the conventional macroscope reported an average peak ΔF/F response of 3.2% ± 0.52% in the same region. Similarly, when mice were presented with a vibrational stimulus to the right hindlimb, the average peak ΔF/F response in the contralateral hindlimb area of the somatosensory cortex was 1.8% ± 1.14% as measured by the mini-mScope. In comparison, the conventional macroscope reported an average peak ΔF/F response of 4.25% ± 1.90% at the same region. When a somatosensory stimulus was presented to the right whisker, the resulting average peak ΔF/F in the left barrel cortex as measured by the mini-mScope was 1.3% ± 0.38%. The average peak ΔF/F in the left barrel cortex as reported by the conventional macroscope was 3.7% ± 0.54%. This translated to a SNR of 3.8, 3.5, and 3.5 in the visual cortex, hindlimb area, and barrel cortex respectively for the mini-mScope. This compared to a SNR of 4.3, 5.0, and 3.7 in the visual cortex, hindlimb area, and barrel cortex respectively when measured using the conventional macroscope. Thus, the mini-mScope can measure localized responses to sensory stimulus, as evidenced by the substantial differences between the contralateral and ipsilateral responses. The mini-mScope resulted in lower peak ΔF/F values compared to the conventional macroscope. This could be attributed to substantial differences in the quantum efficiencies of the two sensors at the wavelengths being imaged (48%

at 500 nm, mini-mScope sensor, 78% at 500 nm, conventional macroscope sensor). Both image sensors used pixel of comparable sizes (6 µm x 6 µm for the mini-mScope, versus 6.4 µm x 6.4 mm in the conventional macroscope). Future versions of mini-mScope could thus alleviate this

performance deficit by incorporating higher performance sensors that are being incorporated in miniaturized imaging devices (Juneau et al. 2020).

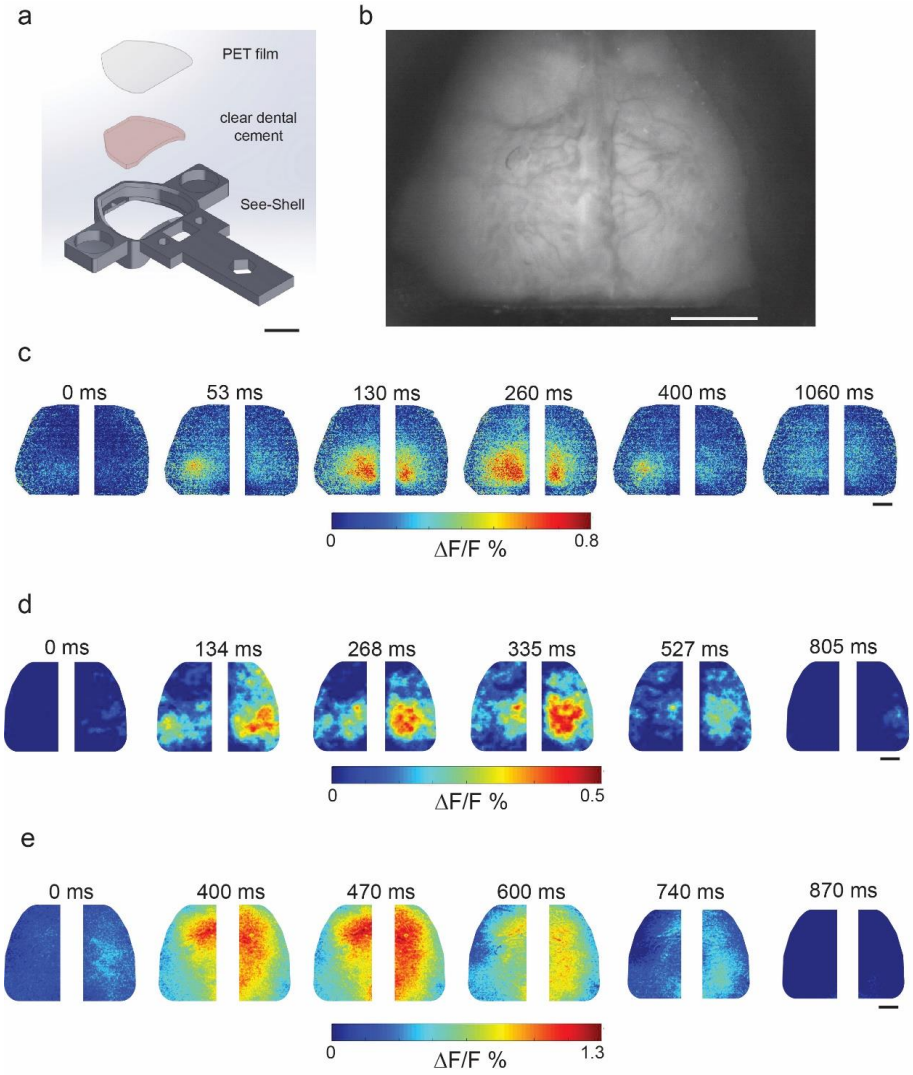

Figure 2.10: Sensory evoked stimuli through the intact skull using the mini-mScope. **(a)** A CAD schematic illustrating the modifications to the mini-mScope See-Shell for intact skull calcium imaging. Scale bar, 4 mm. **(b)** Photo of the cortex of a mouse through the intact skull imaged during sensory evoked stimuli experiments. Scale bar, 2 mm. **(c)** Average time-series ΔF/F pseudocolor graphs of the cortex showing calcium imaging during visual stimuli in anesthetized mice through the intact skull (n=20 trials in one mouse, data is representative from 3 mice). Scale bar 2 mm. **(d)** Average time-series pseudocolor graphs of the cortex showing calcium ΔF/F traces from imaging during visual stimuli in awake mice through the intact skull (n=20 trials in one mouse, data is representative from 3 mice). Scale bar 2 mm. **(e)** Average time-series pseudocolor graphs of the cortex showing calcium ΔF/F traces from imaging during auditory stimuli in awake mice through the intact skull (n=20 trials in one mouse, data is representative from 3 mice). Scale bar 2 mm.

Furthermore, the mini-mScope was also able to perform imaging through a modified intact skull (**Fig. 2.10**)**.** These results demonstrate that the mini-mScope can acquire calcium signals that are comparable to a conventional epifluorescence macroscope.

Imaging sensory stimulus evoked responses across the cortex

Stimulating distinct sensory pathways evokes neural activity in specific primary sensory areas located within the dorsal cortex. Providing a mouse under light (<1%) isoflurane anesthesia

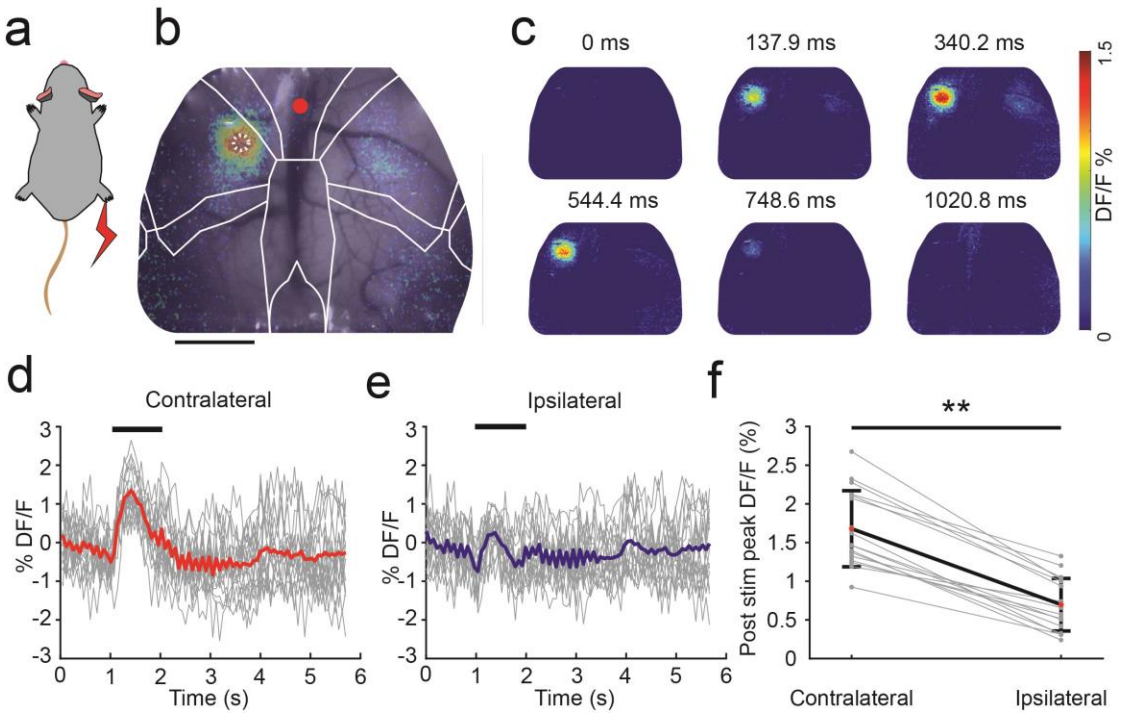

Figure 2.11: Somatosensory stimulus evoked responses imaged by the mini-mScope. **(a)** Schematic of an anesthetized Thy1-GCaMP6f mouse with a vibrational stimulus applied to the right hind limb. **(b)** Composite of raw grayscale image of the brain and the pseudo-color frame where the largest average ΔF/F occurred within the 1-second stimulus period. White circle indicates ROI analyzed in **d** and **e**. Red dot indicates Bregma. Scale bar 3 mm. **(c)** Montage of average cortical calcium response to the vibration stimulus. Scale bar 2 mm. **(d)** ΔF/F traces of the contralateral ROI drawn in **b**. Red line denotes the average traces, grey lines denotes individual trials. Black bar shows the time and duration of the vibrational stimulus. **(e)** ΔF/F traces of ipsilateral ROI drawn in **b**. Blue line denotes the average response, grey lines denote each individual trial. **(f)** Peak ΔF/F within 1-second of vibration stimulus presentation (n=20 trials in one mouse, data is representative of 3 mice). ** indicates $p < 0.01$, $p = 9.1 \times 10^{-3}$, two-sample t-test.

with a series of brief vibrational stimuli (1s long, 100 Hz) to the right hind limb (**Fig. 2.8xa**), evoked

robust calcium activity in the contralateral hind limb (HL) region of the somatosensory cortex within 500 ms of the onset of stimulus (**Fig. 2.11b-c**).

The peak post stimulus response was 1.68% ± 0.49% ΔF/F (**Fig. 2.11d**, n = 17 trials in 1 mouse). In comparison, the peak post-stimulus response on the ipsilateral side was significantly

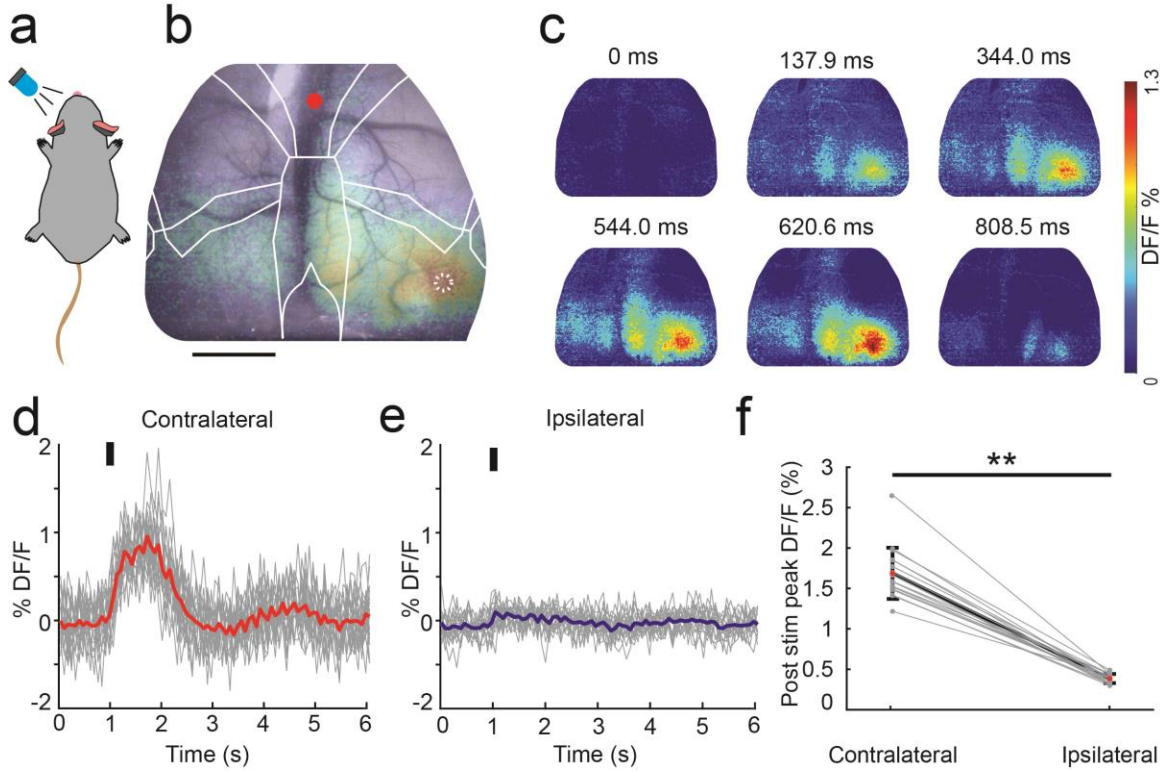

Figure 2.12: Visual stimulus evoked responses imaged by the mini-mScope. (a) Schematic of a mouse with a visual stimulus applied to the left eye. **(b)** Composite of raw grayscale image of the brain and the pseudo-color frame where the largest average ΔF/F occurred within the 1-second stimulus period. White circle indicates ROI analyzed in **d** and **e**. Scale bar 3 mm. Data were acquired in the same mouse as the data in a to f. **(c)** Montage of average cortical calcium response to the visual stimulus. Scale bar 2 mm. **(d)** ΔF/F traces of the contralateral ROI drawn in **h**. Red line denotes the average trace, grey lines denote each individual trial. Black bar shows the time and duration of the visual stimulus. **(e)** ΔF/F traces of ipsilateral ROI drawn in **h**. Blue line denotes average ipsilateral response, grey lines denote individual trials (n=20 trials in one mouse, data is representative of 3 mice). **(f)** Peak ΔF/F within 1-second of visual stimulus presentation. The bolded line corresponds to the average peak response whereas the grey lines indicate the peak response for each trial. ** indicates $p < 0.01$, $p = 1.31 \times 10^{-5}$, two-sample t-test.

lower (0.70% ± 0.34% ΔF/F, **Fig. 2.11e-f**, $\alpha = 0.05$ for significance, $p < 0.01$, $p = 9.1 \times 10^{-3}$, paired t-test). We presented the same mouse with 100 ms long flashes of white light to the left eye (**Fig.**

2.12a), evoking a robust increase in calcium activity in the contralateral visual cortex (**Fig. 2.12b-c**). The peak post stimulus response was 1.7% ± 0.32% ΔF/F (**Fig. 2.12d**, n = 18 trials). In comparison, the peak post-stimulus response on the ipsilateral visual cortex was significantly lower (0.38% ± 0.057% ΔF/F**, Fig. 2.12d-f**, $\alpha = 0.05$ for significance, $p < 0.01$, $p = 1.31 \times 10^{-5}$, paired t-test).

We also performed experiments to test whether visual and auditory stimulus evoked activity could be measured in mice freely locomoting in an open field using the mini-mScope. An array of yellow LEDs was used to present 100 ms long flashes of light every 10 s to mice bearing the mini-mScope freely locomoting in a dark open field arena. Peak responses in visual and association areas are illustrated in **Figure 2.13**.

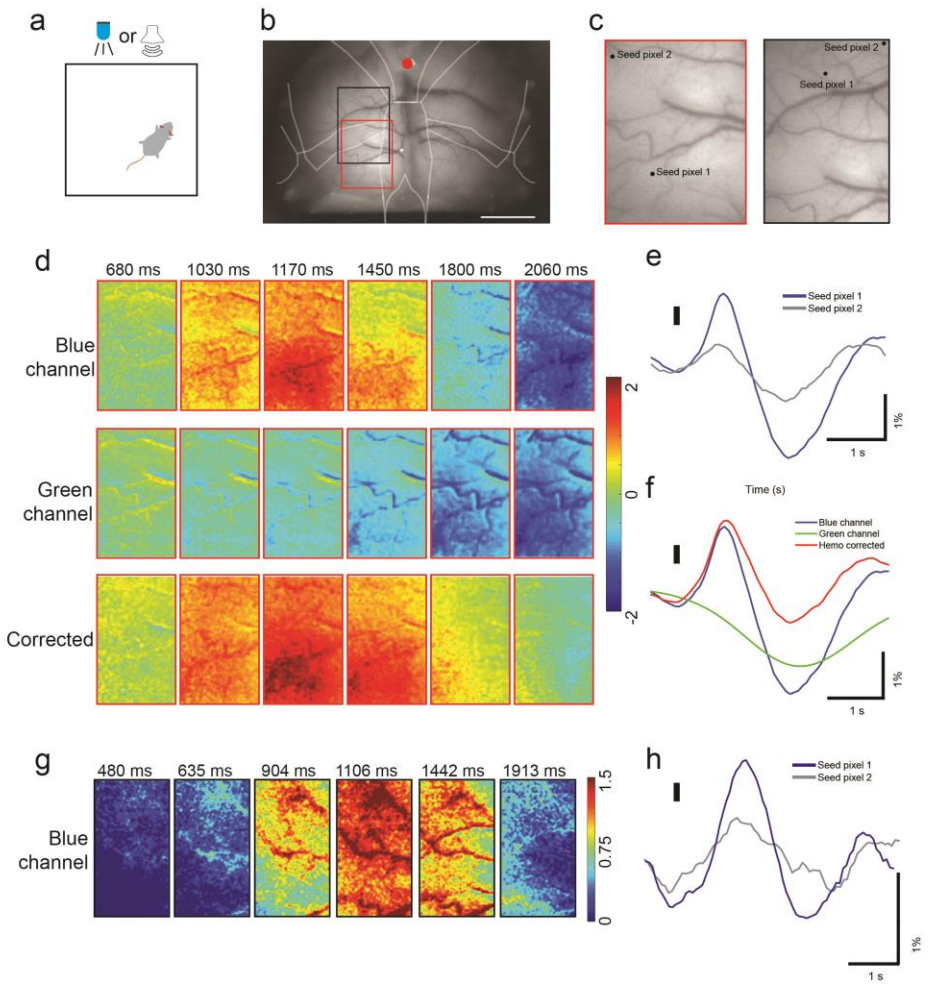

Figure 2.13: Sensory evoked stimuli in awake mice. (a) An illustration of the experimental setup; a mouse was placed in an open arena and presented with visual or auditory stimuli in regular intervals. **(b)** Photo of the cortex of a mouse imaged during the sensory evoked stimuli during awake behavior experiments. The red rectangular region was selected for further analysis in trials which a visual stimulus was applied, and the black rectangle encloses the region selected for trials which auditory stimulus was applied. Scale bar, 2 mm. **(c)** Close up of the cortical regions enclosed by the rectangles drawn in **b**. Two seed pixels were selected to extract ΔF/F traces in each region indicated by the dots. Scale bar 0.5 mm. **(d)** Average time series pseudocolor graphs of the red rectangular ROI from **b** showing mean uncorrected calcium ΔF/F traces, reflectance ΔF/F, and calcium ΔF/F with hemodynamic correction from trials where visual stimuli were presented (n=20 trials in one mouse, data is representative of 4 mice). Scale bar 0.5 mm. **(e)** A graph comparing calcium ΔF/F traces from two seed pixels selected indicated in the red rectangle in **(c)**. The dashed line denotes when the visual stimulus was presented. **(f)** A graph showing the uncorrected calcium ΔF/F (blue channel), reflectance signal (green channel), and the hemodynamic corrected signal for seed pixel 1 from **c**. The dashed line denotes when the visual stimulus was presented. **(g)** Average time series pseudocolor graphs of the black rectangular ROI from **b** showing mean uncorrected calcium ΔF/F traces from trials which auditory stimuli were presented (n=20 trials in one mouse, data is representative of 4 mice). Scale bar 0.5 mm. **(h)** A graph comparing calcium ΔF/F traces from two seed pixels selected indicated in the black rectangle in **c**. The dashed line denotes when the auditory stimulus was presented.

average, we found that there was an increase in calcium activity in response to the stimulus, followed by a decrease relative to baseline with a peak post stimulation ΔF/F response of 1.95 ± 1.27 (n = 20 trials) in seed pixel 1. Responses were relatively diminished in the second seed pixel located anterior within the selected ROI (**Fig. 2.13e**), with the signals in the green reflectance channel lagging the calcium response (**Fig. 2.13f**). Similarly, a 13 KHz tone was presented to the same mice for 50 ms every 10 s. Auditory stimuli resulted in broad activation of much of the dorsal cortex, consistent with previous studies (Mohajerani et al. 2013). These results indicate that the mini-mScope can image stimulus evoked calcium activity in freely behaving animals. The responses were more variable owing to the awake state, but we nevertheless obtained distinct responses. Thus, the mini-mScope can reliably measure evoked responses to varied sensory stimuli in both hemispheres of the dorsal cortex.

Effect of mounting a mini-mScope on behavior and imaging stability

We next assessed if either implanting the see-shell or mounting the mini-mScope affected behavior in both long-term and short-term experiments.To assess whether the implantation of the See-Shell and head-mounting the mini-mScope affected behavior, we used an open field behavior test. Mice bearing the mini-mScope were allowed to freely move in an open field arena for up to 5 minutes. We performed behavioral tracking using an overhead camera in the arena, and then used traces from the recordings to quantify the mean speed, total distance, maximum speed, and time spent in the center of the open field (**Fig. 2.14**). Mice bearing the mini-mScope moved with an average speed of 4.56 ± 2.07 cm/s. In comparison, See-Shell implanted mice without the mini-mScope moved at an average speed of 4.94 ± 1.63 cm/s. There was no significant difference in average speed between both groups compared to the non-surgical control mice group, which moved with an average speed of 4.22 ± 1.24 cm/s ($\alpha = 0.05$ for significance, $p = 0.569$ between implant and control, $p = 0.472$ between mini-mScope and control, paired t-test). Similarly, we

tracked the total distance moved in 5-minute trials. Mice bearing the mini-mScope moved a total distance of 1374.15 ± 623.40 cm. In comparison, See-Shell implanted mice without the mini-mScope moved 1492.65 ± 496.09 cm. There was no significant difference in total distance travelled between both groups compared to that from control mice ($\alpha = 0.05$ for significance, $p = 0.059$ between implant and control, $p = 0.4937$ between mini-mScope and control, paired t-test).

Mice bearing the mini-mScope had an average maximum speed of 49.08 ± 16.48 cm/s. In comparison, See-Shell-implanted mice without the mini-mScope had an average maximum speed of 53.06 ± 8.75 cm/s. There was no significant difference in maximum speed between both groups and the control mice (α = 0.05 for significance, p > 0.05, p = 0.06 between implant and control, p = 0.49 between mini-mScope and control, paired t-test). There was a statistically significant

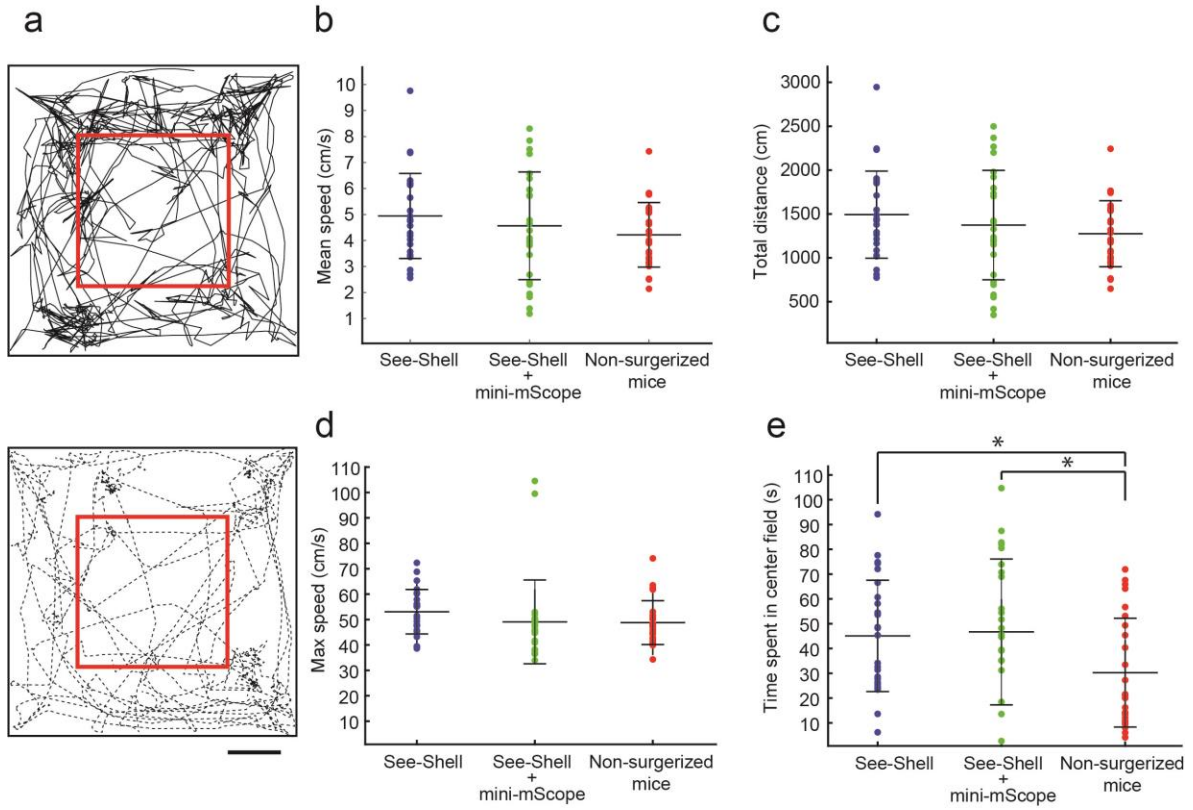

Figure 2.14: Head-mounting the mini-mScope has minimum effect on open field behavior. (a) Trace of mouse position in a 5-minute trial. *Top:* See-Shell implanted mouse without the mini-mScope. *Bottom:* Mouse bearing head-mounted mini-mScope. Red box indicates region of the arena denoted as the open field. Scale bar indicates 5 cm. **(b)** Plot of mean speed ± SD of mice with a See-Shell implanted, mice with both the See-Shell and head-mounted mini-mScope, and non-surgerized control mice (n=5 mice per group, 5 trials per mouse). **(c)** Plot of total distance ± SD traveled by mice with a See-Shell implanted, mice with both the See-Shell and head-mounted mini-mScope, and non-surgerized control mice (n=5 mice per group, 5 trials per mouse). **(d)** Plot of maximum speed ± SD of mice with a See-Shell implanted, mice with both the See-Shell and head-mounted mini-mScope, and non-surgerized control mice (n=5 mice per group, 5 trials per mouse). **(e)** Plot of time spent at the center of the open field ± SD by mice with a See-Shell implanted, mice with both the See-Shell and head-mounted mini-mScope, and non-surgerized control mice (n=5 mice per group, 5 trials per mouse). * indicates p<0.05, p = 0.01 implant vs non-surgerized control mice, p = 0.02 mini-mScope vs non-surgerized control mice, two sample t-test.

difference between the time control mice spent in the open field versus mice with the See-Shell implant and mice with the mini-mScope (α = 0.05 for significance, p=0.01 for See-Shell vs non-surgerized mice, p=0.02 for mini-Mscope vs non-surgerized mice, paired t-test). Tests of how the mini-mScope or See-Shells affect anxiety levels would require the open field arena test to be used in conjunction with other behavioral tests (Ramos 2008).

In a second set of experiments, we evaluated if bearing the mini-mScope over longer

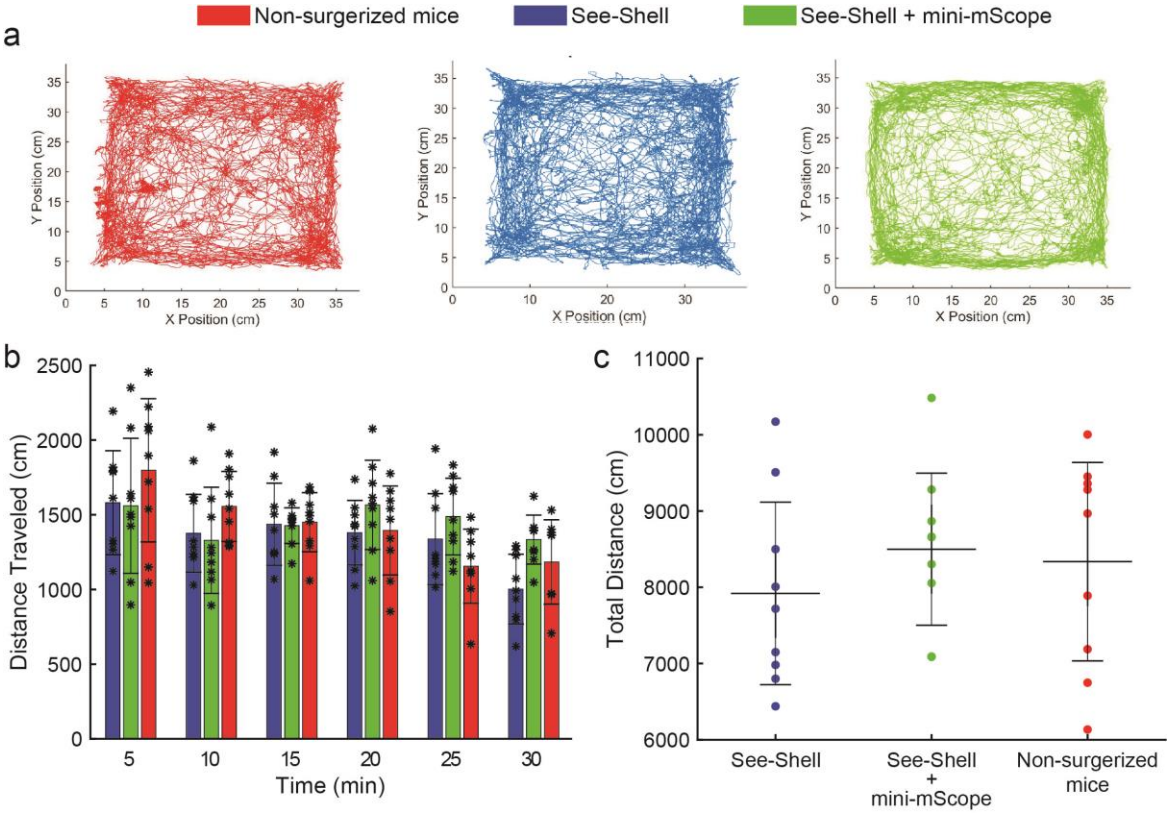

Figure 2.15: Head-mounting the mini-mScope has minimum effect on locomotion in longer experiments. (a) Traces obtained via tracking mouse behavior in an open field arena for 30 minutes for non-surgerized mice, mice implanted with the See-Shell implant, and mice implanted with the See-Shell and bearing the mini-mScope. **(b)** A graph depicting the mean distance ± SD traveled by mice in five-minute epochs during a 30-minute trial (n=3 mice per group, 3 trials per mouse). **(c)** A graph showing the total distance traveled by mice in an entire 30-minute trial (n=3 mice per group, 3 trials per mouse).

durations of time affected mouse behavior. Mice were allowed to explore the open field for 30-minute trials over three days. We found that the total distance moved by the mice were not significantly different across the three groups (**Fig. 2.15**, n = 3 mice, 3 trials, α = 0.05 for

significance, $p > 0.05$. $p = 0.10$ between implant and mini-mScope, $p = 0.54$ between implant and control, $p = 0.81$ between mini-mScope and control, paired t-test). In all groups, there was an overall increase in the total distance moved as the trials progressed, but there were no discernible differences in these trends.

We next assessed if light leakage from the LED affects locomotion. Mice were placed (n = 3 mice, 1 trial each) in the open field arena for 2 minutes with and without the LEDs switched on. We found that, on average, mice traveled 1004.7 cm with the LEDs off and 1015.9 cm with the LEDs on in this time. Thus, light leakage does not appear to influence the behavior of the mouse. These results indicate that the mini-mScope has little to no effect on the free behavior of the mice, consistent with results obtained with other miniaturized head-mounted imaging devices (Skocek et al. 2018).

We also assessed the stability of the images captured using the mini-mScope during free behavior. Experiments related to free behavior can cause motion artifacts due to two issues: the mini-mScope's movement relative to the implant or the brain's movement relative to the implant. When the mini-mScope was attached with the mounting screw on the rear tab, there were minimal

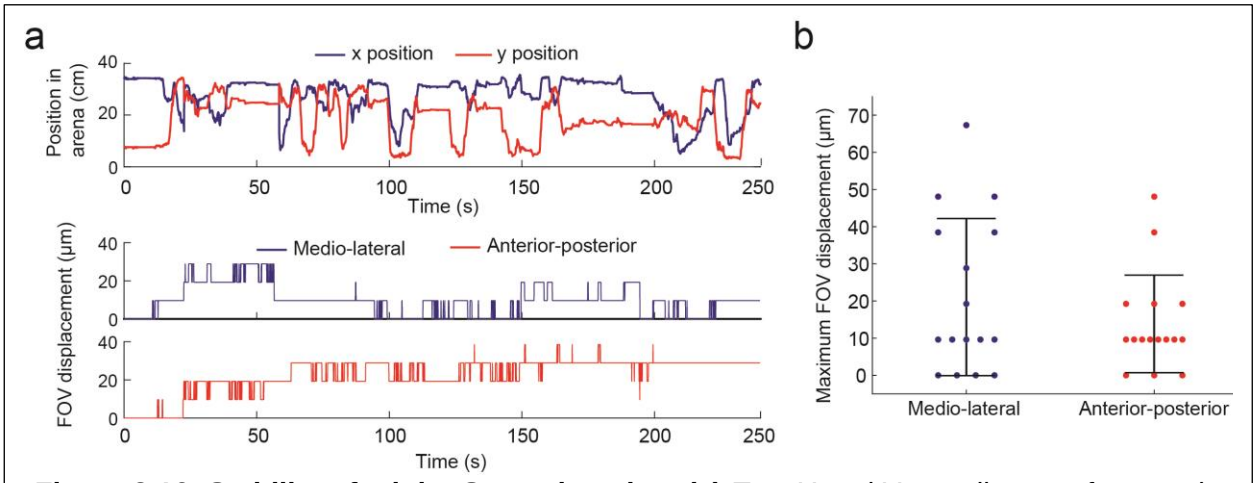

Figure 2.16: Stability of mini-mScope imaging. (a) *Top:* X and Y coordinates of mouse in a 30cm by 30cm open field arena during a 4-minute trial. *Bottom:* Rigid translations of the mini-mScope FOV to correct for motion artifacts in the calcium dynamics video corresponding to the mouse behaving with the positions depicted in *Top*. **(b)** Maximum rigid translations of mini-mScope FOV to correct for motion artifacts in calcium dynamics videos (n = 16 videos). Error bars denote mean ± SD.

lateral motion artifacts while the mouse was performing vigorous behaviors such as rearing and grooming. Imaging stability was analyzed using the MoCo plugin in FIJI to obtain pixel displacements and a motion-corrected video. The absolute maximum x and y displacements of the FOV were 21.0 ± 21.8 µm and 14.4 ± 17.1 µm, respectively (**Fig. 2.16**, n = 3 mice, 3 trials each). The mean absolute x and y displacement were 2.0 ± 2.5 µm and 9.3 ± 4.9 µm, respectively. These motion artifacts were adequately corrected for using a rigid body motion correction algorithm (Dubbs et al. 2016).

Limitations on the weight of the device precluded us from adding any more instrumentation such as a laser range finder (Murphy et al. 2016) to measure z-axis deflection. However, based on the numerical aperture of the collector lens, the mini-mScope's depth of focus ranges from ~120 µm near the optical axis to ~180 µm in more lateral regions of the FOV. Thus, small fluctuations in the z-direction should be within the depth of focus of the device.

While it is possible for the brain to move relative to the implant, our previous study has demonstrated that the brain is stable enough across much of the dorsal cortex to enable 2P imaging of single neurons in awake head-fixed animals (Ghanbari et al. 2019a). Fluctuations of the brain position relative to the implant larger than 100 µm should be easily perceptible to the

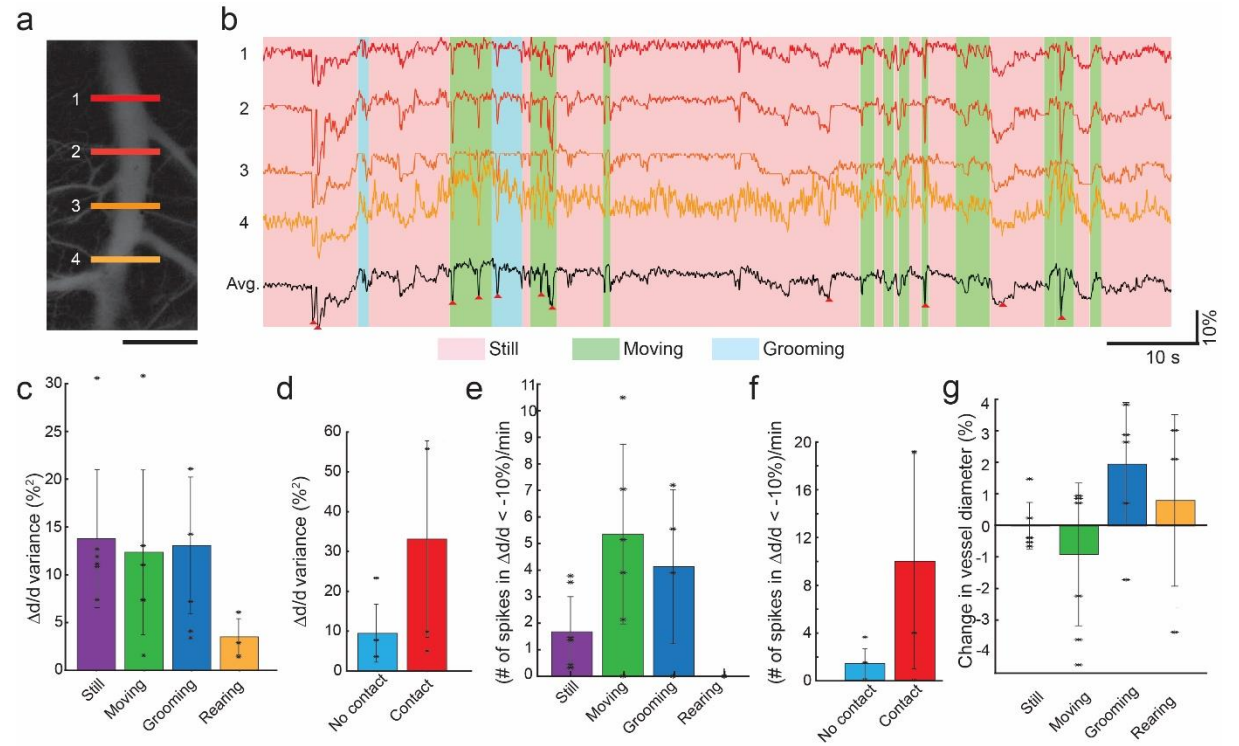

Figure 2.17: Tracking diameter of superior sagittal sinus (SSS) during free and social behavior. (a) Image of SSS in the dorsal cortex. Numbered lines indicate cross sections selected for diameter tracking analysis in **b**. Scale bar, 1 mm. **(b)** Time series evolution of percentage change of vessel diameter at the cross sections specified in **a** and their average during still, moving, and grooming behaviors. Red triangles along the average trace indicate spikes exceeding 10% prominence. **(c)** Bar graph of the variance in percentage change of vessel diameter (n = 3 mice, 6 trials total) by behavior. Error bars denote mean ± SD. **(d)** Bar graph of the variance in percentage change of vessel diameter by social activity (n=3 mice, 3 trials total). Error bars denote mean ± SD. **(e)** Bar graph of the rate of occurrence of 10% prominence spikes by behavior (n = 3 mice, 6 trials total). Error bars denote mean ± SD. **(f)** Bar graph of the rate of occurrence of 10% prominence spikes by social activity (n = 3 mice, 3 trials total). Error bars denote mean ± SD. **(g)** Bar graph of the percent change in vessel diameter by behavior (n = 3 mice, 6 trials total). Error bars denote mean ± SD.

naked eye. In this study, as well as our previous work (Ghanbari et al. 2019a), such large fluctuations were not observed.

The mini-mScope images the cortex through the transparent See-Shell implants, allowing relatively high-resolution imaging of the surface cerebral vasculature compared to intact skull imaging. In raw calcium activity imaging videos acquired during freely moving behavior, we observed large changes in the diameter of the superior sagittal sinus (SSS) that were perceptible to the naked eye. Using image processing, we analyzed the changes in diameter of the SSS at various locations (**Fig. 2.17**).

SSS diameter tracking was performed using a custom written macro in FIJI. Blue channel videos were inverted, and the background was subtracted using a rolling ball radius of 30 pixels. A rectangular ROI was then drawn around the area to be analyzed. The rectangle was used as a guide to create 6 evenly spaced, horizontal lines along the height of the rectangle. The lines were 5 pixels thick and as long as the width of the rectangle. These lines were used as ROIs to track the vessel diameter throughout a trial (**Fig. 2.16a**-**b**). To calculate the diameter, the intensity profile along a line was first plotted. Then, the maximum intensity and its corresponding location in pixels along the line was found. Using half of the maximum intensity as a threshold, the macro then searched for the pixel with the lowest intensity greater than the threshold in both directions from the maximum intensity. The difference between the pixel locations of these two values was then stored as the vessel diameter. This process was repeated for each line and each frame in a video. Values were saved in a .csv file for further analysis.

Post-processing and plotting of data were performed in MATLAB. The percent change in vessel diameter ($\Delta d/d$) was calculated for 4 ROIs (**Fig. 2.17a**). The baseline was the average vessel diameter across time at each ROI. Time-series of diameter changes were then plotted as 5-point moving averages along with the average of those traces (**Fig. 2.17b**). Behavior data was plotted using the consensus among scorers and then padding the behavior epochs on either side by ~0.5 s (7 frames). Spikes with prominence greater than 10% and longer than 1/3 s were

detected using MATLAB. Variances shown in **Figure 2.17c** and **d** were calculated by first pooling the variances from behavior epochs to obtain a variance for each behavior within a trial. The weighted average of these variances was then taken across trials to obtain a single measure for each behavior.

A Wilcoxon signed-rank test was performed on variances from still, moving, grooming, and rearing behavior. A paired sample t-test was performed on spike frequencies from still, moving, and grooming behavior. Statistical tests were not performed for social behavior plots due to the small number of samples (n = 3).

Representative traces of the time-series of SSS diameter during an open field behavior trial are shown in **Figure 2.17b**. The measured diameters varied throughout the trial and the variance in percentage change in vessel diameter was comparable when the mice remained stationary, were moving or grooming (n = 6 trials, 3 mice) (**Fig. 2.17c**). There was no statistically significant difference between the groups ($p > 0.05$, $p = 0.43$ moving vs still, $p = 0.13$ grooming vs still, $p = 0.25$ rearing vs still, $p = 0.31$ grooming vs moving, $p = 0.25$ rearing vs moving, $p = 0.5$ grooming vs rearing, Wilcoxon signed-rank test). The variance increased during social contact (n = 3 trials, 3 mice) (**Fig. 2.17d**). In all trials, we further observed rapid (<0.5 s) and large (>10%) contractions in the SSS. We initially hypothesized that they may occur during motion artifacts caused by behavior. However, such spike-like reductions in diameters were observed even when the mice were stationary (**Fig. 2.17e**). Like the variances, there was no statistically significant difference between the spike frequencies ($p > 0.05$, $p = 0.06$ moving vs still, $p = 0.31$ grooming vs still, $p = 0.07$ moving vs grooming, paired sample t-test). A consequence of this observed phenomenon was that the areas adjoining the SSS had large lateral motion artifacts that could not be corrected using rigid body motion correction algorithms. Thus, areas within ~500 μm were excluded in our data analyses of calcium activity.

Mapping cortical functional connectivity during open field exploration and social interactions

We used the mini-mScope to examine functional connectivity between cortical areas during open field behavior of solitary mice and during social interactions with a companion mouse

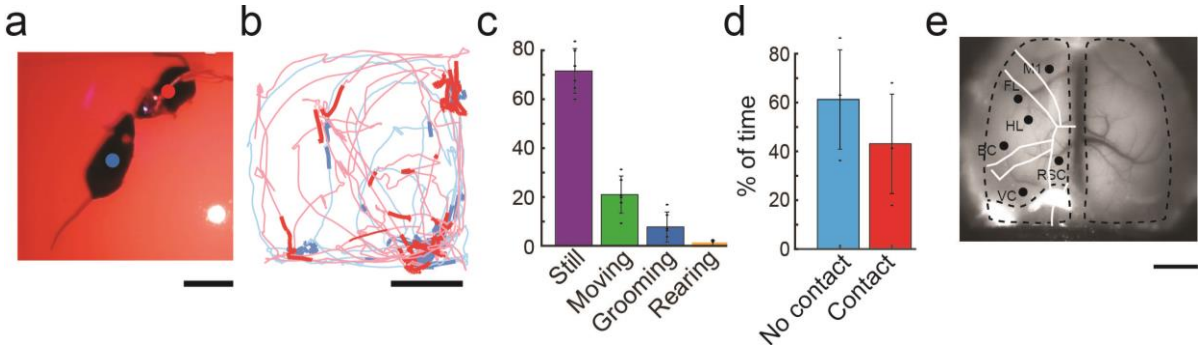

Figure 2.18: Mesoscale imaging of cortex during free and social behavior. (a) Photograph of a mouse with a mini-mScope (red dot annotation) interacting with a companion mouse (blue dot annotation). Scale bar, 5 cm. **(b)** Traces of instantaneous locations of the two mice during trial. The segments of darker blue and red indicate positions of the mice when they were within 5 cm of each other. Scale bar, 10 cm. **(c)** Percentage of time spent still, moving, grooming, and rearing during open field behavior (n = 6 trials). **(d)** Percentage of time spent in contact and not in contact with the companion mouse behavior during trials (n = 3 trials). **(e)** Representative image of the cortex with locations of the seed pixels used for analysis in **Figure 2.14** are indicated. Scale bar 2 mm

(**Fig. 2.18a-b**). We segregated solitary open field trials into four types of behaviors – periods when mice were still, moving, grooming, or rearing. On average, mice spent 70.6% ± 9.0% of the time remaining still (n = 11 trials, 3 mice), while spending 20.7% ± 7.51% of the time moving within the arena. Grooming and rearing were less frequent and shorter in durations, accounting for 7.7% ± 6.02% and 1.04% ± 1.17% of the time respectively (**Fig. 2.18c**). To study social behavior, we allowed mice bearing the mini-mScope to first explore the arena before we introduced a companion mouse of the same sex (n = 8 trials, 8 mice). Mice spent 41.3% ± 19.5% of time socially interacting with each other, including touching whiskers or the body (**Fig. 2.18d**).

We constructed hemodynamics-corrected seed-pixel correlation maps of the cortex from the calcium activity videos during open field behavior. We analyzed maps with respect to six seeds within the motor cortex (M1), the forelimb (FL), the hind limb (HL), and the barrel cortex (BC) areas in the somatosensory cortex, the retrosplenial cortex (RSC), and the visual cortex (VC) (**Fig. 2.18e, Fig. 2.19a**). Correlations between the seed locations changed when the animal was moving versus still. Between the seeds, correlations increased, particularly between those

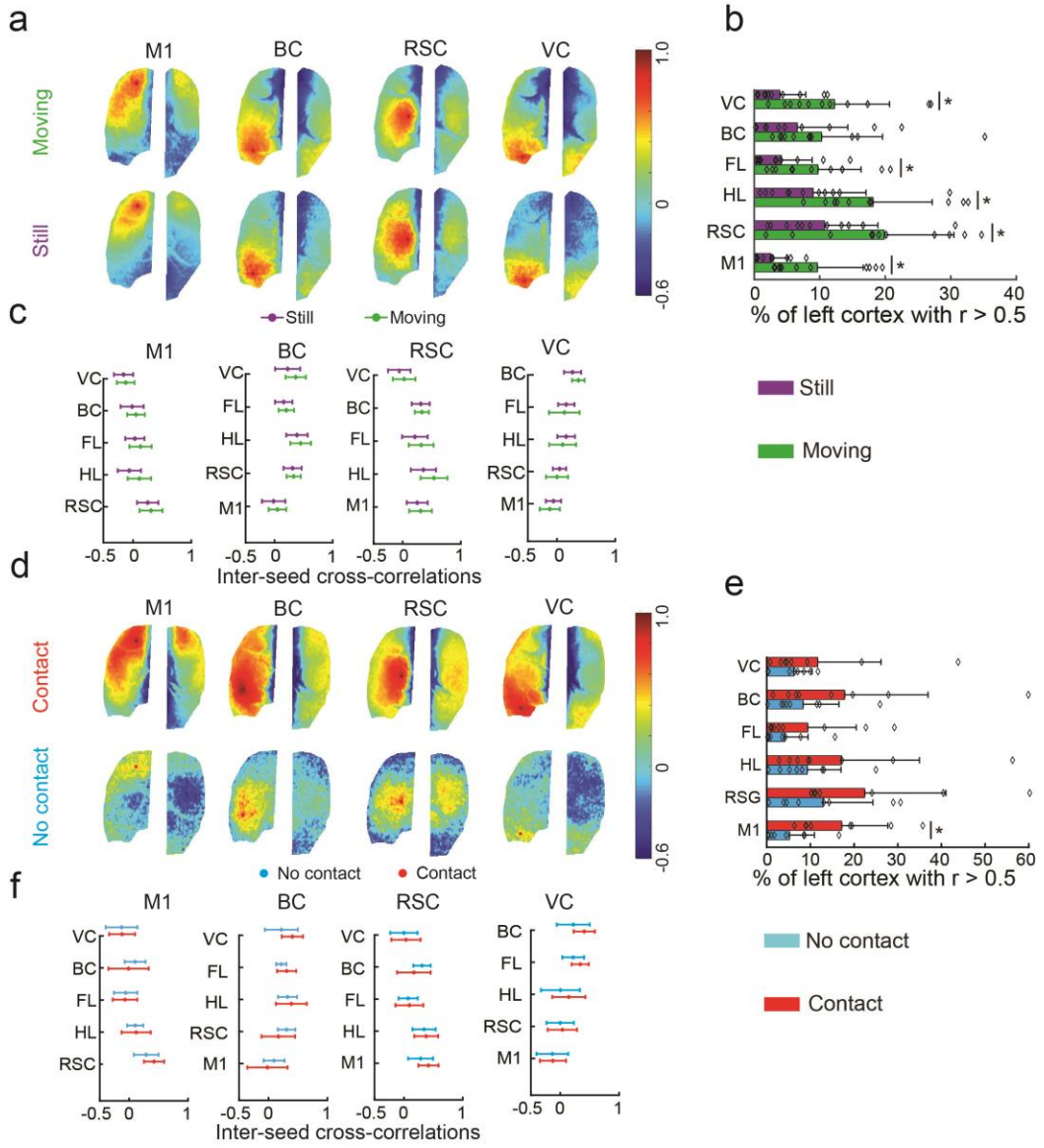

Figure 2.19: Mesoscale calcium dynamics during free and social behavior. (a) Seed pixel correlation maps of motor cortex (M1), barrel cortex (BC), retrospenial cortex (RSC) and visual cortex (VC) during movement and no movement. *Top row:* Average of correlations during 1 s epochs of movement; *bottom row:* Average of correlations during 1 s epochs of no movement. Scale bar 2 mm. **(b)** Change in percentage of hemisphere with r > 0.5 with respect to seed pixels analyzed. * indicates $p < 0.05$ ($p = 4.6 \times 10^{-3}$ M1, $p = 6.3 \times 10^{-4}$ FL, $p = 3.8 \times 10^{-3}$ HL, $p = 4.6 \times 10^{-3}$ RSC, $p = 0.10$ BC, $p = 1.1 \times 10^{-3}$ VC, two-sample Mann-Whitney U-test, n = 11 trials, n = 3 mice). Error bars denote mean ± SD. **(c)** Average inter-seed correlations associated with seeds (n = 11 trials, n = 3 mice). Error bars denote mean ± SD. **(d)** Seed pixel correlation maps of M1, BC, RSC and VC during non-social and social behavior epochs. Scale bar 2 mm. **(e)** Percentage of hemisphere with r > 0.5 with respect to seed pixels analyzed. * indicates $p < 0.05$ ($p = 0.048$ M1, $p = 0.17$ FL, $p = 0.058$ HL, $p = 0.091$ RSC, $p = 0.082$ BC, $p = 0.37$ VC, two-sample Mann-Whitney U-test, n = 8 trials, n = 8 mice). Error bars denote mean ± SD. **(f)** Average inter-seed correlations associated with the seeds (n= 6 trials, n = 6 mice). Error bars denote mean ± SD.

highly correlated with respect to a given seed location, increased for all seeds analyzed when the animal was moving (**Fig. 2.19b**) and these increases were found to be significantly higher for seeds located at M1, HL, FL, VC and RSC (n = 11 trials, 3 mice, $\alpha = 0.05$ for significance, $p < 0.05$, $p = 4.6 \times 10^{-3}$ M1, $p = 6.3 \times 10^{-4}$ FL, $p = 3.8 \times 10^{-3}$ HL, $p = 4.6 \times 10^{-3}$ RSC, $p = 0.10$ BC, $p = 1.1 \times 10^{-3}$ VC, Mann-Whitney U-test).

Overall, movement induced increased variance in the inter-seed correlations (**Fig. 2.19c**). Similarly, we constructed seed-pixel correlation maps for mice engaging in social behaviors (**Fig. 2.19d**). Intra-cortical connectivity was increased during times where the mice were engaged in social behaviors (**Fig. 2.19d-f**, n=8 mice, $\alpha = 0.05$ for significance, $p = 0.048$ M1, $p = 0.17$ FL, $p = 0.058$ HL, $p = 0.091$ RSC, $p = 0.082$ BC, $p = 0.37$ VC, Mann-Whitney U-test). These results demonstrate the utility of the mini-mScope to study functional connectivity during behaviors that are unique to freely behaving mice.

Imaging glutamate release dynamics during wakefulness and natural sleep

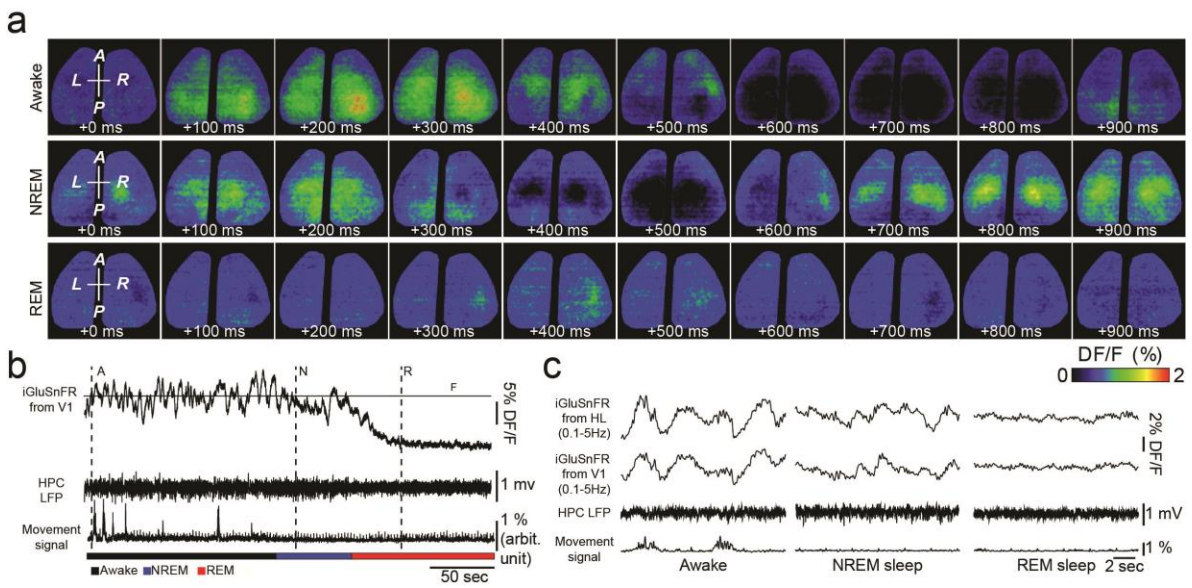

Figure 2.20: Combined electrophysiological recording and mesoscale imaging of brain activity during wakefulness and sleep. (a) Montages of change in glutamate activity over 1s period during awake, REM and NREM sleep states. Scale bar 2 mm. **(b)** Representative traces of raw glutamate signals from V1, hippocampal LFP, and video-based movement signals during states of waking, NREM sleep and REM sleep in a freely moving mouse. F_0 is the baseline glutamate signal calculated by averaging the fluorescence over the entire recording time. **(c)** Magnification of glutamate, LFP and movement signals selected in **b**.

As a final demonstration, we used the mini-mScope to measure dynamic changes in extracellular glutamate release in the cortex during transition from wakefulness to natural sleep. Much of the previous work studying extracellular glutamate release has been done using fixed-potential amperometry (Dash et al. 2009), or optical imaging in head-fixed mice (Abadchi et al. 2020). Inducing sleep in head-fixed mice is challenging and typically requires sleep deprivation which can alter the overall sleep structure and patterns of rapid eye-movement (REM) and non-REM (NREM) sleep (Patti et al. 2010, Colavito et al. 2013).

The flexibility of the See-Shells allowed us to incorporate local field potential (LFP) recording electrodes in the dorsal hippocampus in Emx-CaMKII-Ai85 mice, expressing iGluSnFR in glutamatergic neocortical neurons (Marvin et al. 2013). We allowed mice to naturally transition to sleep in their home cage and recorded glutamate activity across the whole dorsal cortex during wakefulness, REM sleep, and NREM sleep (**Fig. 2.20)**. Hippocampal LFP indicated transition to NREM sleep characterized by high amplitude slow waves (0.5-4 Hz) and subsequently REM sleep characterized by theta band activity (7 – 9 Hz, **Fig. 2.2b-c,**). Consistent with previous studies, spontaneous cortical activity patterns during quiet wakefulness and NREM were highly

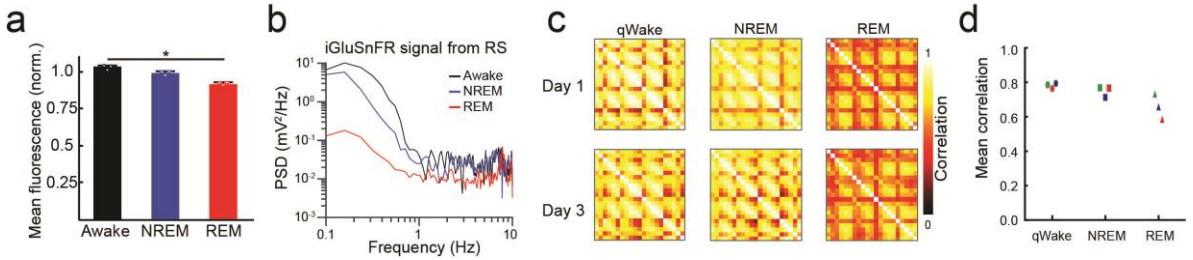

Figure 2.21: Analysis of electrophysiological recording and mesoscale imaging of brain activity during wakefulness and sleep. (a) Grouped mean raw glutamate signal from the entire cortex (normalized to baseline) during wakefulness, NREM sleep and REM sleep (n = 3 mice, Friedman paired nonparametric test; post-hoc multiple comparison with Dunn's correction * indicates $p < 0.05$, $p = 0.02$ wakefulness vs REM). **(b)** Spectral analysis of glutamate signal in three states. **(c)** Correlation maps of cortical activity between quiet wakefulness, NREM sleep and REM sleep at two different days. Cortex was divided into 21 ROIs. **(d)** Mean correlation of cortical activity during waking, REM and NREM sleep (n = 3 mice).

synchronized across hemispheres (Mohajerani et al. 2010). In addition, cortical activity changes were not necessarily due to global changes in state and were instead composed of complex local activity patterns (**Fig. 2.20a**). The transition from wakefulness to NREM sleep and REM sleep

resulted in decreased fluorescence, indicating reduced cortical glutamate activity (**Fig. 2.20a-c, Fig. 2.21a**).

We also observed a reduction of slow cortical glutamate fluctuations during REM sleep

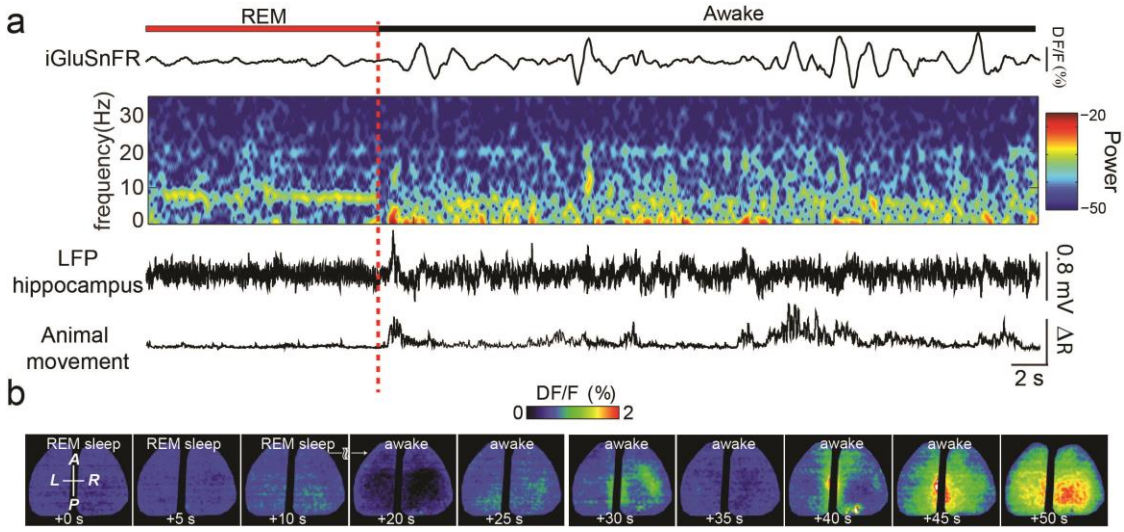

Figure 2.22: Changes in functional connectivity during wakefulness and sleep. (a) Glutamate activity, hippocampal LFP frequency spectrogram and animal movement tracking during transition from REM to wakefulness **(b)** Montage of cortical glutamate changes during the transition shown in **a**. Scale bar 2 mm.

(**Fig. 2.21b**). Correlation analysis of cortical activity revealed that connectivity decreases in REM sleep compared to quiet wakefulness and NREM sleep (**Fig. 2.21c-d**). Moreover, consistent with previous studies, the strength of functional connectivity was less in NREM sleep compared to quiet wakefulness (Mohajerani et al. 2010). The mini-mScope attachment also allowed us to study the transition from REM sleep to wakefulness, wherein we observed increased glutamate activity across the cortex (**Fig. 2.22**).

2.4 Discussion

We have introduced a neurotechnology for mesoscale activity mapping of the dorsal cortex in freely behaving mice. Among mammalian models used in neuroscience, mice have the widest range of transgenic animals for broad expression of genetically encoded calcium indicators

(Dana et al. 2014, 2019, Li et al. 2019), voltage indicators(Daigle et al. 2018) as well as reporters of neurotransmitters(Madisen et al. 2015). Combined with mouse models of neurodegenerative and neuropsychiatric disorders(Dawson et al. 2018), the mini-mScope should enable studies of mesoscale cortical activity mediating a range of complex behaviors in healthy mice and how these activities may be disrupted in diseased states.

The mini-mScope utilizes the CMOS sensor used in the open source “miniscope” (Cai et al. 2016). The miniscope platform is rapidly evolving, and sensors with increased sensitivity and imaging speed (Juneau et al. 2018), miniaturization, and wireless imaging capabilities (Barbera et al. 2019) are being developed. At a frame capture of 30 Hz, the LEDs were alternately pulsed with 20 ms pulses of the blue LEDs and 4 ms pulses of the green LED to maximize illumination intensity output while minimizing bleeding signal cross-over. An additional 2-minute LED warm-up period was allocated at the start of each test to eliminate non-linearities in LED illumination. While the current mini-mScope’s SNR is reduced when compared to the conventional epifluorescence macroscope, future versions could incorporate these improved sensors which are optimized for imaging dim voltage indicators (Juneau et al. 2018).

The mini-mScope performs reflectance measurements at green wavelengths to correct for hemodynamic effects. It is not possible to fully correct for hemodynamics with reflectance measurements using a single wavelength, and multiple wavelength reflectance measurements allow more accurate correction of hemodynamic effects (Ma et al. 2016, Valley et al. 2020), GCaMP6 signal is much brighter than the. In future versions, an additional red LED could be incorporated to obtain reflectance measurements at two wavelengths. Alternatively, issues with hemodynamic corrections could be addressed by illuminating GCaMP6f at its isosbestic point (Lerner et al. 2015). The mini-mScope architecture can also be adapted to image red-shifted fluorescent reporters.

Further, improvements could be made with the development of brighter indicators, such as GCaMP7, for transgenic mice, or with the use of red-shifted activity reporters, where such corrections are not necessary. Both improvements could be integrated via relatively simple changes to the optical filters.

The mini-mScope's FOV is currently limited to the dorsal cortex. Future mini-mScopes could be designed with an expanded FOV to encompass the cerebellar cortex or more lateral regions of the cortex. Finally, mini-mScopes could be designed to incorporate miniaturized amplifiers for integrating chronically implanted recording electrodes for simultaneous mesoscale imaging and deep brain neural recordings, or to interface with electrodes incorporated in the See-Shells for electrocorticography (ECoG)(Donaldson et al. 2019).

Chapter 3 Mesoscale imaging during spatial navigation

3.1 Significance

Successful navigation to a goal can be achieved by a number of behavioral strategies. Evidence suggests that mammals (including mice, rats, cats, dogs, monkeys, and humans) have access to multiple decision processes which are used at different times and which can be separated out with appropriately-defined behaviors (O'Keefe and Nadel 1978, Gallistel 1990, Redish 1999). The Barnes maze is a goal-finding task that rats and mice learn readily (Barnes 1979, Pitts 2018). In this task, mice are placed at the center of a well-lit environment and try to find an escape goal. Initially, mice will have to search randomly as they learn the basics of the task itself, but with experience, mice learn to go directly to the goal. Mice who know the task objective (find the escape hole) but who do not know the spatial location of the goal perform a serial search through many potential hiding holes(Harrison et al. 2006).

The incoming sensory information during spatial navigation is processed widely in the cortex, and information about space has been shown to be present in many cortical regions (Saleem et al. 2018, Esteves et al. 2021, Mika Diamanti et al. 2021). A number of cortical regions have neurons that reflect allocentric information (Mao et al. 2017, Krumin et al. 2018b, Alexander et al. 2020), while other regions have neurons that encode turns and other egocentric information (Mcnaughton et al. 1996, Nitz 2006b, Whitlock 2014, Wilber et al. 2014, Krumin et al. 2018b), and specifically retrosplenial cortex has been shown to encode both egocentric and allocentric information (Alexander and Nitz 2015). Neural activity in association areas of the cortex are also implicated in encoding landmarks (Czajkowski et al. 2014, Vedder et al. 2017, Fischer et al. 2020), route planning (Markus et al. 1995, Whitlock 2014, Krumin et al. 2018a) and associating allocentric cues with motor decisions (Franco and Goard 2021). It has also

been shown that interactions between brain regions are important for various cognitive and spatial navigation tasks (Rothschild et al. 2017, Negrón-Oyarzo et al. 2018, Abadchi et al. 2020, Fischer et al. 2020).

While the different navigation strategies have been shown to reflect different computational processes in individual cortical and subcortical regions (McDonald and White 1994, Geerts et al. 2020), it remains unknown how cortical signals are coordinated between different brain regions when these different strategies are being used for navigation. The measurably different strategies that mice show in the Barnes maze provide an opportunity to determine these cortical interaction changes that drive strategy changes.

We imaged calcium (Ca^{2+}) activity across most of the dorsal cortex of freely behaving mice while they solved the Barnes maze. We found that consistent with previous literature, mice rapidly and progressively used less time to reach the goal. Using a novel clustering algorithm, we decomposed the cortical dynamics into a low dimensional common state space, with each state corresponding to a pattern of cortical activation. We analyzed the temporal sequences of state activation and found distinct sequences of state transitions in the early part of the trial when mice made decisions about the direction to approach edge of the maze. These sequences of state transitions differentiated the behavioral strategies that mice used to solve the maze.

3.2 Methods

3.2.1 Animals

Surgery

Eight Thy-GCaMP6f mice were used in this study (Dana et al. 2014). All animal procedures were performed in accordance with the University of Minnesota's Institutional Animal Care and Use committee (IACUC). Mice were pre-emptively administered 1 mg/kg slow-

release Buprenorphine (Bupenorphine-SR, ZooPharm) and 1 mg/kg Meloxicam prior to surgery. Mice were then anesthetized using 1-4% isoflurane in pure oxygen prepared for surgery following standard aseptic procedures – the scalp was shaved and sterilized with repeated, alternate scrubbing with Betadine and 70% ethanol. The eyes were covered in sterile eye ointment (Puralube, Dechra Veterinary Products) to prevent drying. The mouse was affixed in a cranial microsurgery robot (Ghanbari et al. 2019b, Rynes et al. 2020) under 1-2% isoflurane. The surgical robot performed a large bilateral craniotomy spanning most of the motor, somatosensory, association, higher visual and visual cortices. The top edge of the craniotomy was always cut at 2 mm anterior to Bregma to facilitate alignment of the field of view to the Allen brain atlas (Dang et al. 2007). A transparent polymer skull(Ghanbari et al. 2019a) compatible with a miniaturized head mounted device (Rynes et al. 2021) was initially glued to the skull using surgical grade cyanoacrylate glue (Vetbond, 3M). Two bone screws were implanted in the parietal bone to further anchor the implant, prior to cementing with dental cement (Metabond, Parkell Inc). Mice were recovered from surgery on heating pad and returned to their home cage once they were full ambulatory.

Barnes Maze behavior

Mice recovered for at least 3 days after surgery. Mice were handled for 15-minute sessions over three successive days prior to experiments to acclimatize them to the experimenter. Dummy mini-mScopes with matched weights to the device used for trials were attached to the mice head to acclimatize them to the device weight during the handling sessions. An experimenter lowered the mice to the center of the maze at the beginning of each trial. Trials were split into three groups, habituation phase, acquisition phase, and probe phase, derived from canonical Barnes maze procedure (Barnes et al. 1979, Pitts et al 2018). During the habituation trail phase, animals were placed in a cylinder in the center of the maze and a

dummy mini-mScope was fitted to their implants. Non-goal holes were covered, revealing only the goal hole, and the mouse was allowed to explore the maze for 4 minutes. The maze was then rotated by 90º degrees for acquisition trials. During acquisition trial days, the mini-mscope was fitted onto mice for recording. Mice were placed in the start cylinder in low red-light conditions. Immediately when the trial began, white noise was played at 60 dB and a yellow overhead light was turned on. Non-goal holes were 1 cm deep with black silicone floors. Trials were terminated when the mouse entered the goal hole or after a 3-minute experiment time. For the probe trials, the maze was rotated so that the goal was in a different location with respect to the visual cues. Following all trials, the mouse was placed in the goal box for 1 minute, then returned to their home cage outside of the behavioral enclosure. In between trials, the maze was cleaned with 70% ethanol to reduce odor trails.

The Barnes maze was constructed from a 2.5. cm thick white, high-density polyethylene (HDPE) sheet. A 1-meter diameter circle was cut out of the HDPE sheet. Twenty 10 cm diameter holes were cut into the perimeter 5 cm from the edge of the sheet. A custom-made stair-case goal box was 3D printed using 1.75 mm diameter black PLA filament on a fused deposition modeling 3D printer (M2 3D printer, MakerGear). The maze was mounted onto an aluminum extrusion frame and anchored to a behavioral enclosure. The maze was 0.6 meters from the ground and at least 1.5 meters from any wall. The walls of the behavioral enclosure were made from 1/8-inch-thick single plywood sheets (Eucatile white tile board, Home Depot) and were coated with acoustic damping foam on the inner walls (JBER Acoustic Sound Foam Panels, Amazon) that covered the 1.8 m x 1.8 m x 2.4 m enclosure. A single behavior camera was mounted 1.2 m above the center of the arena to record behavior during the experiments (Blackfly S USB-3, FLIR). The mini-mScope electronics were routed through a low torque commutator (Carousel Commutator 1x DHST 2x LED, Plexon Inc).

3.2.2 Cortex-wide imaging using mini-mScope

Behavior imaging

One overhead camera was used to capture the entirety of the Barnes maze. The behavior camera was set to external trigger mode, line 3 trigger, any edge, (Spinview) and was synchronized to capture frames with the TTL pulses sent by the mini-mScope at each frame capture. The behavior camera exposure was set to 1000 µs and the resulting frames were compressed by 25% and saved to rapid access memory (128 GB RAM) as a .avi video file.

Calcium imaging

The original mini-mScope CMOS sensor (Rynes et al. 2021) was replaced with the MiniFAST CMOS sensor (Sony IMX290LLR-C CMOS sensor, Framos) for its increased sensitivity and smaller pixel size (Juneau et al. 2020). The MiniFAST sensor was set to acquire images at 30 frames per second (FPS), with alternate frames acquired with blue and green light illumination. Thus, images were acquired at 15 FPS under each illumination condition. The CMOS gain was set to a value of 55 and the LED voltage and current for the green LEDs was 5V 0.2A and 8V 0.8A for the blue LEDs. The blue and green LEDs on the mini-mScope were pulsed for 120 seconds, prior to the experiment to allow them to warm up and reach a stable intensity. The mice were brought into the Barnes maze under red light and placed into the opaque cylinder at the center of the maze ~90 s after the LEDs were turned on. The mini-mScope was attached to the mice via 3 interlocking magnets. At ~120 seconds, the white noise and yellow LEDs in the Barnes maze were switched on and the opaque cylinder was removed, marking the start of the trial. Trials typically lasted until mice went into the goal hole or at the end of 180 seconds.

Data pre-processing:

Behavior data pre-processing: For each trial, the location of each hole in the Barnes maze and the outer shape of the maze was automatically detected using computer vision scripts to define regions of interest (ROIs) within the Barnes maze. The location of the goal hole was marked to track where it was located as the Barnes maze was rotated across cohorts and probe days. The behavior camera data was aligned with the calcium imaging data via timestamps generated by the CMOS data acquisition board. , and any frame drops, or motion artifacts detected in the calcium imaging data were dropped in both the calcium imaging data and the behavior imaging data. The behavior camera data was also down sampled to match the calcium channel from the mini-mScope.

Calcium data pre-processing: To mitigate data saving, the MiniFAST software saves calcium imaging data in separate 1000 frame videos. The individual 1000 frame videos were combined into a single video using custom MATLAB scripts (2022b, MathWorks). K-means clustering was used to classify each frame of the video into the blue and green channels. Frames that were not classifiable into either the blue nor green channels due to large motion artifacts or irregularities in LED intensity (~0.04% of all frames) were marked for removal in future analysis. The videos corresponding to both illumination wavelengths were then passed through a motion correction algorithm (Dubbs et al. 2016).

The calcium data videos were compressed to 80% with a bilinear binning algorithm (2022b, MathWorks). One frame randomly selected in each trial was used to draw a mask around the imaged brain surface and exclude the background and superior saggital sinus artery to reduce noise in the overall DF/F signal. For each mouse, the masks across all trials were averaged to generate a mouse-specific average cortex mask. The average mask was imposed across images acquired in all trials for a mouse so that the number of pixels used in each analysis remained consistent.

Each pixel within the mask was corrected for global illumination fluctuations using a correction algorithm that produces DF/F data (Vanni and Murphy 2014). The DF/F data was filtered using a zero-order phase Chebyshev band-pass filter with cutoff frequencies of 0.1 Hz and 5 Hz (2022b, MathWorks). The resulting data was then spatially filtered with a 7-pixel nearest-neighbor average using a custom MATLAB script. The resulting DF/F time series for each pixel was then z-scored.

3.2.3 Data Analysis

Behavior

Data from the overhead behavior camera was analyzed using an unsupervised, marker-less tracking algorithm (Deeplabcut, (Mathis et al. 2018)). The program was trained to track the nose, the top of the head/mini-mScope, between the ears, the right and left forepaws, the shoulder blades, right and left hind paws, the lower back, the base of the tail, and the tip of the tail. This tracking data was used to determine where the mice were in the Barnes maze throughout the trial.

Cortical activation state identification using image correlation clustering

All calcium data was analyzed using custom scripts in Matlab (2022b, MathWorks). At each time point, a spatial map of DF/F z-score of every pixel within the common mask for a mouse was correlated with every other image captured at each time point using a Pearson's correlation coefficient to construct a correlation matrix. The correlation matrix was then sorted using k-means clustering with RNG defaults (for reproducibility) with 5000 iterations and 500 replicates (cross validation) to search for common, reoccurring activity patterns across time. A t-distance optimization algorithm was used to determine the optimal number of clusters to sort the correlation matrix, so that the correlations within each cluster were maximized and correlations

across clusters were minimized (Geerligs et al. 2021). The number clusters for which the largest cumulative t-distance value was obtained was selected as the number of clusters or states for each mouse (**Figure 3.1, Appendix A** for t-distance optimization plots for all mice).

All the frames within an identified cluster were averaged to generate a mean activity spatial map for each state. Image correlations between these mean activity maps for each state

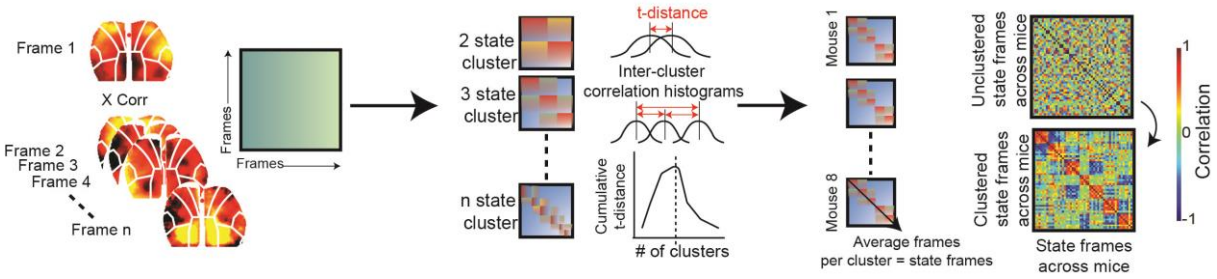

Figure 3.1: Methodology for identifying cortical activation states. a) *Left:* An image correlation matrix is constructed for all frames across all trials for each mouse. *Center:* A t-distance optimization algorithm is used to determine the optimal number of states to cluster the image correlation matrix into via k-means clustering for each mouse. Since the number of clusters (defined as states here) is unknown apriori, the t-distance optimization maximizes the correlation within each state while minimizing the correlation across states. The maximum t-distance value indicates the optimum state number for that mouse. *Right:* Mean DF/F activity maps for each state are constructed by averaging all the frames identified in that state for each mouse. A second image correlation matrix is formed by taking the correlation between the mean DF/F activity maps that exist for each optimized state in each mouse. The correlation matrix is sorted into 7 states of highly correlated average DF/F activity maps across mice, forming a common state model across mice.

identified for all mice were computed to construct a second correlation matrix, which was then sorted into 7 clusters via k-means clustering.

Frontal state activation

The time series of state activations for all trials were filtered using a sliding window to extract periods of high activation of state 1 and 2 (the frontal states) for all trials. The frontal state activation event was determined to be present if it persisted for a period greater than 1 second, with up to 4 frames of jitter into other states before returning to state 1 or state 2. After

the events were labeled, all state activation time series were aligned to the start and end of the frontal state activation event period for statistics and further analysis.

Head orientation angle

Two angles were defined for head orientation of the mouse during the start of the trial until the frontal state activation period. The allocentric angle, denoted as ω, was the angle between the instantaneous mouse body-head vector relative to fixed vector drawn from the center of the maze to the goal. The egocentric angle, denoted as φ, was the angle difference between the instantaneous mouse body-head vector and vector drawn from the instantaneous position of the mouse's body to the goal location.

Statistics

Wilcoxon rank sum non-parametric tests were used to determine statistical significance between serial and spatial search strategies state activation (**Figure 3e, Figure 4 h,l**). A Kruskal-Wallis test was used to determine statistical significance between head direction angles in the pre-FSA period. Non-parametric tests allow for unequal sample sizes between the search strategies. ANOVA tests were run with a Bonferroni correction to determine significance in state activation in the peri-event state probability histograms (**Figure 2g**). All error bars denote standard deviation.

3.3 Results

Mesoscale calcium imaging in mice learning a 2D spatial navigation task

We imaged calcium activity across large swathes of the dorsal cortex using a miniaturized head mounted camera (mini-mScope, (Rynes & Surinach et al. 2021)) in eight

freely behaving Thy1-GCaMP6f mice (Dana et al. 2014), as they solved the Barnes maze (**Fig. 3.2**). As mice learned the location of the goal, they exhibited expected results in the strategies used to search for the goal, which could be categorized as random, serial, or spatial search strategies (Pitts 2018) (**Fig. 3.3a**). As trials progressed, mice demonstrated a reduction in primary errors, or the number of incorrect holes checked prior to reaching the correct location of goal, and primary latency, or the initial trial time until the goal location is found (**Fig. 3.3b-c**).

Primary latency decreased from 51.0 ± 51.7(55.1 Interquartile range, IQR) s on day 1 acquisition trials to 17.6 ± 16.1s (11.0 IQR) on day 2, and 14.2 ± 14.4s (11.1 IQR) on day 3 (**Fig 3.3b,** Day 1 vs Day 2 p = 0.0006, Day 1 vs Day 3 p = 0.0001, Day 3 vs Probe p = 0.044,

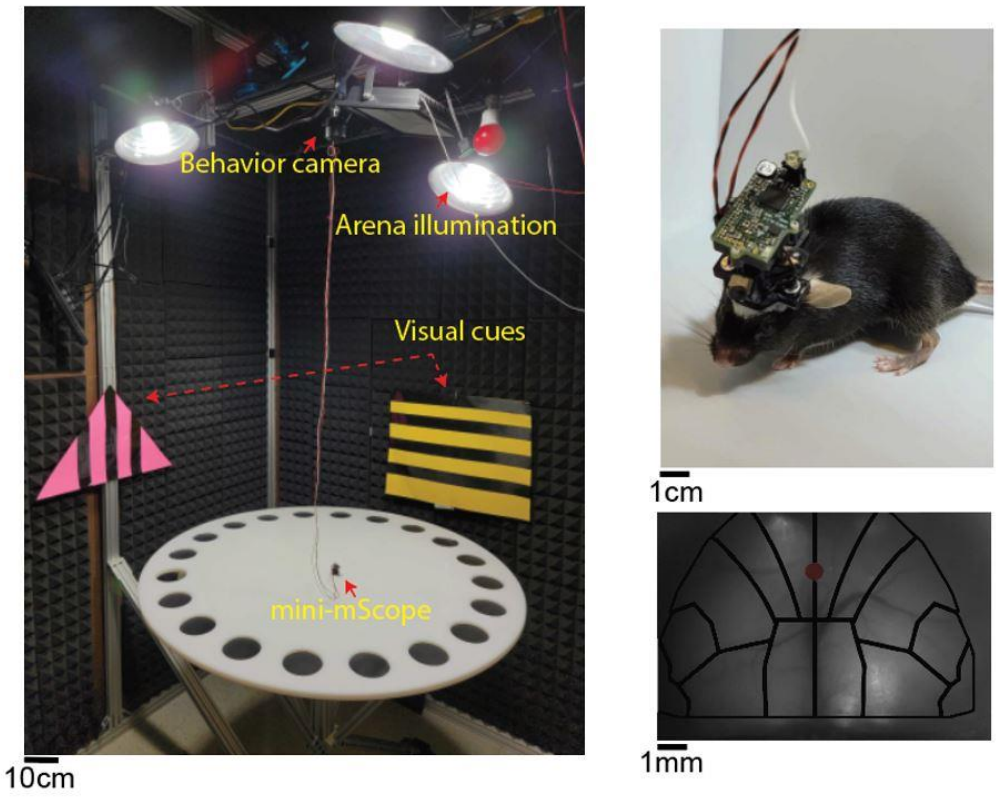

Figure 3.2: Mesoscale calcium imaging during spatial navigation. *Left:* Photograph of the behavioral setup including the mini-mScope and the Barnes Maze. *Right top*: Photo of a mouse bearing the mini-mScope in the behavioral arena. *Right bottom:* Photo of raw imaging field of view (FOV) through the mini-mScope with an Allen atlas overlaid. Red dot indicates bregma.

Wilcoxon ranked sum test). The primary latency increased to 26.0 ± 24.7(21.03 IQR) s when the goal location was moved on the probe trial, where the location of the goal was altered. Similarly, the number of primary errors decreased from 11.7 ± 9.2(11 IQR) on day 1, to 6.3 ± 6.1(7 IQR)

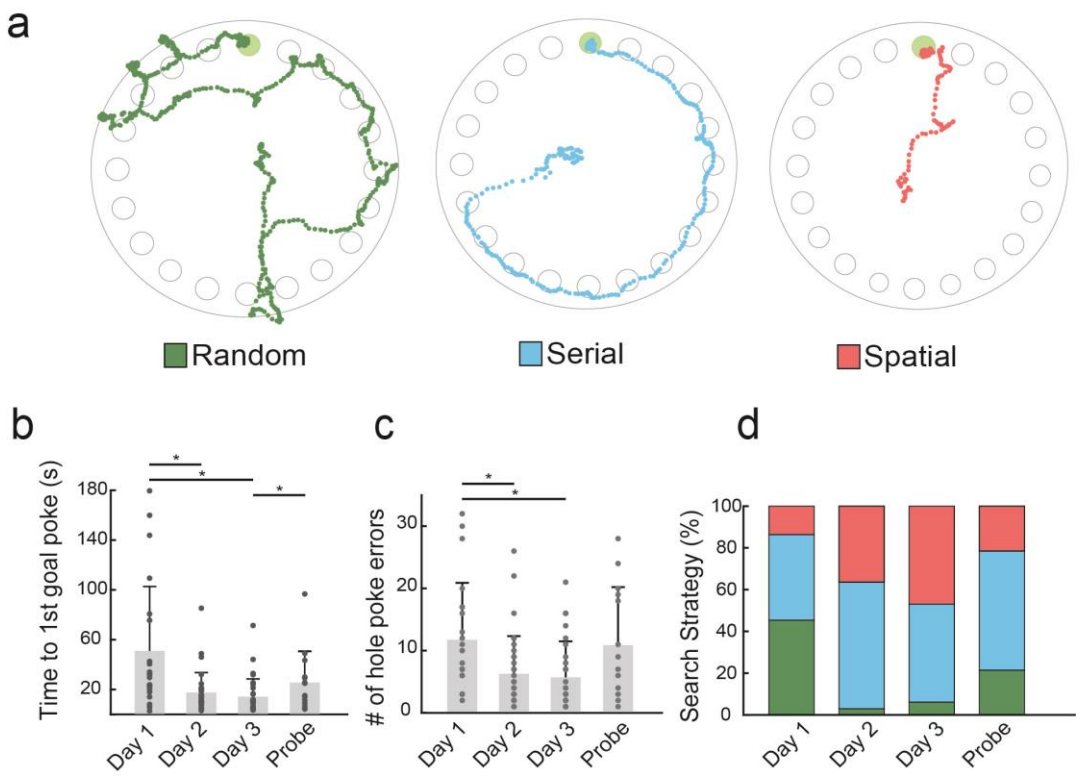

Figure 3.3: Barnes maze behavior during mesoscale imaging. a) Traces obtained from tracking data of mice which utilized random, serial, and spatial search methods as they learned to navigate the Barnes maze. **b)** Bar plot showing the mean primary latency, or time to first goal hole discovery, across days as mice learned to navigate the Barnes maze. Statistical significance from Wilcoxon ranked sum test are indicated with *. **c)** A bar plot showing the mean number of primary errors, or the number of times the mouse checked an incorrect hole before reaching the goal. Statistical significance from Wilcoxon ranked sum test are indicated with *. **d)** A bar plot showing the percentage of search strategies utilized across all trial days.

on day 2 and 5.7 ± 5.7(7.5 IQR) on day 3 across all mice, and the number of primary errors increased to 10.9 ± 9.2(16 IQR) when the goal location was changed in the probe trial (**Fig. 3.3c,** Day 1 vs Day 2 p = 0.012, Day 1 vs Day 3 p = 0,0001, Wilcoxon ranked sum test). These results are consistent with previous results obtained in this task (Markus et al. 1995), indicating mounting the mini-mScope did not interfere with previously-observed Barnes maze behaviors.

Across trials, mice utilized increasingly non-random search methods as they learned to navigate the maze. On day 1, 54.5% of trials were nonrandom, whereas 45.5% were random. On day 3, 93.7% of trials were non-random and 6.3% of trials were random. Mice increasingly utilized spatial searches as trials progressed where 13.6% of trials were spatial on day 1, 36.36% of trials were spatial on day 2, and 46.8% of trials were spatial on day 3 (**Fig 3.3d**).

While the white noise and bright lights were presented as mildly noxious stimuli and motivated the mice to navigate to the goal progressively faster, mice rarely entered the goal immediately after first poke (21% of trials, n=13/63 trials), preferring to explore the arena. In a subset of trials, mice explored the two nearest holes and the edge around the goal hole in 32% of trials (n=20/63), entering the goal hole 5-30 s after nearby exploration. A large subset of mice (46%, n=29/63) chose to repeat one or more searches around the maze after first goal poke before entering at some later trial time. Thus, while the animals were motivated to go to the goal, the environment was not excessively stress-inducing such that mice were not prevented from exploring the maze further.

Mesoscale cortical dynamics exhibited discrete shifts in cortical activation patterns

The mini-mScope imaged a field of view (FOV) of 8 mm x 11 mm, with a craniotomy encompassing 6 brain regions: primary motor cortex (M1), somatosensory cortex (SSC), premotor/frontal cortex (M2), retrosplenial cortex (RSC), primary visual cortex (V1), and barrel cortex (BC) on each hemisphere at a resolution of ~39-56 μm per pixel from the center to lateral edges of the FOV. As the mice navigated the maze, prolonged patterns of calcium activation across the FOV occurred sporadically, with observable shifts between these calcium activity patterns occurring at ~0.2-1 s time scales (**Fig. 3.4**).

We used an image correlation and clustering methodology to cluster spatial pattens of

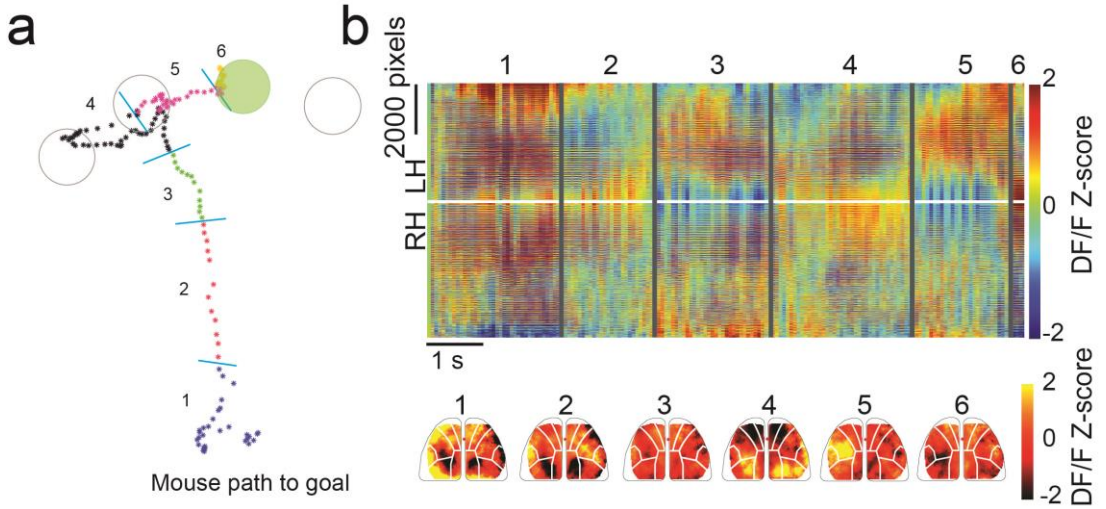

Figure 3.4: Episodes of sustained activity across the field of view observed during navigation. a) Tracking data from a spatial trial in which the mouse makes a single error on the way to the goal. The trace is annotated with periods that correspond to state-like shifts in calcium data across the cortex shown in **b**.**(b)** a map of the calcium data across the entire FOV acquired during the trial shown in the left panel. Numbered lines correspond to state-like global calcium activity transitions observed during the behavioral periods marked in the left panel. Pseudo color maps of the calcium DF/F Z-score from frames during each behavioral period are shown below. All error bars indicate sample standard deviation.

calcium activity observed in individual frames into groups of highly correlated images with similar patterns of cortical activation. We refer to these groups of highly correlated images as cortical activation 'states' (**Fig 3.4, Fig. 3.1a**). Briefly, the z-scored calcium DF/F activity recorded at each time frame was correlated with every frame recorded for a mouse across all trials, forming an image correlation matrix. The data in this matrix was then iteratively clustered into increasing numbers of states. The number of states needed to optimally cluster the cortical activity patterns is not known *a priori*. We used a t-distance optimization algorithm to determine the optimal number of states that could segregate the image correlation matrix into groups to maximize the correlations between images within a group while simultaneously minimizing the correlations between images across groups (Geerligs et al. 2021) (See **Methods** and **Fig. 3.1** for more details). We found that 5-10 states optimally described calcium activity clusters across

each mouse (**Fig 3.1b, Fig. 3.6**). An example of this clustering methodology for one mouse is shown in **Figure 3.4**.

To identify a common state space to describe activity in all mice, similar clustering

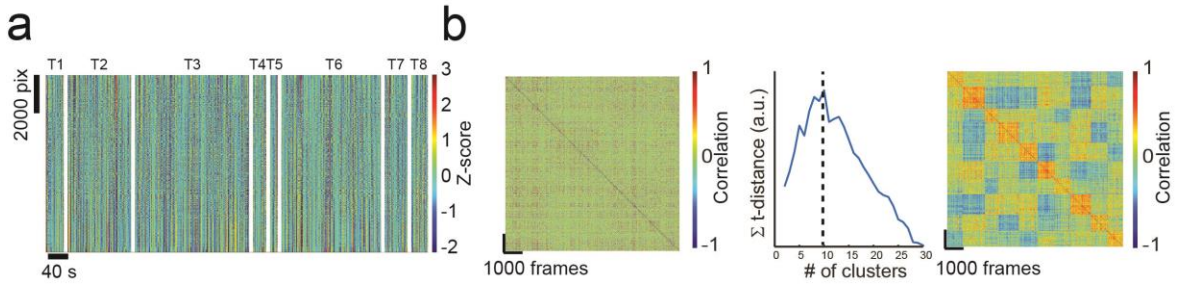

Figure 3.4: Example of state identification algorithm. a) Example of the method used to identify cortex-wide brain states from widefield calcium imaging during spatial navigation from one mouse. Data from all trials for one mouse is shown. All pixels across the FOV are plotted vs time. Trials are indicated by T1-T8 labels, separated by the white lines. **b)** *Left:* A correlation matrix is constructed by computing the image correlation between all frames. K-means clustering is used to organize the correlation matrix into highly correlated groups, denoted as states. *Center:* The number of states is determined by using an optimization algorithm which maximizes intra-cluster correlation while minimizing inter-cluster correlations. The maximum t-distance value indicates the optimal number of states for this mouse (k=10 states here). *Right:* the result of re-sorting the correlation map on the left into an optimized number of clusters determined with k-means clustering and t-distance optimization, resulting in 10 states for this mouse.

methodology was employed. Briefly, the average DF/F activity for each state identified per mouse was calculated by averaging activity across all frames within each state. The average frames for each state for all mice were then correlated to form a second image correlation matrix across all mice (51 x 51 matrix, **Fig. 3.1**). The image correlation matrix was then sorted into 7 states via k-means clustering to construct the intra-mouse state space model.

The spatial distribution of the mean calcium activity of all seven states for one mouse is shown in **Figure 3.5 top**. Additionally, a bar graph of the mean DF/F activity patterns for each ROI in the Allen brain atlas across all 7 states in each mouse (**Fig. 3.5, bottom)**. States 1 and 2 were characterized by high calcium activity in the frontal regions of the FOV. State 3 was characterized by high activity in several cortical areas of each hemisphere, with peak activation in bilateral somatosensory, primary motors, and antero-lateral retrospenial cortex. States 4 and

5 were characterized by high calcium activity in the posterior regions of the FOV. State 6 was characterized by high calcium activity in the vicinity of the midline. Lastly, state 7 was marked by activity distributed broadly across the left hemisphere. Observed mean activation patterns for states 1-6 were lateralized in most mice, perhaps indicating functional specialization between the cortical hemispheres during navigation.

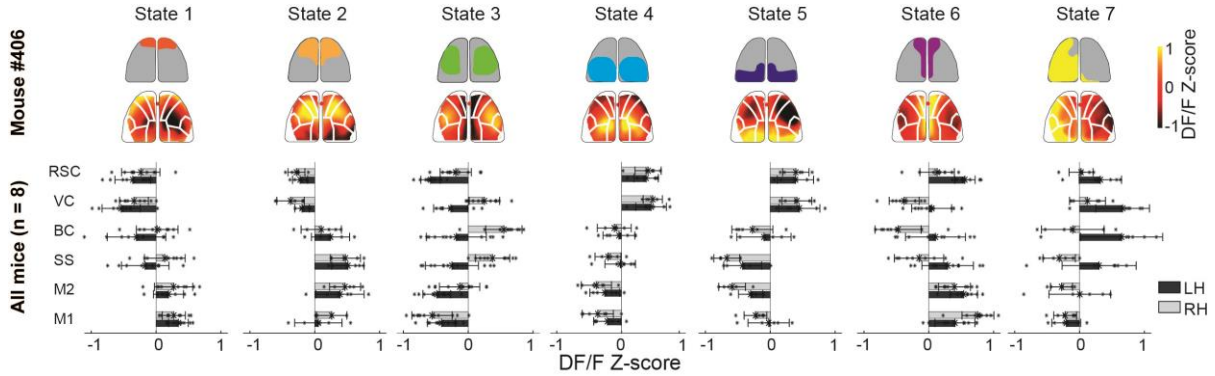

Figure 3.5: Analyzing cortical activation state space across mice. Common state space model across n = 8 mice and 63 trials. Optimum number of states varied from 5-10 states across all mice, with an average of 6.4 ± 2 states (**Fig. 3.1** and **Fig. 3.6**). 7 states were selected as sufficient to describe the state space across mice. States were identified by cortical areas across the FOV with high DF/F Z-score calcium signal. The top row illustrates simplified activity maps with high DF/F z-score activity. Below the top row are average DF/F Z-score heat maps for the mouse in **Fig. 3.4** which fit into the common state space. Bottom: bar graphs depicting the average DF/F Z-score of cortical regions across mice using the Allen atlas.

Every mouse had one of state 1 or 2 present, with n = 4 mice expressing both states. Additionally, every mouse had one of state 4 or 5 present, with n = 2 mice exhibiting both states. State 3 and 6 were present in all mice (n = 8), and state 7 was present in n = 5 mice (**Fig. 3.5, Fig. 3.6**). Example montages of DF/F Z-score activity for commonly occurring state transitions are shown in **Figures 3.7 and 3.8**.

The time series of detected states during the first 15 seconds of each trial is shown in **Figure 3.9a**, where rows denote trials for each search strategy, and colors signify the state that each frame in that trial was assigned. White spaces denote the trial has ended when the mouse enters the goal hole. Examples of the state activation along the path taken by a mouse during a

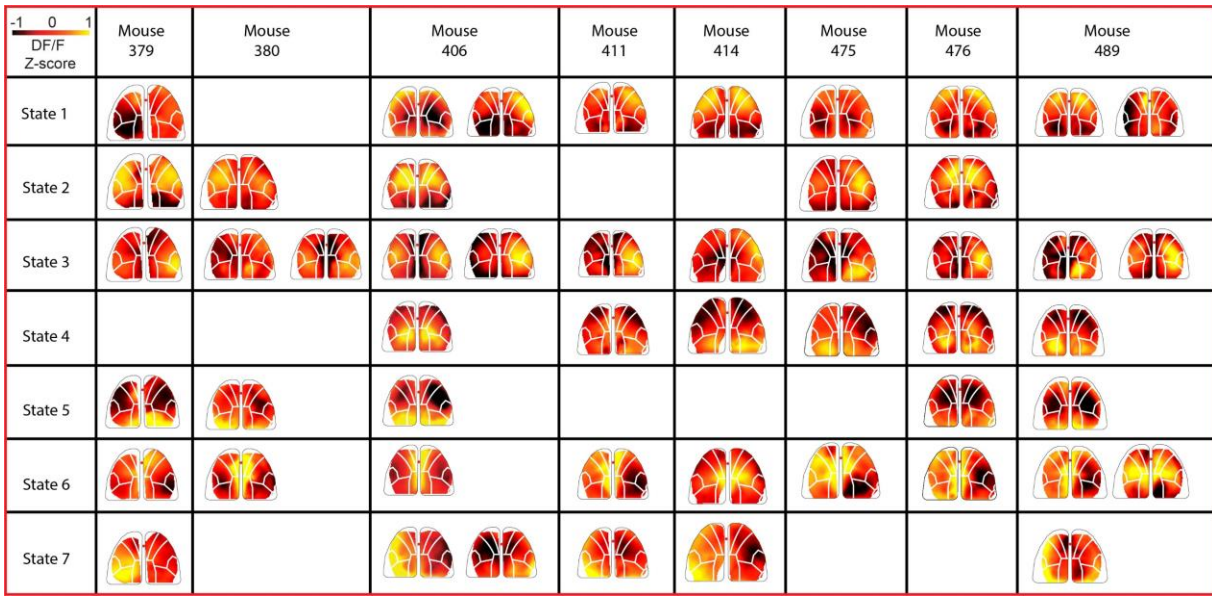

Figure 3.6: Common state space across mice. Mean DF/F z-score activity maps are formed for each mouse and state by averaging the DF/F activity across all frames identified within each state. The average maps are sorted into the common 7-state model and tabulated here (see **Fig. 3.1** for details).

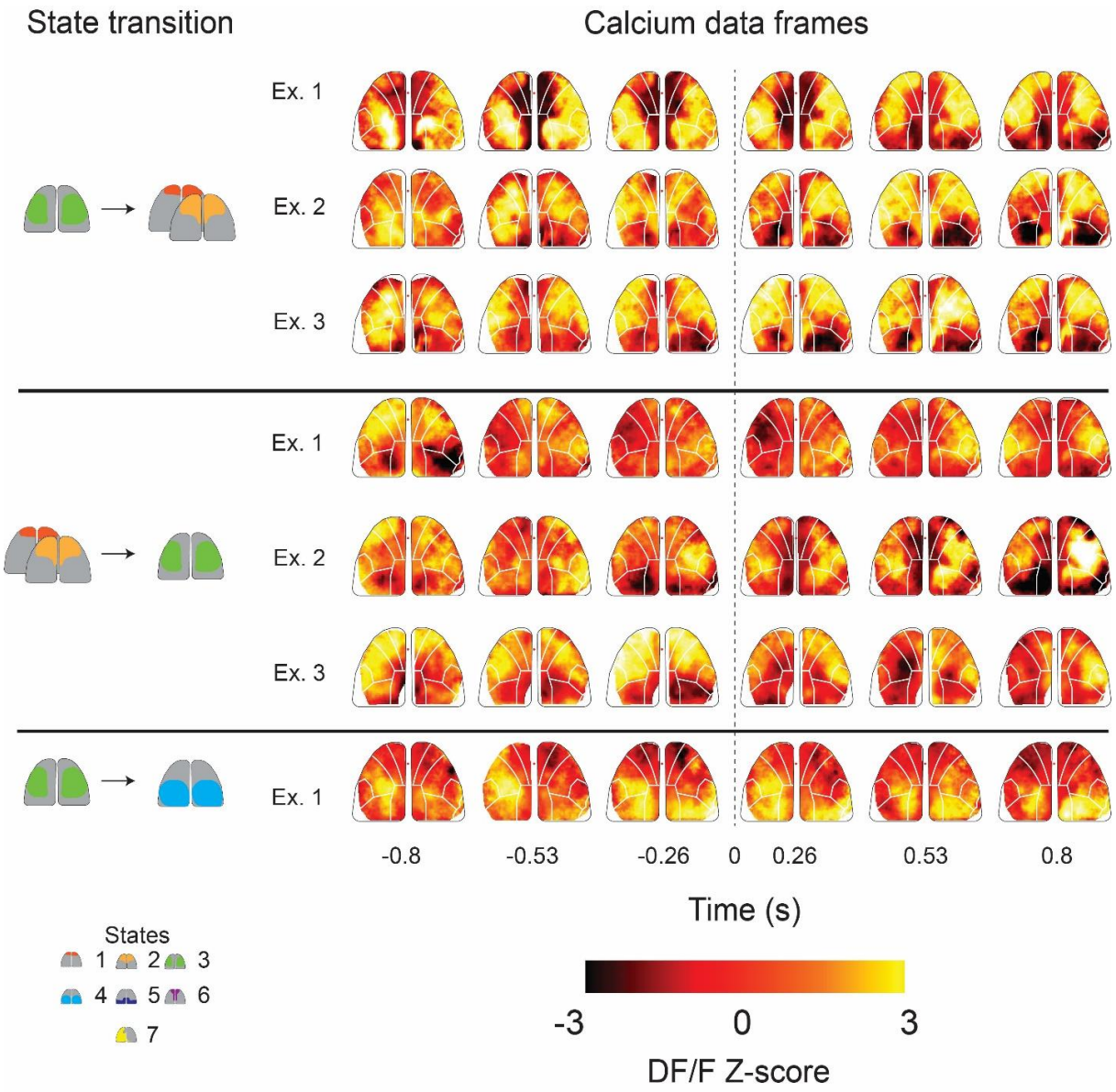

Figure 3.7: Montages of changes in calcium activity across the cortex during common state transitions. DF/F Z-score calcium activity maps illustrating examples of common state transitions to and from state 3. Simplified representations of the transitions are on the left, and DF/F Z-score maps are on the right, with each row representing a different example. Example transitions occur at t = 0. *Top:* three examples showing transitions from frontal states 1 and 2 to state 3. *Middle:* three examples showing transitions from state 3 to frontal states 1 and 2. *Bottom:* one example of a state 3 to state 4 transition.

random, serial, and spatial search trials are shown in **Figure 3.9e**. Similar visualization of state activation along the paths traversed by the mice in all trials are shown in **Appendix B**.

We evaluated the probability of a particular cortical activation state being active. For all states, mean state activation probability varied between 14.2% - 22.7% (**Fig. 3.7c-d**). States 3

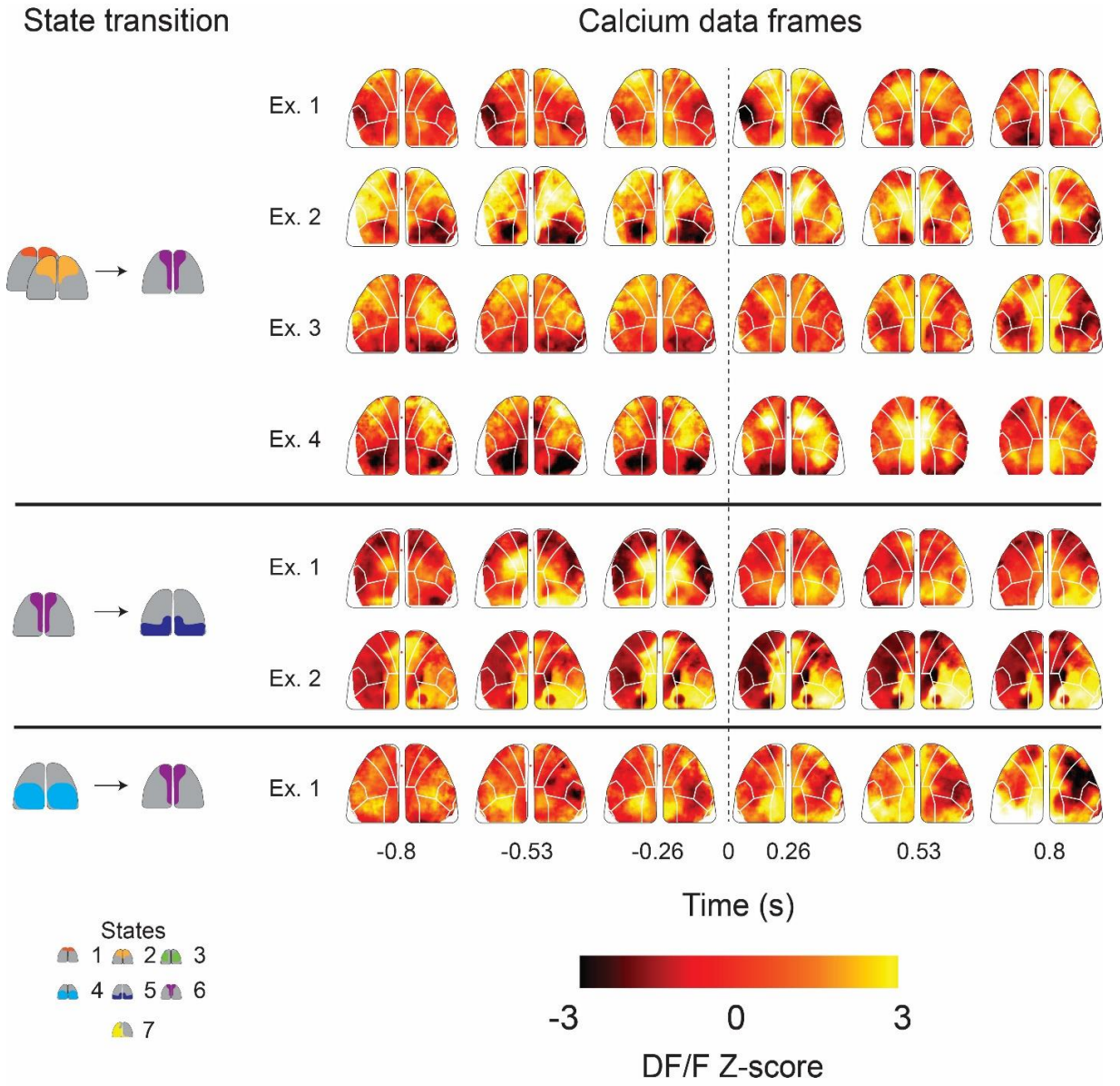

Figure 3.8: Montages of changes in calcium activity across the cortex during common state transitions. DF/F Z-score calcium activity maps illustrating examples of common state transitions to and from state 6. Simplified representations of the transitions are on the left, and DF/F Z-score maps are on the right, with each row representing a different example. Example transitions occur at t = 0. *Top:* four examples showing transitions from frontal states 1 and 2 to state 6. *Middle:* two examples showing state 6 transitioning to state 5. *Bottom:* one example of a state 4 to state 6 transition.

and 6 which are present in all the mice had slightly higher activation probabilities of 22.5 ± 9.2 %

and 18.8 ± 6.9% respectively. Thus, there was no one state having a dominant activation probability. Grouping trials by search strategy (**Fig. 3.10a**), we observed no significant differences in state activation probabilities for any of the states. The mean state activation probabilities did not change substantially as mice performed successive trials (**Fig. 3.10a right**).

We further examined how cortical activation changed from one state to the other by constructing state transition probabilities matrices for serial search trials and spatial search trials (**Fig. 3.10b**). Notably, state 3 had a high probability of 18.7% and 15.3% to transition to state 1 in random and serial trials, respectively. Transition probability from state 3 to state 1 in corresponding spatial trials decreased to 6.3% during spatial trials. State transition probabilities from state 5 were low (<6%) when transitioning to other states in trials on which mice used a random search strategy. In trials on which mice used a serial search strategy, state 5 transitioned to state 6 with a probability of 6.1%. In contrast, state 5 transitioned to state 3 and 7 with probabilities of 6.3% and 8.7% respectively during trials which mice used a spatial search

method. These results highlight how cortical dynamics were different for the trials with different behavioral strategies.

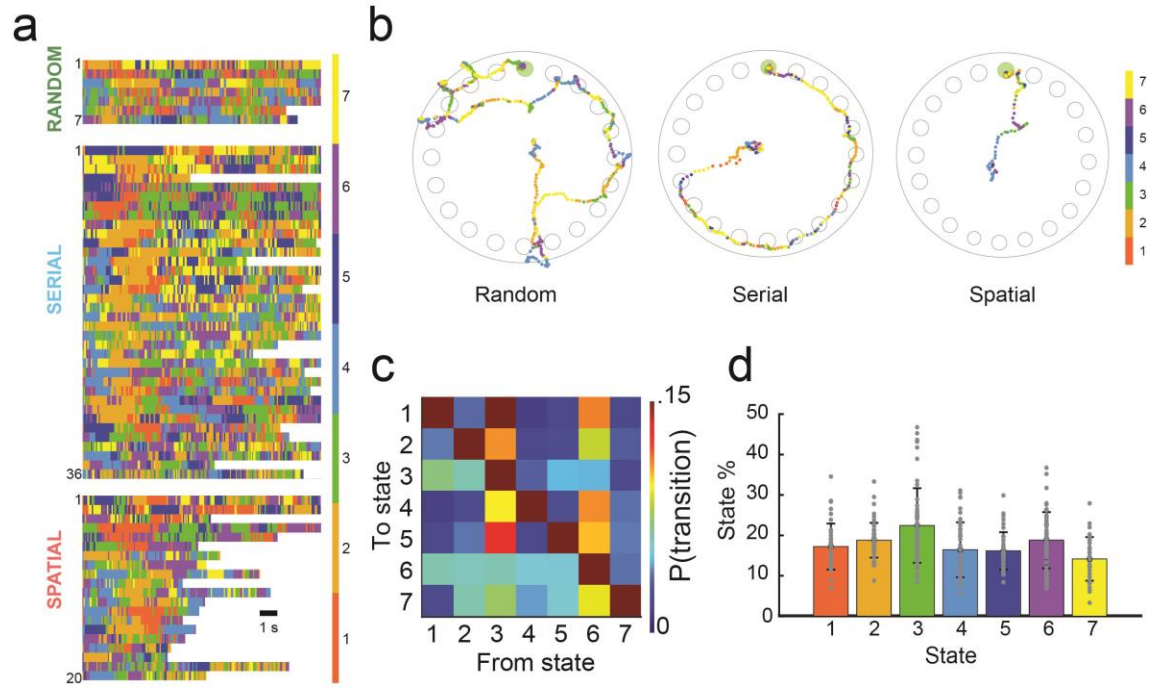

Figure 3.9: State space analysis of calcium data from mesoscale activity. a) Time series of state activation of the first 12 seconds of all trials plotted in a time series. Color bar indicates state number. The top row are random trials, the middle row are serial trials, and the bottom row are spatial trials. **b)** Examples path plots of random, serial, and spatial trials with state number overlayed on mouse tracking data. Color bar indicates state number. **c)** State transition probability matrix across all trials. **d)** Bar graph of the total state activation probabilities across all trials.

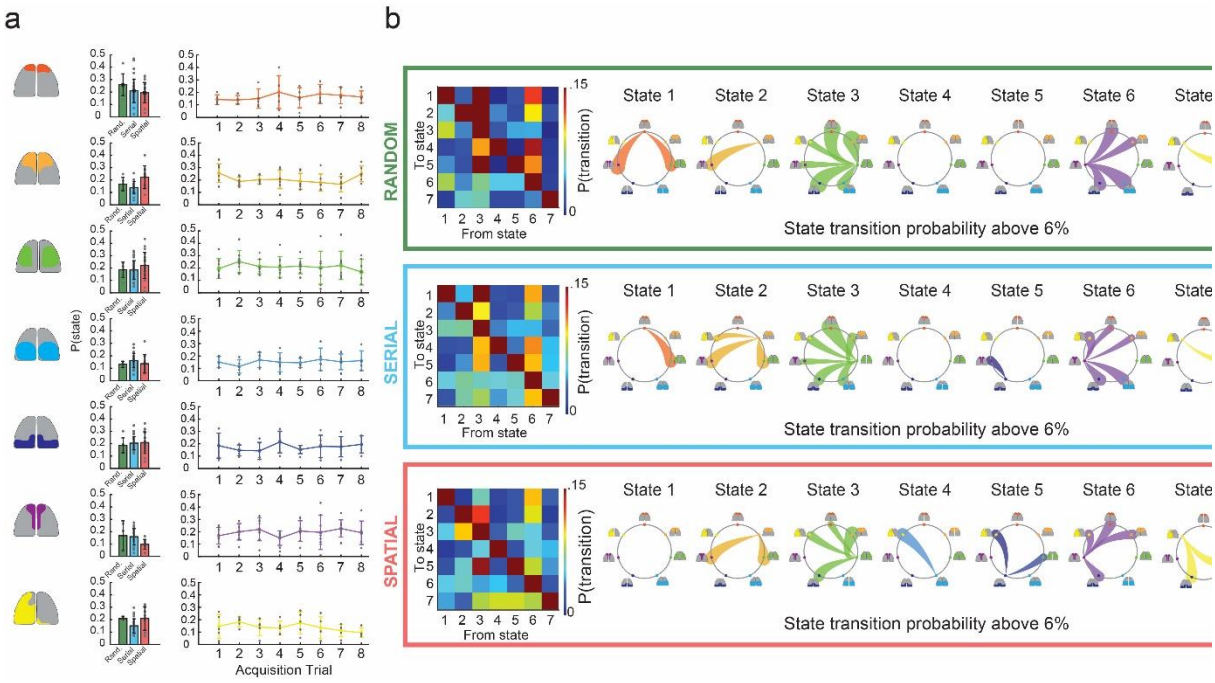

Figure 3.10: Brain-state variations across trials and search strategies. **a)** State activation probabilities across trials and search methods. *Left:* simplified schematic for each state. *Center*: state activation probabilities for trials groups by search method. Data points indicate each trial which mice utilized the search method. *Right:* state activation probabilities across trials for all mice. Data points indicate state activation probabilities for each mouse. All error bars indicate standard deviation. **b)** State transition probability matrices for random (top), serial (middle), and spatial (bottom) trials. State transition node maps indicate specific state transition probabilities above 6% for each search method. Thickness of the lines indicate higher state transition probabilities.

Frontal regions of the cortex are activated for prolonged durations shortly after trial initiation

Representing the patterns of cortical activation in a low-dimensional state space allowed us to examine trial-by-trial variation in cortical dynamics during the spatial navigation task. We observed repeated temporal sequences of state activation that occurred shortly after trial initiation. Trials typically started with a variegated sequence of states, but then transitioned to a clear and prolonged period of activation of the one or both frontal cortex active states (states 1 or 2) near the start of the trial (**Fig. 3.7a**). These prolonged durations of frontal cortex states

(henceforth referred to as frontal state activation event or FSA event) could be algorithmically identified as conditions where state 1 or 2 was active for more than 1 second near the start of the trial (**Fig. 3.11**). The FSA events occurred in 57.1% of trials where mice used random search method, 91.7% of trials which the mouse used a serial search method, and 85.0% of trials where the mouse used a spatial search method (**Fig. 3.12a**). These FSA periods were primarily associated with non-random search strategy trials. Overall, mean onset to the FSA event was 2.3 ± 1.9 s. In trials in which mice performed a random search strategy, the mean onset to the FSA event was 1.4 ± 1.2 s, whereas in serial search trials it was 2.3 ± 2.0 s, and 2.5 ± 2.0 s in spatial search strategy trials (**Fig. 3.12b**). The mean duration of the FSA event was 2.0 ± 0.7 s. The duration of the FSA event at the beginning of trials were also longer in serial search and spatial than in random strategy trials. In trials on which the mice performed a random strategy, the mean duration of the FSA event was 1.5 ± 0.4 s, whereas it was 2.0 ± 0.6 s in serial trials, and 2.2 ± 1.0 s in spatial trials (**Fig. 3.12c**).

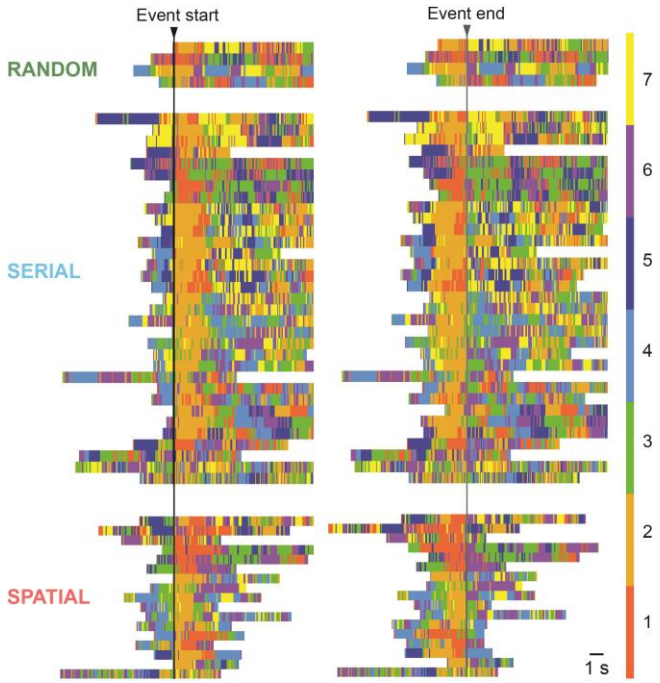

Figure 3.11: Prolonged activation of frontal states at trial start. Time series of state activation of all trials containing >1 second activation of frontal states 1 or 2 aligned to the start of the frontal state activation event (FSA event, left) and the end of the FSA event (right)

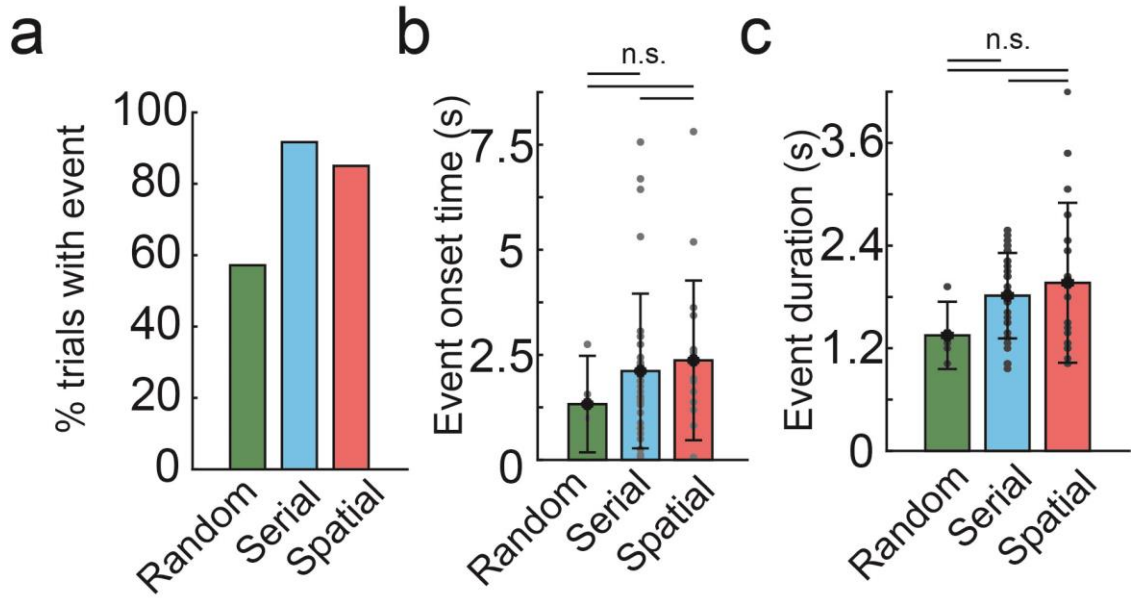

Figure 3.12: Frontal state activation events across search strategies. a) A bar graph depicting the total percentage of trials in which FSA event occurred when mice used random, serial and spatial search strategies. **b)** A bar graph depicting the mean onset time to the FSA event for trials which the mouse utilized each search strategy. **c)** A bar graph depicting the total duration of the of the FSA event for trials which the mouse utilized each search strategy.

Frontal state activation events coincided with approach to edge of the maze

We next evaluated the behavior of the mice around the FSA events in serial and spatial search trials by examining the position, velocity, and head direction of the mice (**Fig. 3.13**). Plots of the location of the mice during the FSA event indicated that the FSA event occurred when mice approached the edge of the maze from the initial starting location at the center of the maze (**Fig. 3.13a**). In 84.4% of trials with a FSA event, the event initiated before or during the mouse's approach to the edge of the arena. The FSA event began during the initial period of the trial before the mouse approached the edge and as it investigated its surroundings. The FSA events occurred before the mouse reached the edge of the maze in 60.6% of trials with an FSA event for serial trials vs 35.3% of trials for spatial search strategies with an FSA event. The FSA events were also accompanied by an increase in velocity of the animal, with instantaneous velocity peaking ~800ms after event onset in both serial (mean peak velocity of 25.5 cm/s, **Fig.**

3.13b top left and **Fig. 3.13c left**) and spatial trials (mean peak velocity of 27.1 cm/s, **Fig. 3.13b bottom left** and **Fig. 3.13c left**). The end of the FSA event coincided with a decrease in velocity in both serial and spatial trials, with a steeper decline in velocity in spatial trials starting 50 ms prior to the end of the event as mice approached the vicinity of the goal (**Fig. 3.13b right** and **Fig. 3.13c right**).

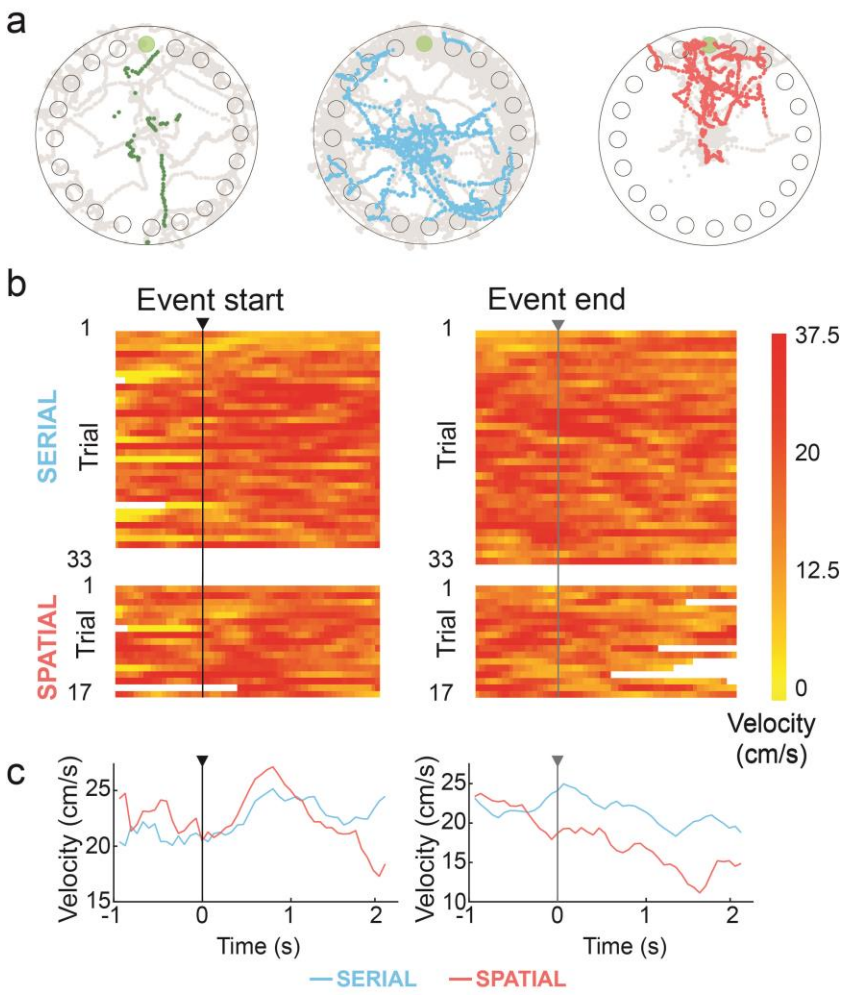

Figure 3.13: Frontal state activation events occur during approach to edge. a) Mouse tracking data from trials in which the mouse utilized random, serial, and spatial search strategies. Colored points indicate the frontal state activation period and gray points indicate the rest of the tracking data to first goal poke. **b)** Plots depicting the velocity of mice in trials with a FSA event. The FSA event period is aligned to the start and end of the event for serial and spatial trials. **c)** Average velocity plots made from **f** with serial and spatial trials superimposed before and after the frontal state activation event.

Head orientation towards goal was initiated prior to frontal activation state events in spatial trials

The period before the FSA event is likely a self-localization event in which mice survey the space before deciding on direction of approach to the edge of the mice. We examined the changes in both the allocentric heading direction (ω), and the egocentric heading direction (φ) of the mice in the time before the FSA event (**Fig. 3.14, Fig. 3.15**). When mice employed spatial search strategies, mice oriented towards the goal quadrant ($|\omega| < 45°$) 500 ms prior to event onset on 41% of trials (7/17) (**Fig. 3.15a bottom left**). They continued to orient towards the goal until the start of the FSA event. At the event onset, mice were oriented in the direction of goal quadrant on 59% of trials (10/17 trials), with an increased fraction (76.4%, 13/17 trials) 500 ms after event onset. Mean allocentric heading orientation reduced from 73.9° 500 ms prior to event onset to 46.4° 1s after event onset (**Fig. 3.15b left**). In contrast, mice were oriented towards the goal quadrant in the allocentric reference frame in only 27% of serial trials (9/33) at the event onset, with no decline in heading direction angle observed after event onset (**Fig. 3.15a top left**). Mean allocentric heading direction for serials trials 500 ms prior to event onset was 94.3°and 97.1° degrees 1 s after event onset (**Fig. 3.15b left**).

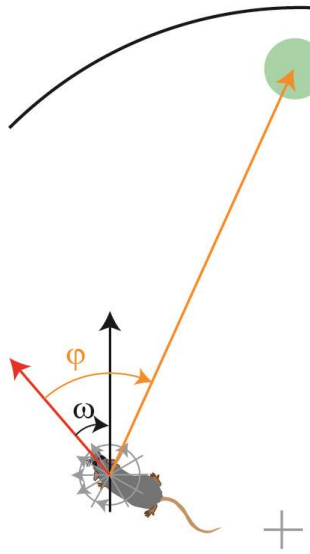

Figure 3.14: Schematic of allocentric and egocentric head angles, ω and φ.

Similar differences in trends between serial and spatial trials were observed in φ near the start of the trial before the FSA event (**Fig. 3.15c-d**). When mice employed spatial search strategies, 47% of trials (8/17) had mice oriented towards the goal quadrant ($|\varphi| < 45°$) 500 ms

prior to event onset (**Fig. 3.15c bottom left**) and continued to do so until event start. At the event onset, mice oriented in the direction of goal quadrant on 65% of trials (11/17 trials), with

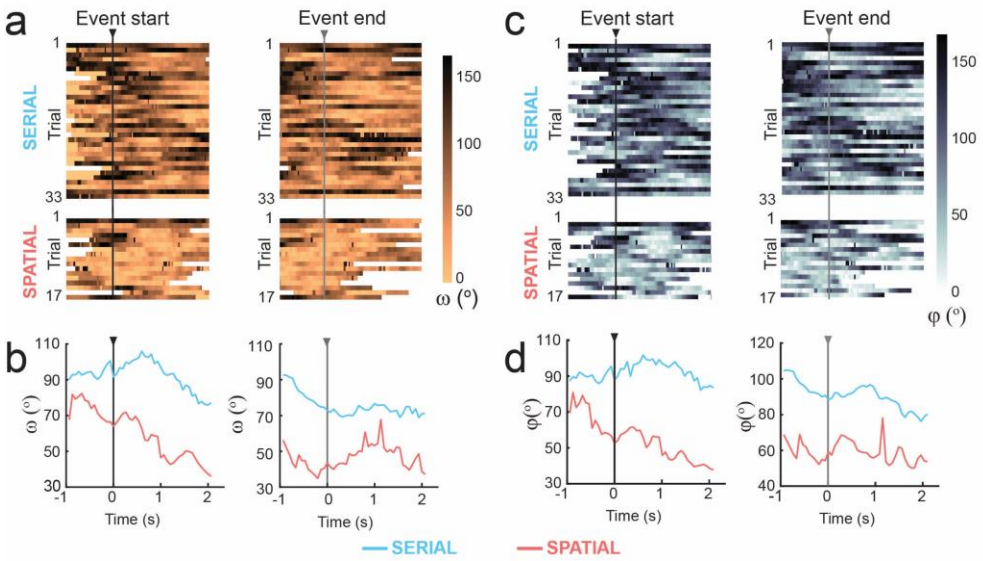

Figure 3.15: Orientation to the goal happens in spatial trials before the FSA event. a) Allocentric head direction plots of trials with the frontal state activation period aligned to the start and end of the event for serial and spatial trials. **b)** Average allocentric head direction plots made from **a** with serial and spatial trials superimposed before and after the frontal state activation event. **c)** Egocentric head direction plots of trials with the frontal state activation period aligned to the start and end of the event for serial and spatial trials. **d)** Average egocentric head direction plots made from **c** with serial and spatial trials superimposed before and after the frontal state activation event.

an increased fraction (18%, 3/17 trials) 500 ms after event onset. Mean egocentric heading orientation reduced from 84.6° 500 ms prior to event onset to 55.9° 1s after event onset (**Fig. 3.15d left**). In contrast, mice were oriented towards the goal quadrant in the allocentric reference frame in 24% of serial trials (8/33) at the event onset, with no decline in egocentric heading direction angle observed after event onset (**Fig. 3.15c top left**). Mean egocentric heading direction for serials trials 500 ms prior to event onset was 99.7° and 107° 1 s after event onset (**Fig. 3.15d left**).

Sequences of state transitions before activation of the frontal cortex were search strategy dependent

We next evaluated if there were differences in sequences of state activation during specific periods around the FSA events. Examining state activation probabilities in the duration of time prior to the FSA event period revealed differences between serial and spatial search methods (**Fig. 3.16**). In trials where mice utilized serial searches, state 7 had an activation probability of 29.3 ± 29.2% prior to FSA event. In spatial trials, the activation probability reduced to 14.1 ± 5.4%. State 3 had an activation probability of 28.7 ± 26.9% prior to the FSA event in spatial search trials, significantly higher than the activation probability in serial search trials (12.4 ± 19.6%, p = 0.007, Wilcoxon ranked sum test, **Fig. 3.16a**). State 6 activation probability did not change notably between the two search strategies (16.5 ± 17.4% serial search trials, 11.9 ± 13.6% spatial search trials). Examining state transition probabilities in the period before the FSA

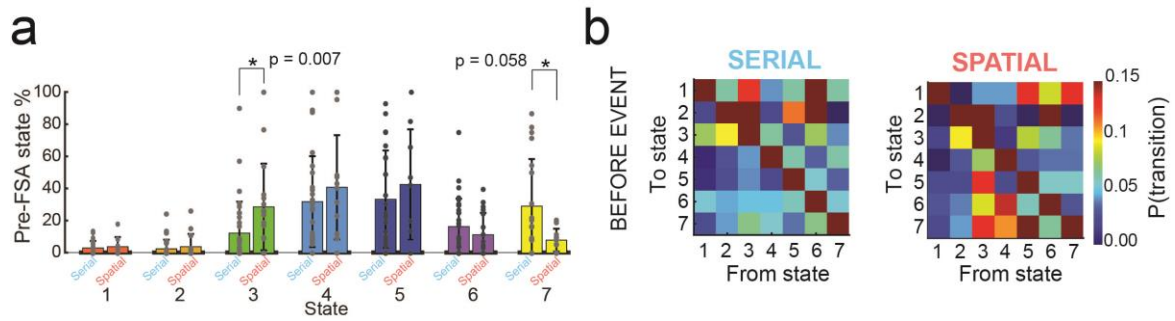

Figure 3.16: State activation percentage and transition probability before FSA event. **(a)** Bar plots of states activation probabilities for all states before the FSA event in serial and spatial trials. Statistically significant differences are highlighted (Wilcoxon rank sum test). **(b)** State transition probabilities before the FSA event for serial and spatial trials.

event revealed differences in dynamics of cortical activity between spatial and serial trials **(Fig. 3.16b)**. Most prominently, state 3 had a high probability of transitioning to many states in spatial trials, but not in serial trials.

To quantify the patterns of state transitions leading up to the FSA, we constructed peri-event state probability histograms (**Fig. 3.17**). As a control, we generated randomized data by performing 100 bootstraps of the time series of states for each trial. We determined if a state's activation probability was statistically significant from the bootstrapped trials by using an Anova

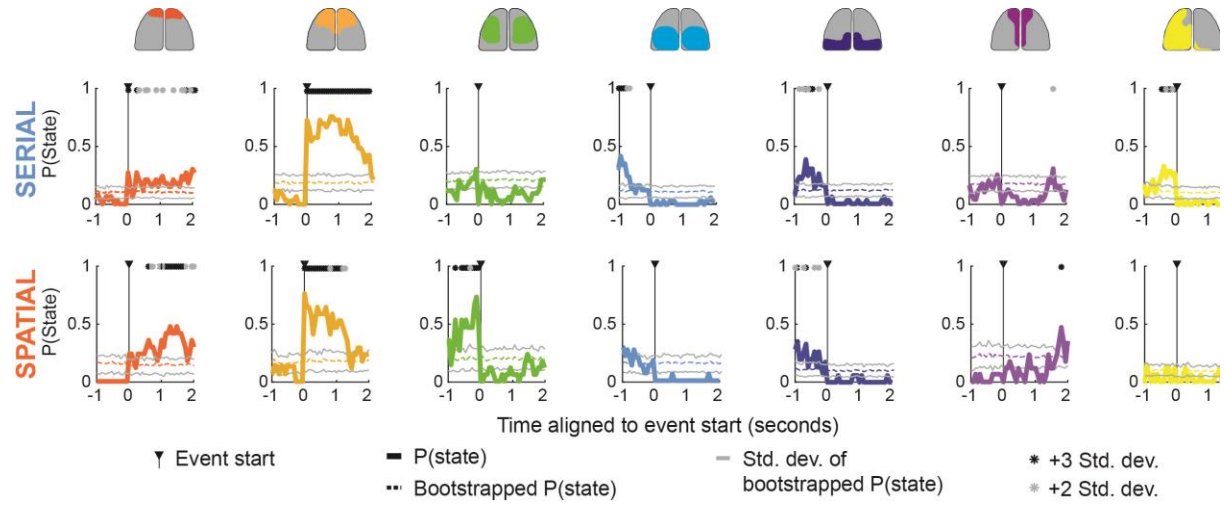

Figure 3.17: Sequences of states before FSA event depend on search method. Peri-event state probability histograms aligned to the start of the frontal state activation event in serial and spatial trials. Solid color lines denote the average peri-event probability across all trials. Transparent solid color lines indicate the average of 100 randomized bootstrapped trials with standard deviation lines in gray. Asterisks indicate statistical significance against bootstrapped data using an Anova test with a Bonferroni correction (gray $p<0.05$; black $p<0.01$).

test with a Bonferroni correction of the mean state activation probability aligned to the FSA period to the bootstrapped data. In serial trails, the 1 s period leading up to the FSA event was marked by significantly higher activation of state 4, followed state 5 and then by state 7 when compared bootstrapped mean. In contrast, in spatial trials, the same 1 s period was marked by activation of state 5 that was followed by activation of state 3 before entering the FSA period (**Fig. 3.18a**). These results indicate that the sequences of state transitions occurring before the FSA events were search strategy dependent (**Fig. 3.18b**).

State 3 was preferentially active before FSA during goal-heading direction in spatial but not serial trials

When considering the entire duration before the FSA event, heading direction in the allocentric reference frame was significantly more aligned towards the goal in spatial search trials (77.1° ± 50.4°) as compared to serial search trials (94.9° ± 52.7°, $p<0.001$, Kruskal-Wallis

test). Similarly, evaluating the egocentric heading direction revealed there was significantly more alignment towards the goal in spatial search trials (88.1° ± 50.3°) as compared to serial search trials (101.8° ± 51°, p<0.001, Kruskal-Wallis test). Thus, there was an overall change in

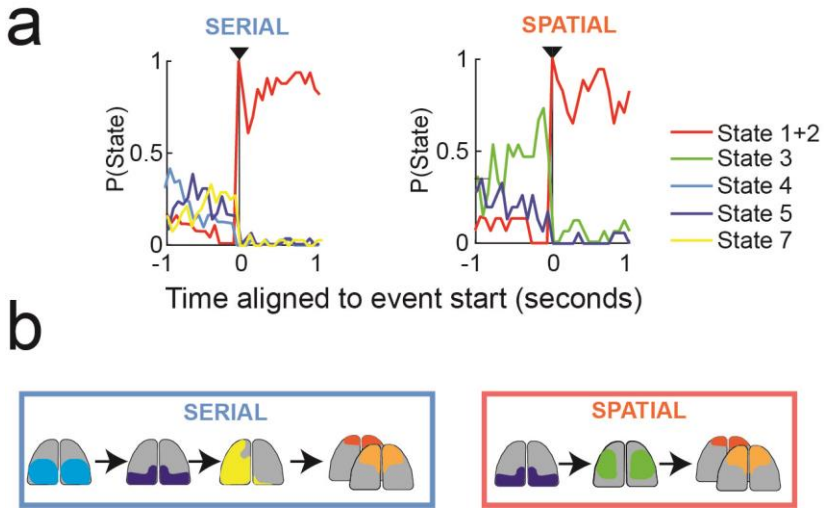

Figure 3.18: Summary of state sequences before frontal state activation dependent upon search method. a) Summary of statistically significant probability of state activation in **Figure 3.17**. **b)** Simplified state transition schematic of cortical activation states 1 s before and during the FSA event using the statistically significant state activation periods found in **Figure 3.15** for serial and spatial trials.

tuning of heading direction for most states that differed between serial and spatial trials.

We next asked if the animals head orientation affected the activation of states. We examined the times when head direction of the mice was aligned to the goal quadrant in the allocentric reference frame ($|\omega| < 45°$, **Fig. 3.19a**) and egocentric reference frame ($|\varphi| < 45°$, **Fig. 3.19b**). Within these events we asked what the likelihood of a certain state being active was prior to the FSA event. State 3, which was significantly more likely to be active immediately prior to FSA event onset in spatial trials (**Fig. 3.17a, Fig. 3.18**), was much more likely to be active when animals were oriented towards the goal quadrant in the allocentric frame of reference during spatial trials), as compared to serial trials (mean P(s3) spatial = 0.33, mean P(s3) serial = 0.13, p = 0.046, Wilcoxon Rank-sum test). For egocentric goal orientation, state 3 also had a higher probability of being active while mice were oriented to the goal as well (mean

P(s3) spatial = 0.31, mean P(s3) serial = 0.07, p = 0.021). No significant differences were found for any of the other states. These results indicate that state 3 was preferentially activated when the animals head direction was oriented towards the goal in spatial trials, but not in serial trials.

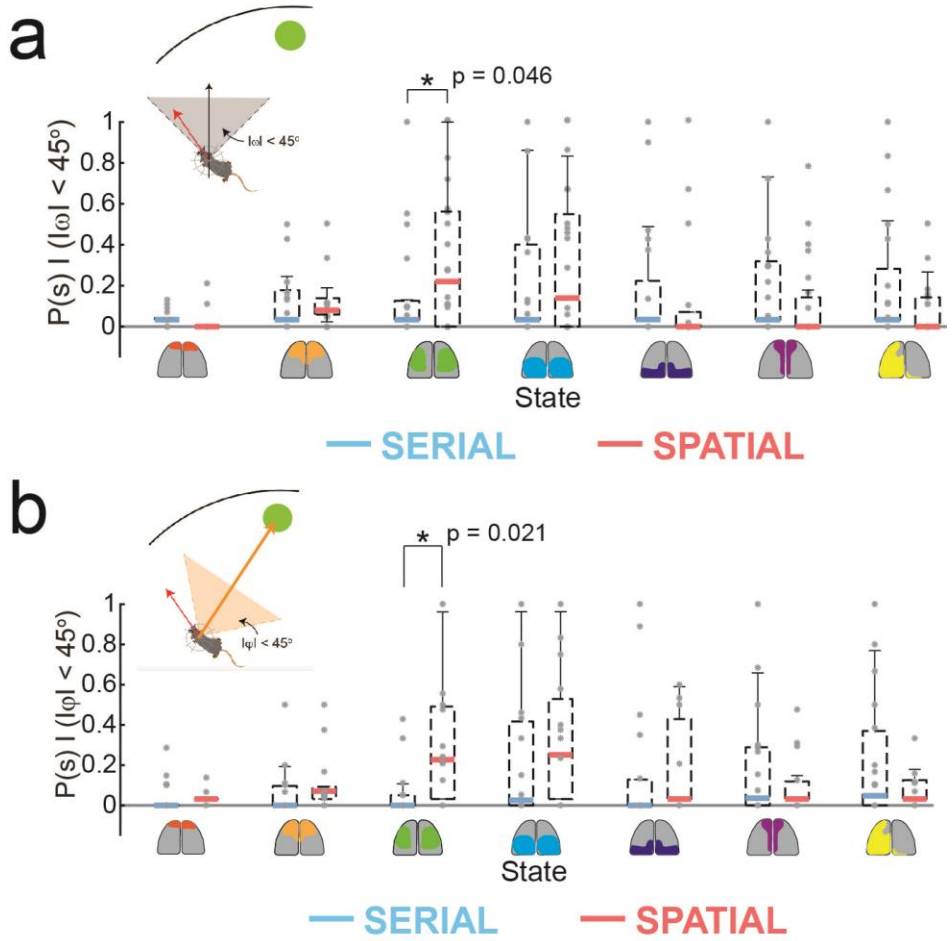

Figure 3.19: State 3 is preferentially active while mice orient to the goal while spatial strategies are used, but not serial strategies. a) State activation probability box plots generated for allocentric head direction for |ω|<45 degrees for serial vs spatial trials. **b)** State activation probability plots generated for egocentric head direction for |φ}<45 degrees for serial vs spatial trials. Statistically significant comparisons are highlighted (Wilcoxon rank sum test).

Thus, activation of state 3 in spatial trials may indicate a recognition of the goal direction in spatial trials when mice make direct approaches to the goal.

Chapter 4 Conclusion

Traditionally, mesoscale cortical imaging has been done exclusively in head fixed animals. Studying brief, stereotyped behaviors during head fixation has revealed much about cortex wide calcium dynamics during locomotion (Musall et al. 2019, Mitelut et al. 2022, West et al. 2022), motor learning (Allen et al. 2017a, Makino et al. 2017), sensory discrimination (Gilad and Helmchen 2020), decision making (Orsolic et al. 2019, Pinto et al. 2019) and goal directed behavior (Allen et al. 2017b), The cortical dynamics are also altered in diseased states (Sepers et al. 2022, Cramer et al. 2023). To our knowledge, this is the first attempt to observe cortex wide calcium dynamics in freely moving mice performing an ethologically relevant spatial navigation task, where learning progresses rapidly. The behavioral variability posed a challenge as no two trials were similar. Our data-driven modeling approach used here allowed us to capture trial to trial variability in cortical activation patterns in a low dimensional state space, enabling the correlation of brain states to behavior.

We discovered coordinated sequences of brain-wide activity patterns reflected in mesoscale cortical activity on a spatial navigation task that differentiated goal-oriented and non-goal-oriented strategies. The clustering algorithm we developed in this study identified 7 cortical activation states that were generalizable across mice and trials, and 15 state transitions that occurred frequently during this spatial navigation task. Similar numbers of dynamic motifs have been independently described in studies looking at mesoscale calcium dynamics during head-fixed spontaneous behaviors (MacDowell and Buschman 2020), with distinct dynamics observed during memory guided and sensory guided tasks (Pinto et al. 2019b), and uninstructed movements during sensory decision making (Musall et al. 2019b) and locomotion

(West et al. 2022). These findings suggest that such generalizable repeated sequences of activity may underlie a diverse set of behaviors.

Trial initiation was marked by an initial duration lasting 1-2 seconds of variegated sequences of states while animals were in the center of the maze near the starting location, followed by prolonged activation of states associated with activation of frontal areas of the cortex lasting 1-2 seconds (FSA event) as the animals turned towards the edge of the maze. Despite the variability in the behavior, with the path taken by the mice to goal distinct in each trial, the FSA event occurred reliably in most serial and spatial search strategy trials and coincided with the phase of spatial navigation where mice approached the edge of the maze from the central starting point.

Additionally, the sequence of state changes preceding and succeeding the frontal activation event were distinct for goal and non-goal oriented (spatial and serial) search strategies. In spatial (goal-oriented) trials, the 1s period prior to the frontal activation event (FSA) was marked by a transition from activation of posterior regions of the cortex to broad activation of the lateral regions of the cortex, anterior to the primary visual areas (State 3). In serial (non-goal-oriented) trials, this 1s period was marked by a sequential progression of states associated with high level bilateral activation of posterior regions of the cortex along with the RSC (States 4 and 5), followed by broad activation of left hemisphere (State 7). These distinct sequences of state transitions are summarized in **Figure 3.18b**. This points to different brain wide circuits being recruited at different time points during the task. Further, these data suggest a frontal role in moving towards the edge and suggests differences in information processing between spatial and serial strategies, both of which successfully get the mouse to the goal.

Goal-oriented spatial navigation depends on cognitive maps (Tolman 1948), dependent on structures such as the hippocampus (HPC) and connected cortical circuits (O'Keefe 1976, O'Keefe and Nadel 1978, O'Keefe et al. 1998, Redish 1999, Knierim 2015). Recent work

looking simultaneously at mesoscale cortical activity and HPC electrophysiology has established a temporal link between mesoscale cortical activity and hippocampal oscillatory such as slow gamma activity and sharp wave ripples in the HPC (Abadchi et al. 2020, Liu et al. 2021, Pedrosa et al. 2022a, 2022b)

We posit that the distinct spatio-temporal sequences of cortical activation we observed in this study may be part of a larger cortico-hippocampal network computation wherein incoming sensory information seeds retrieval of encoded memory in the HPC followed by reactivation of trace memory in the cortex, followed by execution of motor sequences in which frontal regions of the cortex are active (**Fig. 3.20**). These sequences are different depending on whether the

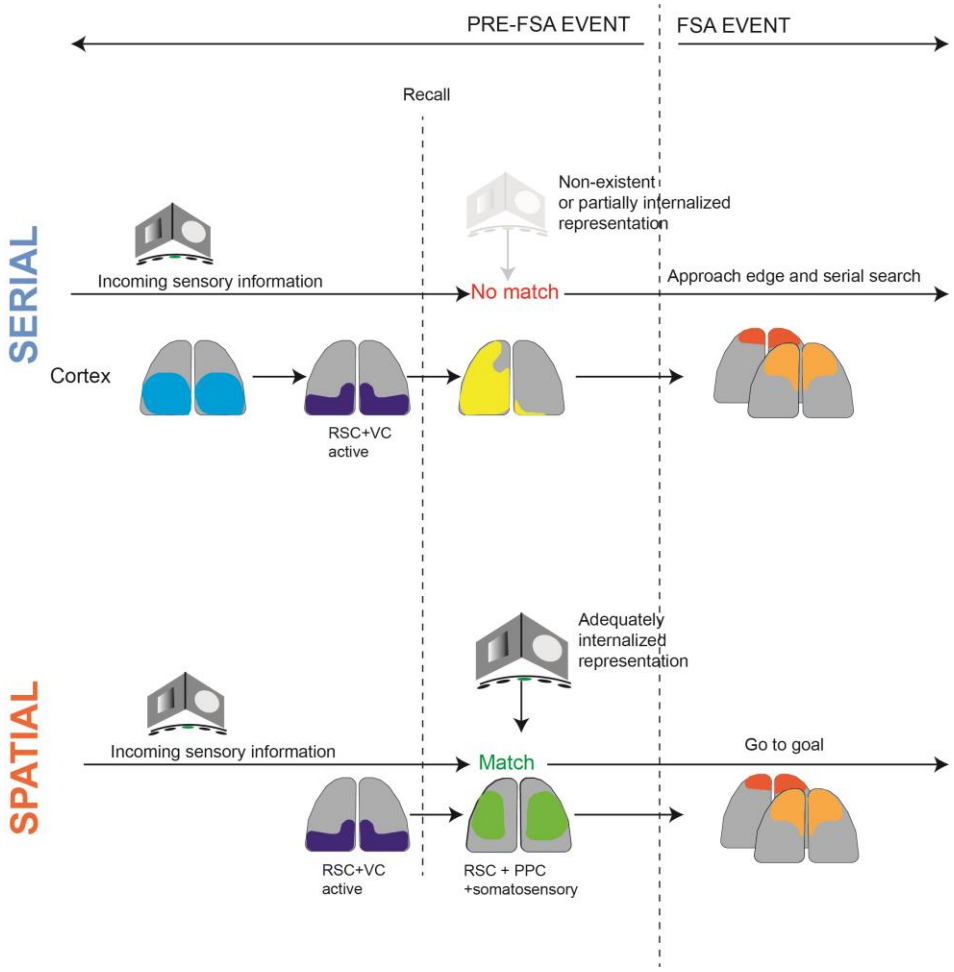

Figure 3.20: Proposed model for distinct cortical dynamics corresponding to non-goal and goal directed search strategies

navigation strategy involves orienting towards a known spatial goal before making an approach or part of a simpler serial search process.

Bibliography

Abadchi JK, Nazari-Ahangarkolaee M, Gattas S, Bermudez-Contreras E, Luczak A, McNaughton BL, Mohajerani MH (2020) Spatiotemporal patterns of neocortical activity around hippocampal sharp-wave ripples. eLife 9. https://doi.org/10.7554/eLife.51972

Aghajan ZM, Acharya L, Moore JJ, Cushman JD, Vuong C, Mehta MR (2015) Impaired spatial selectivity and intact phase precession in two-dimensional virtual reality. Nature Neuroscience 18: 121–128. https://doi.org/10.1038/nn.3884

Alexander AS, Nitz DA (2015) Retrosplenial cortex maps the conjunction of internal and external spaces. Nature Neuroscience 2015 18:8 18: 1143–1151. https://doi.org/10.1038/NN.4058

Alexander AS, Carstensen LC, Hinman JR, Raudies F, William Chapman G, Hasselmo ME (2020) Egocentric boundary vector tuning of the retrosplenial cortex. Science Advances 6. https://doi.org/10.1126/SCIADV.AAZ2322/SUPPL_FILE/AAZ2322_SM.PDF

Allen WE, Kauvar I V., Chen MZ, Richman EB, Yang SJ, Chan K, Gradinaru V, Deverman BE, Luo L, Deisseroth K (2017) Global Representations of Goal-Directed Behavior in Distinct Cell Types of Mouse Neocortex. Neuron 94: 891-907.e6. https://doi.org/10.1016/J.NEURON.2017.04.017

Barbera G, Liang B, Zhang L, Li Y, Lin DT (2019) A wireless miniScope for deep brain imaging in freely moving mice. Journal of Neuroscience Methods 323: 56–60. https://doi.org/10.1016/j.jneumeth.2019.05.008

Barnes CA (1979) Memory deficits associated with senescence: A neurophysiological and behavioral study in the rat. Journal of Comparative and Physiological Psychology. https://doi.org/10.1037/h0077579

Cai DJ, Aharoni D, Shuman T, Shobe J, Biane J, Song W, Wei B, Veshkini M, La-Vu M, Lou J,

Flores SE, Kim I, Sano Y, Zhou M, Baumgaertel K, Lavi A, Kamata M, Tuszynski M, Mayford M, Golshani P, Silva AJ (2016) A shared neural ensemble links distinct contextual memories encoded close in time. Nature 534: 115–118. https://doi.org/10.1038/nature17955

Chen T-W, Wardill TJ, Sun Y, Pulver SR, Renninger SL, Baohan A, Schreiter ER, Kerr RA, Orger MB, Jayaraman V, Looger LL, Svoboda K, Kim DS (2013) Ultrasensitive fluorescent proteins for imaging neuronal activity. Nature 499: 295–300. https://doi.org/10.1038/nature12354

Colavito V, Fabene PF, Grassi-Zucconi G, Pifferi F, Lamberty Y, Bentivoglio M, Bertini G (2013) Experimental sleep deprivation as a tool to test memory deficits in rodents. Frontiers in Systems Neuroscience 7. https://doi.org/10.3389/fnsys.2013.00106

Czajkowski R, Jayaprakash B, Wiltgen B, Rogerson T, Guzman-Karlsson MC, Barth AL, Trachtenberg JT, Silva AJ (2014) Encoding and storage of spatial information in the retrosplenial cortex. Proceedings of the National Academy of Sciences of the United States of America 111: 8661–8666. https://doi.org/10.1073/PNAS.1313222111/SUPPL_FILE/PNAS.201313222SI.PDF

Daigle TL, Madisen L, Hage TA, Valley MT, Knoblich U, Larsen RS, Takeno MM, Huang L, Gu H, Larsen R, Mills M, Bosma-Moody A, Siverts LA, Walker M, Graybuck LT, Yao Z, Fong O, Nguyen TN, Garren E, Lenz GH, Chavarha M, Pendergraft J, Harrington J, Hirokawa KE, Harris JA, Nicovich PR, McGraw MJ, Ollerenshaw DR, Smith KA, Baker CA, Ting JT, Sunkin SM, Lecoq J, Lin MZ, Boyden ES, Murphy GJ, da Costa NM, Waters J, Li L, Tasic B, Zeng H (2018) A Suite of Transgenic Driver and Reporter Mouse Lines with Enhanced Brain-Cell-Type Targeting and Functionality. Cell 174: 465–480. https://doi.org/10.1016/j.cell.2018.06.035

Dana H, Sun Y, Mohar B, Hulse BK, Kerlin AM, Hasseman JP, Tsegaye G, Tsang A, Wong A,

Patel R, Macklin JJ, Chen Y, Konnerth A, Jayaraman V, Looger LL, Schreiter ER, Svoboda K, Kim DS (2019) High-performance calcium sensors for imaging activity in neuronal populations and microcompartments. Nature Methods 16: 649–657. https://doi.org/10.1038/s41592-019-0435-6

Dana H, Chen TW, Hu A, Shields BC, Guo C, Looger LL, Kim DS, Svoboda K (2014) Thy1-GCaMP6 transgenic mice for neuronal population imaging in vivo. PLoS ONE 9. https://doi.org/10.1371/journal.pone.0108697

Dang C, Sodt A, Lau C, Youngstrom B, Ng L, Kuan L, Pathak S, Jones A, Hawrylycz M (2007) The Allen Brain Atlas: Delivering Neuroscience to the Web on a Genome Wide Scale BT - Data Integration in the Life Sciences: 4th International Workshop, DILS 2007, Philadelphia, PA, USA, June 27-29, 2007. Proceedings. In: Cohen-Boulakia S, Tannen V (Eds), Springer Berlin Heidelberg, Berlin, Heidelberg, 17–26. https://doi.org/10.1007/978-3-540-73255-6_4

Dash MB, Douglas CL, Vyazovskiy V V., Cirelli C, Tononi G (2009) Long-term homeostasis of extracellular glutamate in the rat cerebral cortex across sleep and waking states. Journal of Neuroscience 29: 620–629. https://doi.org/10.1523/JNEUROSCI.5486-08.2009

Dawson TM, Golde TE, Lagier-Tourenne C (2018) Animal models of neurodegenerative diseases. Nature Neuroscience 21: 1370–1379. https://doi.org/10.1038/s41593-018-0236-8

Donaldson PDPDD, Ghanbari L, Rynes MLML, Kodandaramaiah SBSB, Swisher SLLSL (2019) Inkjet-Printed Silver Electrode Array for in-vivo Electrocorticography. In: 2019 9th International IEEE/EMBS Conference on Neural Engineering (NER). IEEE Computer Society, 774–777. https://doi.org/10.1109/NER.2019.8717083

Dubbs A, Guevara J, Yuste R (2016) moco: Fast motion correction for calcium imaging. Frontiers in Neuroinformatics. https://doi.org/10.3389/fninf.2016.00006

Erisken S, Vaiceliunaite A, Jurjut O, Fiorini M, Katzner S, Busse L (2014) Effects of Locomotion Extend throughout the Mouse Early Visual System. Current Biology 24: 2899–2907.

https://doi.org/10.1016/J.CUB.2014.10.045

Esteves IM, Chang H, Neumann AR, Sun J, Mohajerani MH, McNaughton BL (2021) Spatial Information Encoding across Multiple Neocortical Regions Depends on an Intact Hippocampus. Journal of Neuroscience 41: 307–319. https://doi.org/10.1523/JNEUROSCI.1788-20.2020

Ferezou I, Haiss F, Gentet LJ, Aronoff R, Weber B, Petersen CCH (2007) Spatiotemporal Dynamics of Cortical Sensorimotor Integration in Behaving Mice. Neuron 56: 907–23. https://doi.org/10.1016/j.neuron.2007.10.007

Fischer LF, Soto-Albors RM, Buck F, Harnett MT (2020) Representation of visual landmarks in retrosplenial cortex. eLife 9. https://doi.org/10.7554/ELIFE.51458

Flossmann T, Rochefort NL (2021) Spatial navigation signals in rodent visual cortex. Current Opinion in Neurobiology 67: 163–173. https://doi.org/10.1016/J.CONB.2020.11.004

Franco LM, Goard MJ (2021) A distributed circuit for associating environmental context with motor choice in retrosplenial cortex. Science advances 7. https://doi.org/10.1126/SCIADV.ABF9815

Geerligs L, van Gerven M, Güçlü U (2021) Detecting neural state transitions underlying event segmentation. NeuroImage 236: 118085. https://doi.org/10.1016/J.NEUROIMAGE.2021.118085

Geerts JP, Chersi F, Stachenfeld KL, Burgess N (2020) A general model of hippocampal and dorsal striatal learning and decision making. Proceedings of the National Academy of Sciences of the United States of America 117: 31427–31437. https://doi.org/10.1073/PNAS.2007981117/SUPPL_FILE/PNAS.2007981117.SAPP.PDF

Ghanbari L, Carter RE, Rynes ML, Dominguez J, Chen G, Naik A, Hu J, Sagar MAK, Haltom L, Mossazghi N, Gray MM, West SL, Eliceiri KW, Ebner TJ, Kodandaramaiah SB (2019a) Cortex-wide neural interfacing via transparent polymer skulls. Nature Communications 10:

1500. https://doi.org/10.1038/s41467-019-09488-0

Ghanbari L, Rynes ML, Hu J, Schulman DS, Johnson GW, Laroque M, Shull GM, Kodandaramaiah SB (2019b) Craniobot: A computer numerical controlled robot for cranial microsurgeries. Scientific Reports 9: 1023. https://doi.org/10.1038/s41598-018-37073-w

Ghosh KK, Burns LD, Cocker ED, Nimmerjahn A, Ziv Y, Gamal A El, Schnitzer MJ (2011) Miniaturized integration of a fluorescence microscope. Nature Methods. https://doi.org/10.1038/nmeth.1694

Gilad A, Helmchen F (2020) Spatiotemporal refinement of signal flow through association cortex during learning. Nature Communications 11: 1744. https://doi.org/10.1038/s41467-020-15534-z

Grewe BF, Langer D, Kasper H, Kampa BM, Helmchen F (2010) High-speed in vivo calcium imaging reveals neuronal network activity with near-millisecond precision. Nature Methods 7: 399–405. https://doi.org/10.1038/nmeth.1453

Harrison FE, Reiserer RS, Tomarken AJ, McDonald MP (2006) Spatial and nonspatial escape strategies in the Barnes maze. Learning and Memory. https://doi.org/10.1101/lm.334306

Harvey CD, Coen P, Tank DW (2012) Choice-specific sequences in parietal cortex during a virtual-navigation decision task. Nature. https://doi.org/10.1038/nature10918

Hull CL (1934a) The concept of the habit-family hierarchy, and maze learning. Part I. Psychological Review 41: 33–54. https://doi.org/10.1037/H0070758

Hull CL (1934b) The concept of the habit-family hierarchy and maze learning: Part II. Psychological Review 41: 134–152. https://doi.org/10.1037/H0072855

Juczewski K, Koussa JA, Kesner AJ, Lee JO, Lovinger DM (2020) Stress and behavioral correlates in the head-fixed method: stress measurements, habituation dynamics, locomotion, and motor-skill learning in mice. Scientific Reports 10: 12245. https://doi.org/10.1038/s41598-020-69132-6

Juneau J, Duret G, Robinson J, Kemere C (2018) Enhanced Image Sensor Module for Head-Mounted Microscopes∗. In: Proceedings of the Annual International Conference of the IEEE Engineering in Medicine and Biology Society, EMBS. Institute of Electrical and Electronics Engineers Inc., 826–829. https://doi.org/10.1109/EMBC.2018.8512387

Juneau J, Duret G, Chu JP, Rodriguez A V, Morozov S, Aharoni D, Robinson JT, St-Pierre F, Kemere C (2020) MiniFAST: A sensitive and fast miniaturized microscope for in vivo neural recording. bioRxiv: 2020.11.03.367466. https://doi.org/10.1101/2020.11.03.367466

Keller GB, Bonhoeffer T, Hübener M (2012) Sensorimotor mismatch signals in primary visual cortex of the behaving mouse. Neuron 74: 809–815. https://doi.org/10.1016/J.NEURON.2012.03.040

Kendler HH, Gasser WP (1948) Variables in spatial learning. I. Number of reinforcements during training. Journal of Comparative and Physiological Psychology 41: 178–187. https://doi.org/10.1037/H0057407

Knierim JJ (2015) The hippocampus. Current Biology 25: R1116–R1121. https://doi.org/10.1016/J.CUB.2015.10.049

Krumin M, Lee JJ, Harris KD, Carandini M (2018a) Decision and navigation in mouse parietal cortex. bioRxiv. https://doi.org/10.1101/166413

Krumin M, Lee JJ, Harris KD, Carandini M (2018b) Decision and navigation in mouse parietal cortex. eLife 7. https://doi.org/10.7554/ELIFE.42583

Lau C, Ng L, Thompson C, Pathak S, Kuan L, Jones A, Hawrylycz M (2008) Exploration and visualization of gene expression with neuroanatomy in the adult mouse brain. BMC Bioinformatics 9: 153. https://doi.org/10.1186/1471-2105-9-153

Lerner TN, Shilyansky C, Davidson TJ, Evans KE, Beier KT, Zalocusky KA, Crow AK, Malenka RC, Luo L, Tomer R, Deisseroth K (2015) Intact-Brain Analyses Reveal Distinct Information Carried by SNc Dopamine Subcircuits. Cell 162: 635–647.

https://doi.org/10.1016/j.cell.2015.07.014

Li P, Geng X, Jiang H, Caccavano A, Vicini S, Wu J (2019) Measuring Sharp Waves and Oscillatory Population Activity With the Genetically Encoded Calcium Indicator GCaMP6f. Frontiers in Cellular Neuroscience 13: 274. https://doi.org/10.3389/fncel.2019.00274

Liu X, Ren C, Lu Y, Liu Y, Kim J-H, Leutgeb S, Komiyama T, Kuzum D (2021) Multimodal neural recordings with Neuro-FITM uncover diverse patterns of cortical–hippocampal interactions. Nature Neuroscience: 1–11. https://doi.org/10.1038/s41593-021-00841-5

Ma Y, Shaik MA, Kozberg MG, Kim SH, Portes JP, Timerman D, Hillman EMC (2016) Resting-state hemodynamics are spatiotemporally coupled to synchronized and symmetric neural activity in excitatory neurons. Proceedings of the National Academy of Sciences of the United States of America 113: E8463–E8471. https://doi.org/10.1073/pnas.1525369113

MacDowell CJ, Buschman TJ (2020) Low-Dimensional Spatiotemporal Dynamics Underlie Cortex-wide Neural Activity. Current Biology 30: 2665-2680.e8. https://doi.org/10.1016/J.CUB.2020.04.090

Madisen L, Garner AR, Shimaoka D, Chuong AS, Klapoetke NC, Li L, van der Bourg A, Niino Y, Egolf L, Monetti C, Gu H, Mills M, Cheng A, Tasic B, Nguyen TN, Sunkin SM, Benucci A, Nagy A, Miyawaki A, Helmchen F, Empson RM, Knöpfel T, Boyden ES, Reid RC, Carandini M, Zeng H (2015) Transgenic mice for intersectional targeting of neural sensors and effectors with high specificity and performance. Neuron 85: 942–958. https://doi.org/10.1016/j.neuron.2015.02.022

Makino H, Ren C, Liu H, Kim AN, Kondapaneni N, Liu X, Kuzum D, Komiyama T (2017) Transformation of Cortex-wide Emergent Properties during Motor Learning. Neuron 94: 880–890. https://doi.org/10.1016/j.neuron.2017.04.015

Mao D, Kandler S, McNaughton BL, Bonin V (2017) Sparse orthogonal population representation of spatial context in the retrosplenial cortex. Nature communications 8.

https://doi.org/10.1038/S41467-017-00180-9

Markus E, Qin Y, Leonard B, Skaggs W, McNaughton B, Barnes C (1995) Interactions between location and task affect the spatial and directional firing of hippocampal neurons. Journal of Neuroscience 15: 7079–7094. https://doi.org/10.1523/JNEUROSCI.15-11-07079.1995

Marvin JS, Borghuis BG, Tian L, Cichon J, Harnett MT, Akerboom J, Gordus A, Renninger SL, Chen TW, Bargmann CI, Orger MB, Schreiter ER, Demb JB, Gan WB, Hires SA, Looger LL (2013) An optimized fluorescent probe for visualizing glutamate neurotransmission. Nature Methods 10: 162–170. https://doi.org/10.1038/nmeth.2333

Mathis A, Mamidanna P, Cury KM, Abe T, Murthy VN, Mathis MW, Bethge M (2018) DeepLabCut: markerless pose estimation of user-defined body parts with deep learning. Nature Neuroscience 21: 1281–1289. https://doi.org/10.1038/s41593-018-0209-y

McDonald RJ, White NM (1994) Parallel information processing in the water maze: Evidence for independent memory systems involving dorsal striatum and hippocampus. Behavioral and Neural Biology 61: 260–270. https://doi.org/10.1016/S0163-1047(05)80009-3

Mcnaughton BL, Barnes CA, Gerrard JL, Gothard K, Jung MW, Knierim JJ, Kudrimoti H, Qin Y, Skaggs WE, Suster M, Weaver KL (1996) Deciphering the hippocampal polyglot: the hippocampus as a path integration system. Journal of Experimental Biology 199: 173–185. https://doi.org/10.1242/JEB.199.1.173

Meyer AF, O'Keefe J, Poort J (2020) Two Distinct Types of Eye-Head Coupling in Freely Moving Mice. Current Biology 30: 2116-2130.e6. https://doi.org/10.1016/j.cub.2020.04.042

Mika Diamanti E, Reddy CB, Schröder S, Muzzu T, Harris KD, Saleem AB, Carandini M (2021) Spatial modulation of visual responses arises in cortex with active navigation. eLife 10: 1–15. https://doi.org/10.7554/ELIFE.63705

Miller AMP, Mau W, Smith DM (2019) Retrosplenial Cortical Representations of Space and Future Goal Locations Develop with Learning. Current Biology 29: 2083-2090.e4.

https://doi.org/10.1016/j.cub.2019.05.034

Mohajerani MH, Chan AW, Mohsenvand M, Ledue J, Liu R, McVea DA, Boyd JD, Wang YT, Reimers M, Murphy TH (2013) Spontaneous cortical activity alternates between motifs defined by regional axonal projections. Nature Neuroscience 16: 1426–1435. https://doi.org/10.1038/nn.3499

Mohajerani MH, McVea DA, Fingas M, Murphy TH (2010) Mirrored bilateral slow-wave cortical activity within local circuits revealed by fast bihemispheric voltage-sensitive dye imaging in anesthetized and awake mice. Journal of Neuroscience 30: 3745–3751. https://doi.org/10.1523/JNEUROSCI.6437-09.2010

Morris RGM (1981) Spatial localization does not require the presence of local cues. Learning and Motivation 12: 239–260. https://doi.org/10.1016/0023-9690(81)90020-5

Morris RGM, Garrud P, Rawlins JNP, O'Keefe J (1982) Place navigation impaired in rats with hippocampal lesions. Nature 1982 297:5868 297: 681–683. https://doi.org/10.1038/297681a0

Murphy TH, Boyd JD, Bolaños F, Vanni MP, Silasi G, Haupt D, Ledue JM (2016) High-throughput automated home-cage mesoscopic functional imaging of mouse cortex. Nature Communications 7: 11611. https://doi.org/10.1038/ncomms11611

Musall S, Kaufman MT, Juavinett AL, Gluf S, Churchland AK (2019a) Single-trial neural dynamics are dominated by richly varied movements. Nature Neuroscience. https://doi.org/10.1038/s41593-019-0502-4

Musall S, Kaufman MT, Juavinett AL, Gluf S, Churchland AK (2019b) Single-trial neural dynamics are dominated by richly varied movements. Nature Neuroscience 22: 1677–1686. https://doi.org/10.1038/s41593-019-0502-4

Namiki S, Sakamoto H, Iinuma S, Iino M, Hirose K (2007) Optical glutamate sensor for spatiotemporal analysis of synaptic transmission. European Journal of Neuroscience 25:

2249–59. https://doi.org/10.1111/j.1460-9568.2007.05511.x

Negrón-Oyarzo I, Espinosa N, Aguilar M, Fuenzalida M, Aboitiz F, Fuentealba P (2018) Coordinated prefrontal–hippocampal activity and navigation strategy-related prefrontal firing during spatial memory formation. Proceedings of the National Academy of Sciences of the United States of America 115: 7123–7128. https://doi.org/10.1073/PNAS.1720117115/SUPPL_FILE/PNAS.1720117115.SM03.WMV

Niell CM, Stryker MP (2010) Modulation of Visual Responses by Behavioral State in Mouse Visual Cortex. Neuron 65: 472–479. https://doi.org/10.1016/J.NEURON.2010.01.033

Nitz DA (2006a) Tracking route progression in the posterior parietal cortex. Neuron. https://doi.org/10.1016/j.neuron.2006.01.037

Nitz DA (2006b) Tracking route progression in the posterior parietal cortex. Neuron 49: 747–756. https://doi.org/10.1016/j.neuron.2006.01.037

Niu Y, Shen B, Cui Y, Chen Y, Wang J, Wang L, Kang Y, Zhao X, Si W, Li W, Xiang AP, Zhou J, Guo X, Bi Y, Si C, Hu B, Dong G, Wang H, Zhou Z, Li T, Tan T, Pu X, Wang F, Ji S, Zhou Q, Huang X, Ji W, Sha J (2014) Generation of gene-modified cynomolgus monkey via Cas9/RNA-mediated gene targeting in one-cell embryos. Cell 156: 836–843. https://doi.org/10.1016/j.cell.2014.01.027

O'Keefe J (1976) Place units in the hippocampus of the freely moving rat. Experimental Neurology 51: 78–109. https://doi.org/10.1016/0014-4886(76)90055-8

O'Keefe J, Dostrovsky J (1971) The hippocampus as a spatial map. Preliminary evidence from unit activity in the freely-moving rat. Brain Research 34: 171–175. https://doi.org/10.1016/0006-8993(71)90358-1

O'Keefe J, Nadel L (1978) The Hippocampus as a Cognitive Map. Oxford University Press: Oxford, UK. (1978) .

O'Keefe J, Burgess N, Donnett JG, Jeffery KJ, Maguire EA (1998) Place cells, navigational

accuracy, and the human hippocampus. Philosophical Transactions of the Royal Society B: Biological Sciences 353: 1333. https://doi.org/10.1098/RSTB.1998.0287

Pakan JMP, Currie SP, Fischer L, Rochefort NL (2018) The Impact of Visual Cues, Reward, and Motor Feedback on the Representation of Behaviorally Relevant Spatial Locations in Primary Visual Cortex. Cell Reports 24: 2521–2528. https://doi.org/10.1016/J.CELREP.2018.08.010

Patti CL, Zanin KA, Sanday L, Kameda SR, Fernandes-Santos L, Fernandes HA, Andersen ML, Tufik S, Frussa-Filho R (2010) Effects of sleep deprivation on memory in mice: Role of state-dependent learning. Sleep 33: 1669–1679. https://doi.org/10.1093/sleep/33.12.1669

Pedrosa R, Nazari M, Mohajerani MH, Knöpfel T, Stella F, Battaglia FP (2022a) Hippocampal gamma and sharp wave/ripples mediate bidirectional interactions with cortical networks during sleep. Proceedings of the National Academy of Sciences of the United States of America 119: e2204959119. https://doi.org/10.1073/PNAS.2204959119/SUPPL_FILE/PNAS.2204959119.SM03.AVI

Pedrosa R, Nazari M, Kergoat L, Bernard C, Mohajerani M, Stella F, Battaglia F (2022b) Hippocampal ripples coincide with “up-state” and cortical spindles in Retrosplenial Cortex. bioRxiv: 2022.12.19.521088. https://doi.org/10.1101/2022.12.19.521088

Pinheiro-da-Silva J, Fernandes Silva P, Nogueira M, Luchiari A (2016) ESM 1.

Pinto L, Rajan K, DePasquale B, Thiberge SY, Tank DW, Brody CD (2019a) Task-Dependent Changes in the Large-Scale Dynamics and Necessity of Cortical Regions. Neuron 104: 810–824. https://doi.org/10.1016/j.neuron.2019.08.025

Pinto L, Rajan K, Depasquale B, Thiberge SY, Tank DW, Brody CD (2019b) Task-Dependent Changes in the Large-Scale Dynamics and Necessity of Cortical Regions In Brief Article Task-Dependent Changes in the Large-Scale Dynamics and Necessity of Cortical Regions. Neuron 104: 810–824. https://doi.org/10.1016/j.neuron.2019.08.025

Pitts M (2018) Barnes Maze Procedure for Spatial Learning and Memory in Mice. BIO-PROTOCOL. https://doi.org/10.21769/bioprotoc.2744

Ramos A (2008) Animal models of anxiety: do I need multiple tests? Trends in Pharmacological Sciences 29: 493–498. https://doi.org/10.1016/j.tips.2008.07.005

Redish AD (1999) Beyond the Cognitive Map: From Place Cells to Episodic Memory. Beyond the Cognitive Map. https://doi.org/10.7551/MITPRESS/1571.001.0001

Rothschild G, Eban E, Frank LM (2017) A cortical–hippocampal–cortical loop of information processing during memory consolidation. Nature neuroscience 20: 251. https://doi.org/10.1038/NN.4457

Rynes ML, Surinach DA, Linn S, Laroque M, Rajendran V, Dominguez J, Hadjistamoulou O, Navabi ZS, Ghanbari L, Johnson GW, Nazari M, Mohajerani MH, Kodandaramaiah SB (2021) Miniaturized head-mounted microscope for whole-cortex mesoscale imaging in freely behaving mice. Nature Methods 2021 18:4 18: 417–425. https://doi.org/10.1038/s41592-021-01104-8

Rynes ML, Ghanbari L, Schulman DS, Linn S, Laroque M, Dominguez J, Navabi ZS, Sherman P, Kodandaramaiah SB (2020) Assembly and operation of an open-source, computer numerical controlled (CNC) robot for performing cranial microsurgical procedures. Nature Protocols 15: 1992–2023. https://doi.org/10.1038/s41596-020-0318-4

Saleem AB, Ayaz AI, Jeffery KJ, Harris KD, Carandini M (2013) Integration of visual motion and locomotion in mouse visual cortex. Nature Neuroscience 2013 16:12 16: 1864–1869. https://doi.org/10.1038/nn.3567

Saleem AB, Diamanti EM, Fournier J, Harris KD, Carandini M (2018) Coherent encoding of subjective spatial position in visual cortex and hippocampus. Nature 562: 124. https://doi.org/10.1038/S41586-018-0516-1

Schindelin J, Arganda-Carreras I, Frise E, Kaynig V, Longair M, Pietzsch T, Preibisch S,

Rueden C, Saalfeld S, Schmid B, Tinevez JY, White DJ, Hartenstein V, Eliceiri K, Tomancak P, Cardona A (2012) Fiji: An open-source platform for biological-image analysis. Nature Methods 9: 676–682. https://doi.org/10.1038/nmeth.2019

Scott BB, Thiberge SY, Guo C, Tervo DGR, Brody CD, Karpova AY, Tank DW (2018) Imaging Cortical Dynamics in GCaMP Transgenic Rats with a Head-Mounted Widefield Macroscope. Neuron 100: 1045–1058. https://doi.org/10.1016/j.neuron.2018.09.050

Silasi G, Xiao D, Vanni MP, Chen ACN, Murphy TH (2016) Intact skull chronic windows for mesoscopic wide-field imaging in awake mice. Journal of Neuroscience Methods 267: 141–149. https://doi.org/10.1016/j.jneumeth.2016.04.012

Singh S, Bermudez-Contreras E, Nazari M, Sutherland RJ, Mohajerani MH (2019) Low-cost solution for rodent home-cage behaviour monitoring. Silvani A (Ed.). PLoS ONE 14: e0220751. https://doi.org/10.1371/journal.pone.0220751

Skocek O, Nöbauer T, Weilguny L, Martínez Traub F, Xia CN, Molodtsov MI, Grama A, Yamagata M, Aharoni D, Cox DD, Golshani P, Vaziri A (2018) High-speed volumetric imaging of neuronal activity in freely moving rodents. Nature Methods 15: 429–432. https://doi.org/10.1038/s41592-018-0008-0

Teixeira CM, Pomedli SR, Maei HR, Kee N, Frankland PW (2006) Involvement of the Anterior Cingulate Cortex in the Expression of Remote Spatial Memory. The Journal of Neuroscience 26: 7555. https://doi.org/10.1523/JNEUROSCI.1068-06.2006

Tolman EC (1948) Cognitive maps in rats and men. Psychological Review 55: 189–208. https://doi.org/10.1037/H0061626

Tolman EC, Ritchie BF, Kalish D (1946) Studies in spatial learning. I. Orientation and the short-cut. Journal of Experimental Psychology 36: 13–24. https://doi.org/10.1037/H0053944

Valley MT, Moore MG, Zhuang J, Mesa N, Castelli D, Sullivan D, Reimers M, Waters J (2020) Separation of hemodynamic signals from GCaMP fluorescence measured with wide-field

imaging. Journal of Neurophysiology 123: 356–366. https://doi.org/10.1152/jn.00304.2019

Vanni MP, Murphy TH (2014) Mesoscale transcranial spontaneous activity mapping in GCaMP3 transgenic mice reveals extensive reciprocal connections between areas of somatomotor cortex. Journal of Neuroscience 34: 15931–15946. https://doi.org/10.1523/JNEUROSCI.1818-14.2014

Vedder LC, Miller AMP, Harrison MB, Smith DM (2017) Retrosplenial Cortical Neurons Encode Navigational Cues, Trajectories and Reward Locations During Goal Directed Navigation. Cerebral Cortex 27: 3713–3723. https://doi.org/10.1093/CERCOR/BHW192

Watson JB (1907) Kinæsthetic and organic sensations: Their role in the reactions of the white rat to the maze. The Psychological Review: Monograph Supplements 8: i–101. https://doi.org/10.1037/H0093040

Wekselblatt JB, Flister ED, Piscopo DM, Niell CM (2016) Large-scale imaging of cortical dynamics during sensory perception and behavior. Journal of Neurophysiology 115: 2852–66. https://doi.org/10.1152/jn.01056.2015

West SL, Aronson JD, Popa LS, Feller KD, Carter RE, Chiesl WM, Gerhart ML, Shekhar AC, Ghanbari L, Kodandaramaiah SB, Ebner TJ (2022) Wide-Field Calcium Imaging of Dynamic Cortical Networks during Locomotion. Cerebral Cortex 32: 2668–2687. https://doi.org/10.1093/CERCOR/BHAB373

Whitlock JR (2014) Navigating actions through the rodent parietal cortex. Frontiers in Human Neuroscience. https://doi.org/10.3389/fnhum.2014.00293

Wilber AA, Clark BJ, Forster TC, Tatsuno M, McNaughton BL (2014) Interaction of Egocentric and World-Centered Reference Frames in the Rat Posterior Parietal Cortex. Journal of Neuroscience. https://doi.org/10.1523/JNEUROSCI.0511-14.2014

Wyass JM, Van Groen T (1992) Connections between the retrosplenial cortex and the hippocampal formation in the rat: a review. Hippocampus 2: 1–11.

https://doi.org/10.1002/HIPO.450020102

Zong W, Wu R, Li M, Hu Y, Li Y, Li J, Rong H, Wu H, Xu Y, Lu Y, Jia H, Fan M, Zhou Z, Zhang Y, Wang A, Chen L, Cheng H (2017) Fast high-resolution miniature two-photon microscopy for brain imaging in freely behaving mice. Nature Methods 14: 713.

Appendix

Appendix A: T-distance optimization of cortical activation state counts for all mice

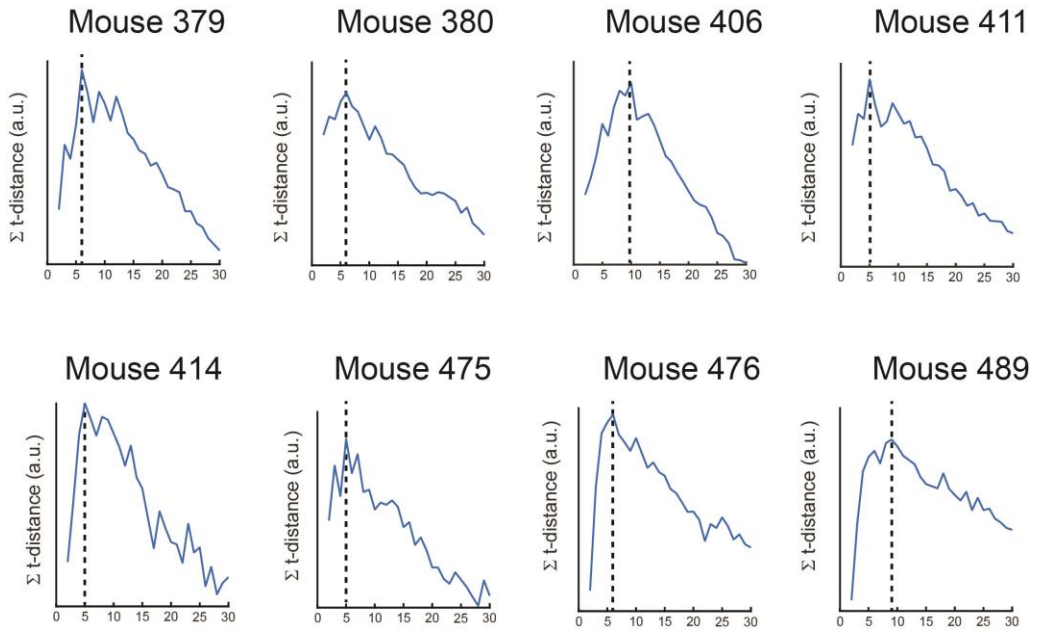

Figure A1: t-distance optimization of cortical activation state counts for all mice. T-distance plots for the optimum number of states found for each mouse using the algorithm described in **Figure 3.1.** There are 5-10 optimum states found across n=8 mice.

Appendix B: State activation along mice paths

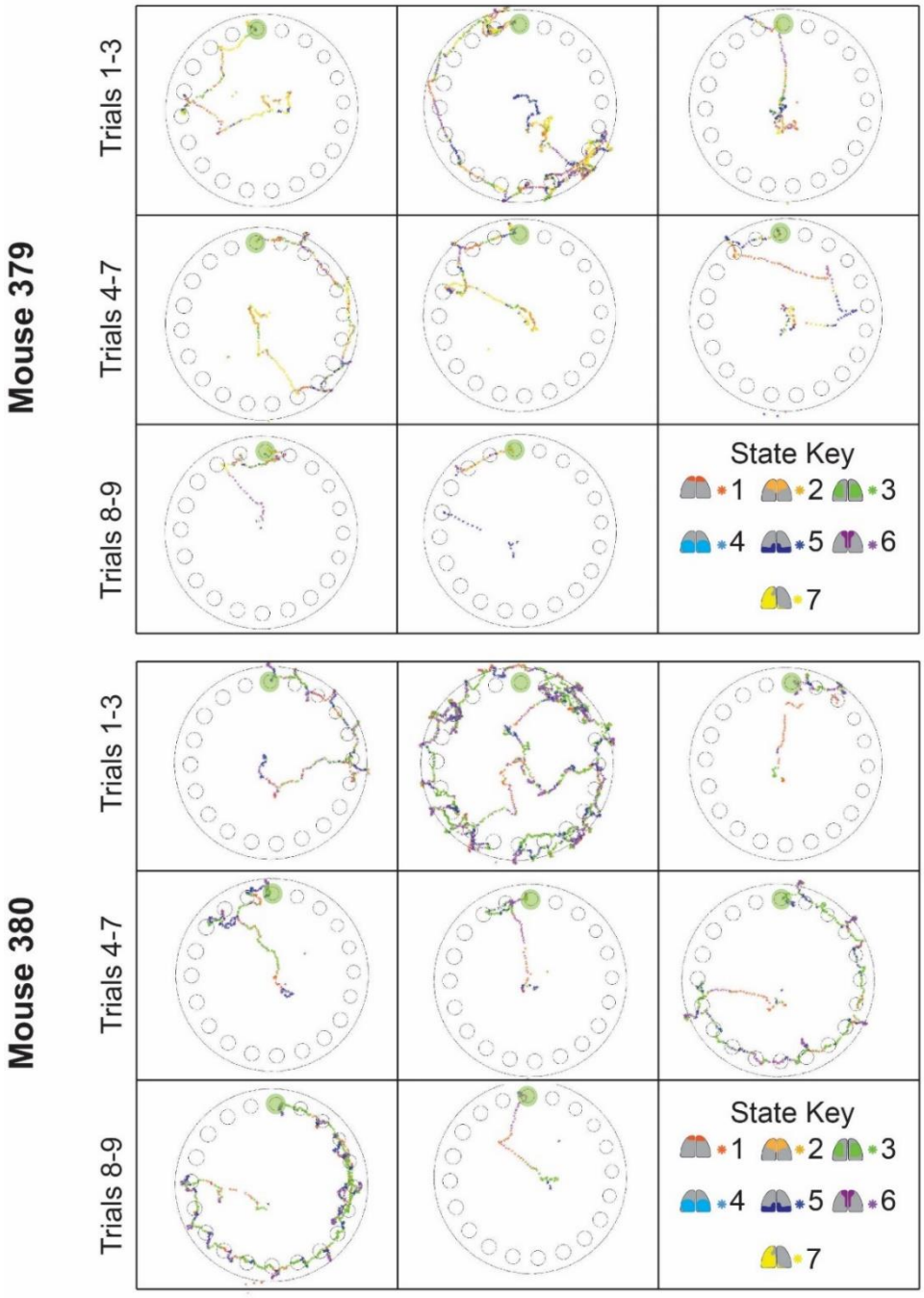

Figure A2: State activation along mice paths. State activation plotted along paths taken by mice for all acquisition trials are shown for mice 379 and 380**.**

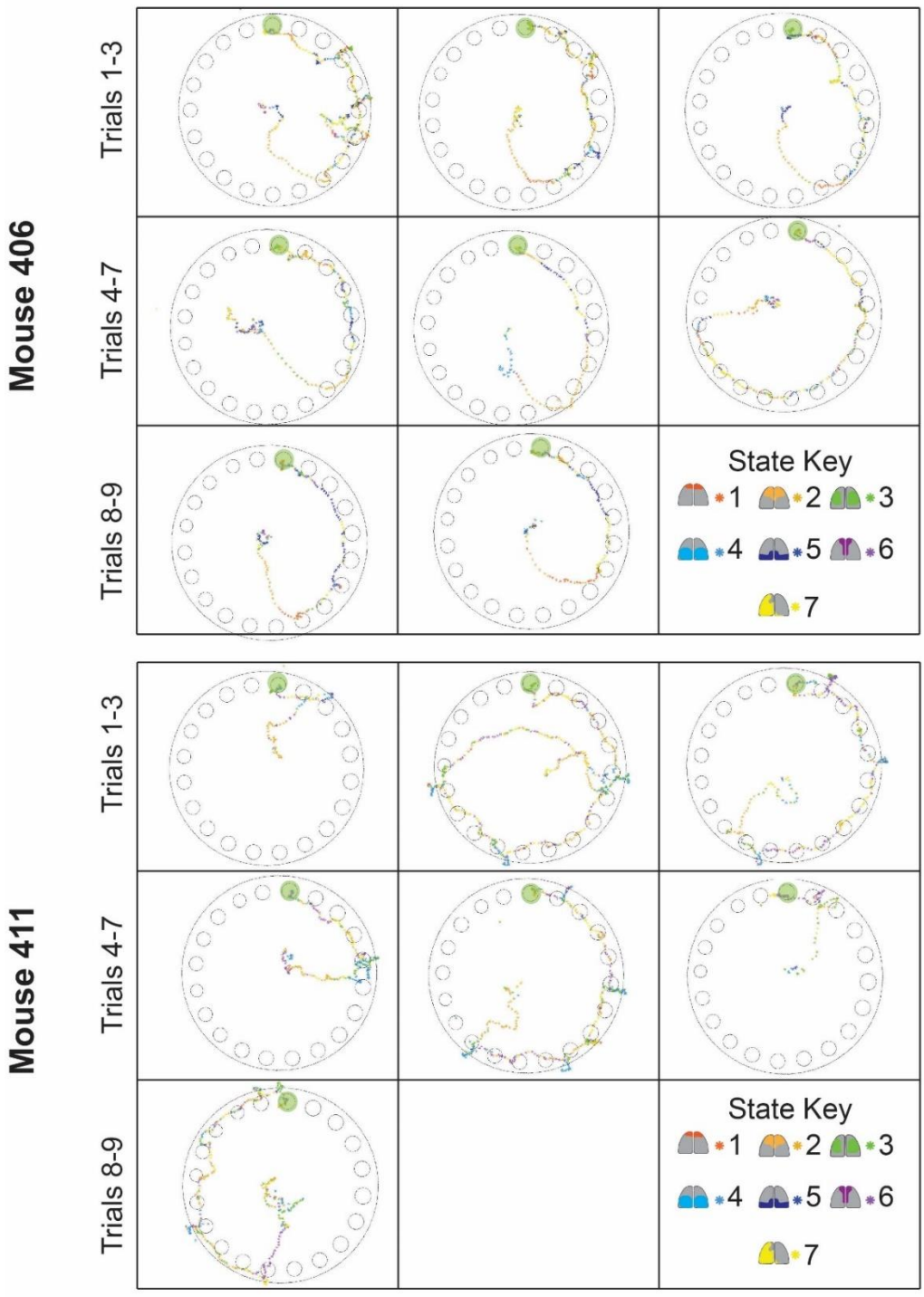
Mouse 406
Trials 1-3
Trials 4-7
Trials 8-9
State Key
1
2
3
4
5
6
7
Mouse 411
Trials 1-3
Trials 4-7
Trials 8-9
State Key
1
2
3
4
5
6
7

Figure A3: State activation along mice paths. State activation plotted along paths taken by mice for all acquisition trials are shown for mice 406 and 411.

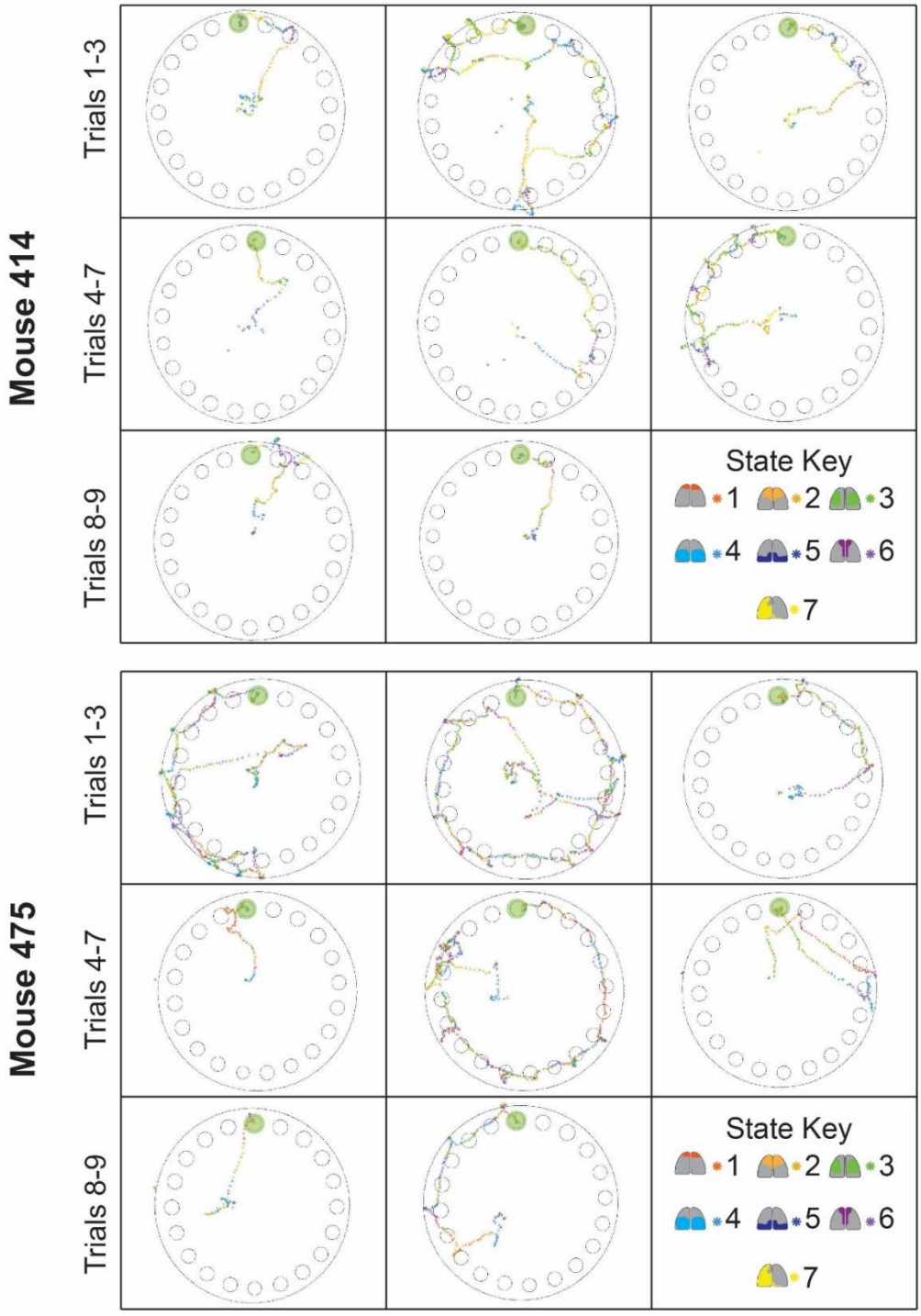

Figure A4: State activation along mice paths. State activation plotted along paths taken by mice for all acquisition trials are shown for mice 414 and 475.

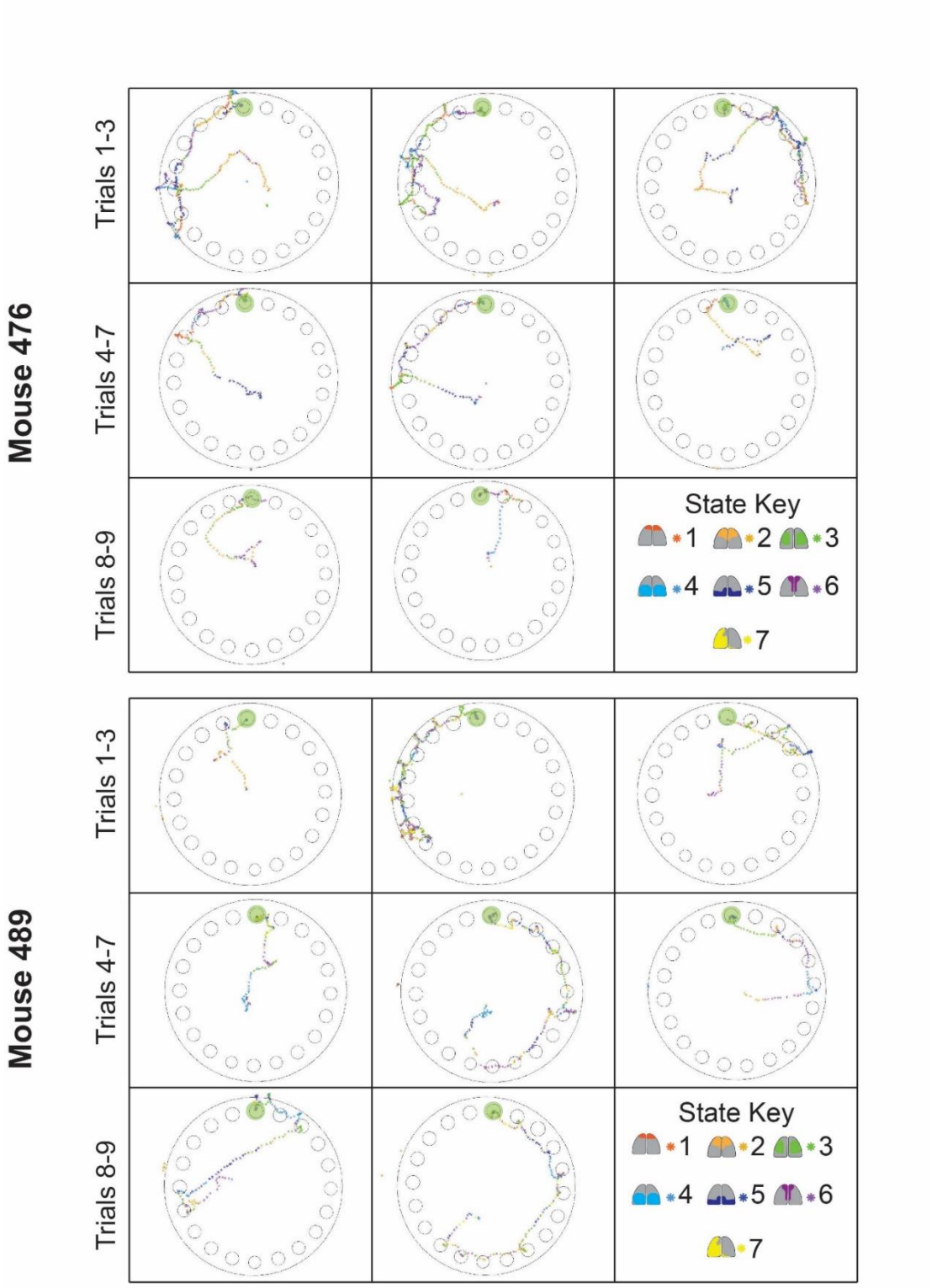

Figure A5: State activation along mice paths. State activation plotted along paths taken by mice for all acquisition trials are shown for mice 476 and 489.